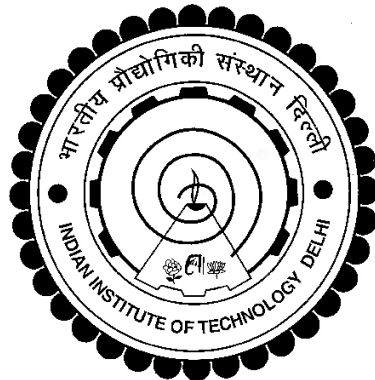


MODELLING OF PIEZO-STRUCTURE ELASTODYNAMIC INTERACTION THROUGH BOND LAYER FOR ELECTRO- MECHANICAL IMPEDANCE TECHNIQUE

SUMEDHA MOHARANA



**DEPARTMENT OF CIVIL ENGINEERING
INDIAN INSTITUTE OF TECHNOLOGY DELHI**

NOVEMBER 2012

MODELLING OF PIEZO-STRUCTURE ELASTODYNAMIC INTERACTION THROUGH BOND LAYER FOR ELECTRO- MECHANICAL IMPEDANCE TECHNIQUE

by

SUMEDHA MOHARANA

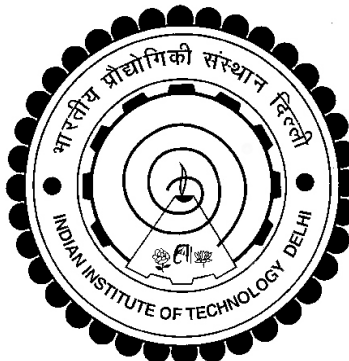
Department of Civil Engineering

Submitted

in fulfillment of the requirements of the degree of

Doctor of Philosophy

to the



Indian Institute of Technology Delhi

November 2012

CERTIFICATE

This is to certify that the thesis entitled, "**MODELLING OF PIEZO-STRUCTURE ELASTODYNAMIC INTERACTION THROUGH BOND LAYER FOR ELECTROMECHANICAL IMPEDANCE TECHNIQUE**" submitted by **Ms. Sumedha Moharana** to Indian Institute of Technology Delhi, for the award of the degree of the **Doctor of Philosophy** is a record of bonafide research work carried out by her. She worked under my supervision for the submission of this thesis, which to the best of my knowledge, has reached the requisite standard.

The research reports and the results presented in this thesis have not been submitted in parts or in full to any other University or Institute for the award of any degree or diploma.

Dr. Suresh Bhalla

Associate Professor

Department of Civil Engineering

Indian Institute of Technology, Delhi

New Delhi – 110016

INDIA

ACKNOWLEDGEMENTS

First and foremost, I would like to extend my sincere thanks and gratitude towards my supervisor, Dr Suresh Bhalla, for his continuous guidance, encouragement and strong support during the course of my Ph.D. research. It has been an honour to be associated with Dr. Suresh Bhalla whose suggestions and critical views have greatly helped me in this work. I am eternally grateful for his kindness, helpful guidance, and discussions. He truly exemplifies the role of advisors. I am forever grateful for his kindness and contributions, not only towards my research, but towards my professional growth as well.

I am grateful to my committee members of Prof K. G. Sharma, Dr. Swadesh De and Dr Vasant Matsagar, who provided their useful suggestions and advice regarding my research work. I thank my friends Sanjay and Usha, without them, things would have been very difficult. I am also thankful to my colleague, Vishalakshi, Naveet and Dinesh, for providing imminent helps to conduct the lab experiments.

My thanks are also due to all the Civil Engineering faculty and other staff members for their support and keenness in my work. I am extremely grateful to the staff of Smart Structures and Dynamics Laboratory (SSDL), departmental and central library for providing books, journals etc., which made this research work possible.

I express my special thanks to Mr Lal Singh, Mr Vinod, Mr Mansukh and other technicians, who provided their technical support generously during the lab work. Special thanks go to almighty God and my parent and sisters for their encouragement and love. Their support and kind encouragements provided the essential foundation to thrive and success.

Sumedha Moharana

ABSTRACT

As impedance transducers, the piezoelectric ceramic (PZT) patches have emerged as strong candidates for structural health monitoring (SHM) of structures in the recent years because of their small size and shape, cost-effectiveness and ease of installation. The research for structural identification and long-term monitoring has recently become an area of interest for a large number of academic and commercial laboratories. The associated techniques aim to enable structures and equipment monitor their own structural integrity while in operation, and shall be useful not only to improve reliability, but also to reduce maintenance and inspection costs.

This thesis is focused on the electro-mechanical impedance (EMI) technique for SHM. The basic principle behind this technique is to use high frequencies (typically >50 kHz) generated by surface-bonded PZT patch to detect changes in structural drive point impedance caused by internal/ surface cracks, loose connections, delaminations or any other type of damage. The resultant electro-mechanical interaction, which is characteristic of the particular structure, modulates the current flowing through the PZT patch. The modulation is a function of the mechanical interaction between the PZT patch and the structure over the considered frequency range. The resultant admittance signature, which acts like a frequency response function (FRF), is used to detect changes or damages occurring in the host structure.

The bond layer between the PZT patch and host structure plays a significant role in PZT-structure interaction in the EMI technique. To understand the mechanism of force transfer through the adhesive medium (which introduce shear lag effect) more precisely, various models have been proposed by researchers in the past. Some of those are based on static, dynamic, effective and simplified interaction through the bond layer. However, these models still lack

rigour in terms of considering all governing parameters, especially both shear and inertia terms simultaneously. Understanding shear mechanism phenomena of the adhesive layer is vital for enhanced applicability of the EMI technique.

The main objective of this research work is to model the shear lag phenomena (between PZT patch and host structure) analytically, achieving more accurate model. The previous analytical models have ignored the inertia term, which has been rigorously integrated in this research to arrive at a new refined shear lag model. The new model considers both shear lag and inertia effects simultaneously. The predictions of the new model are much better match with experimental observations as compared to the previous models. Various parametric studies have also been carried out to study the influence of the piezo and the structural properties on the admittance signatures.

The research is further extended by considering the inertia effect of the adhesive mass (so far neglected) in addition to that of the PZT patch. A continuum based admittance approach has been formulated where the “equivalent and effective impedance” terms are replaced by continuum displacement term developed at interfacial adhesive bond. This model considers the bond layer’s connection between the patch and structure throughout the sensor length, unlike the previous models which were restricted to boundary interactions. Parametric studies have followed to support the sustainability and suitability of proposed continuum approach. Finally, to enhance the efficiency of the proposed model in real life application on SHM and active control system, the study of electrical power consumption and energy efficiency has been carried out. Various energy conversion efficiency ratios have been obtained by evaluating the total energy used for mechanical response to the total energy supplied. In overall, the study shows significant influence of the bond layer on energy efficiency. A modified electro-mechanical

coupling coefficient has been derived from basic strain energy relationship taking care of the mechanical, dielectric and shear lag losses of piezo active control system.

In overall, it is hoped that the outcome of this research will be of significant help SHM based on EMI technique.

CONTENTS

CERTIFICATE.....	i
ACKNOWLEDGEMENTS	ii
ABSTRACT.....	iii
CONTENTS	vi
LIST OF FIGURES	ix
LIST OF TABLES	xvi
LIST OF SYMBOLS.....	xvii
LIST OF ABBREVIATIONS	xxiii
CHAPTER-1: INTRODUCTION	1
1.1 Research Background	1
1.2 Motivation.....	1
1.3 Smart Materials And Structures.....	3
1.4 Basics of EMI Technique	4
1.5 Shear Lag Effect.....	6
1.6 Power and Energy Consumption For Bonding Effect.....	7
1.7 Various SHM techniques: A comparison	9
1.8 Thesis Organization.....	10
CHAPTER-2:IMPEDANCE BASED MODELING OF PIEZO-STRUCTURE INTERACTION.....	12
2.1 Introduction	12
2.2 EMI Based Structural Health Monitoring	14
2.3 Piezo-Structure Interaction Modeling For EMI Technique.....	17
2.3.1 Static Approach	17
2.3.2 Impedance Approach	19
2.4 Inclusion of Shear Lag Effect In Impedance Based Models	28
2.5 Numerical Investigation of Shear Lag Effect of FE Piezo-Structure Interaction Model	35
2.6 Summary: Critical Points of Review.....	39
2.7 Gaps identified in previous research	40
2.7 Research Objectives	41

CHAPTER-3:COUPLED FIELD FINITE ELEMENT MODELING AND SIMULATION OF SHEAR LAG EFFECT FOR EMI TECHNIQUE	42
3.1 Introduction	42
3.2 FE Modelling of PZT Transducers.....	43
3.3 Review of FE Modelling Using Coupled-Field Analysis	44
3.4 Theory of Coupled Piezoelectric Analysis	45
3.5 2D FE Modelling of Adhesively Bonded PZT Patch.....	52
3.6 3D FE Modelling of Adhesively Bonded PZT Patch	57
3.7.1 Parametric Study For Piezo-Structure Interaction	63
(a) Effect of Bond Length	63
(b) Effect of Shear Modulus	64
(c) Effect of Bond Layer Damping	65
3.8 Concluding Remarks	65
CHAPTER-4 : DEVLOPMENT OF SHEAR LAG MODEL	67
4.1 Introduction	67
4.2 Derivation of Proposed 1D Shear Lag Model.....	67
4.3 Extension of Refined Shear Lag Formulation to 2D	72
4.4 Comparison with Previous Models and Experiment	75
4.5 Effect of Inclusion of Adhesive Mass	83
4.6 Interfacial Stress and Strain Analysis for Coupled Phenomena	85
4.6.1 Shear Stress Profile Along Bond Layer	87
4.6.2 Effective Strain Profile Along Bond Layer	91
4.6.3 Variation Effective Axial Stress Along Adhesive Bond	93
4.7 Parametric Study of Adhesive Bond Layer Induced Admittance Signature	94
4.7.1 Effect of Bond Layer's Shear Modulus	94
4.7.2 Effect of Bond Layer Thickness	94
4.7.3 Influence of Damping bond layer	96
4.7.4 Effect of Sensor Length	96
4.7.5 Effect of Excitation Voltage.....	97
4.8 Concluding Remarks	98
CHAPTER-5 : EXTENSION TO CONTINUUM BASED SHEAR LAG MODEL.....	99
5.1 Introduction	99

5.2 Derivation of Admittance Signature using Continuum Approach	100
5.3 Experimental Verification	103
5.4 Parametric Study for Continuum Signature.....	108
5.5 Effect on Adhesive Mass on Continuum Based Admittance Signature.....	112
5.6 Conclusions	114
CHAPTER-6 : Bond Effect on Power And Energy Transduction Efficiency.....	115
6.1 Introduction.....	115
6.2 Electrical Impedance And Power Triangle.....	115
6.3 Power and Energy Flow in Piezo-Mechanical Interaction	118
6.4 Electrical Power Consumption in Piezo-Impedance Transducer.....	121
6.5 Energy Conversion Efficiency of Piezo-Active Mechanical System.....	128
6.6 Energy Conversion Efficiency Ratio For Bonding Influence On Piezo-Impedance System	130
6.7 Formulations for Modified Electro-Mechanical Coupling Coefficient.....	134
6.8 Concluding Remarks	137
CHAPTER-7: CONCLUSIONS AND RECOMENDATIONS	138
7.1 Introduction.....	138
7.2 Research originality and contributions	139
7.3 Research conclusions	140
7.4 Recommendations	142
REFERENCES	145
APPENDICES	157
AUTHOR'S PUBLICATION	167
BIODATA	169

LIST OF FIGURES

FIGURE NO	TITLE	PAGE NO
2.1	A deformed PZT patch	14
2.2	Representation of harmonic force and velocity by rotating phasor	15
2.3	Determination of mechanical impedance of PZT patch	16
2.4	Modelling of PZT-structure interaction by static approach	18
2.5	Liang's 1D impedance model	20
2.6	2D impedance model of Zhou et al. (1996)	22
2.7	Effective impedance model (Bhalla and Soh, 2004a)	25
2.8	A schematic representation of actuating forces from PZT patches acting on the host structure. (Cheng and Lim, 2005)	27
2.9	Modified impedance model of Xu and Liu (2002) including bond layer	31
2.10	Force/strain transfer mechanism through adhesive bond	32
2.11	Simplified 1D impedance model (Bhalla et al., 2009)	34
3.1	A piezoelectric material sheet with <ul style="list-style-type: none"> (a) Axes as per IEEE standard (b) Axes as per ANSYS format 	46
3.2	FE model of 2D PZT- Structure interaction	52
3.3	Effect of adhesive on PZT-Structure interaction signature <ul style="list-style-type: none"> (a) Conductance(G) vs Frequency (b) Susceptance(B) vs Frequency 	53
3.4	Comparison of coupled field numerical result with other analytical results <ul style="list-style-type: none"> (a) Conductance(G) vs Frequency (b) Susceptance(B) vs Frequency 	54
3.5	Effect of bond thickness on electro-mechanical admittance signature <ul style="list-style-type: none"> (a) Conductance(G) vs Frequency 	55

.	(b) Susceptance(B) vs Frequency	55
3.6	Effect of shear modulus of bond layer on electro-mechanical admittance signature	55
	(a) Conductance(G) vs Frequency	55
	(b) Susceptance(B) vs Frequency	55
3.7	Effect of Mechanical loss of PZT patch on electro- mechanical admittance signature	56
	(a) Conductance(G) vs Frequency	56
	(b) Susceptance(B) vs Frequency	56
3.8	Effect of sensor length on electro- mechanical admittance signature	56
	(a) Conductance(G) vs Frequency	56
	(b) Susceptance(B) vs Frequency	56
3.9	Isometric view of one-fourth of aluminium block (48mm x 48mm x10mm) adhesively bonded with PZT-patch modelled in ANSYS12.0 workspace.	58
3.10	Comparison of numerical obtained signatures of perfectly bonded PZT-structure system and adhesively bonded PZT- structure interaction system	61
	(a) Conductance(G) vs Frequency	61
	(b) Susceptance(B) vs Frequency	61
3.11	Comparison of 3D numerical EMI signature with analytical and numerical admittance signatures (Bhalla and Soh, 2004c)	62
	(a) Conductance(G) vs Frequency	62
	(b) Susceptance(B) vs Frequency	62
3.12	Effect of bond layer thickness on electro-mechanical admittance signature for 3D coupled analysis field	63
	(a) Conductance(G) vs Frequency	63
	(b) Susceptance(B) vs Frequency	63
3.13	Effect of shear modulus of adhesive on electro-mechanical admittance signature obtained through 3D coupled field	64

	analysis	
	(a) Conductance(G) vs Frequency	64
	(b) Susceptance(B) vs Frequency	64
3.14	Effect of bond layer damping on coupled FE admittance signature	65
	(a) Conductance(G) vs Frequency	65
	(b) Susceptance(B) vs Frequency	65
4.1	Deformation in bond layer and PZT patch	67
4.2	2D schematic view of PZT structure interaction model	72
4.3	PZT-Structure Interaction Model	76
	(a) Aluminium block structure	76
	(b) Finite element model of a quarter of structure	76
4.4	Comparison of refined conductance signature with previous analytical model (Bhalla and Soh, 2004c)	78
	(a) Plot in 0-250 kHz range	78
	(b) Closer view in 150-250 kHz range	78
4.5	Comparison of refined susceptance signature with previous analytical model (Bhalla and Soh, 2004c)	79
	(a) Plot in 0-250 kHz range	79
	(b) Closer view in 150-250 kHz range	79
4.6	Comparison of admittance signature with previous analytical models (Zhou et al., 1996 (perfect bond); Bhalla and Soh, 2004c)	80
	(a) Conductance (G) vs Frequency	80
	(b) Susceptance (B) vs Frequency	80
4.7	Comparison of conductance of experimental data (Bhalla and Soh, 2004c) with proposed model	81
	(a) Normalized analytical conductance (Refined model)	81
	(b) Normalized analytical conductance (Bhalla and Soh, 2004c)	81
	(c) Normalized experimental conductance (Bhalla and Soh,	81

	2004c)	
4.8	Comparison of susceptance of experimental data (Bhalla and Soh, 2004c) with proposed mode	82
(a)	Normalized analytical conductance (Refined model)	82
(b)	Normalized analytical conductance (Bhalla and Soh, 2004c)	82
(c)	Normalized experimental conductance (Bhalla and Soh, 2004c)	82
4.9	Effect of mass of adhesive on signature	86
(a)	Conductance (G) vs Frequency	86
(b)	Susceptance (B) vs Frequency	86
4.10	Variation of shear stress in bond layer	88
4.11	Profile of interfacial shear stress distribution	89
(a)	Effect of mechanical damping of bond layer	89
(b)	Effect of bond layer thickness	89
4.12	Effect of bond layer's shear modulus on shear stress profile	90
4.13	Effect of inertia parameter $\bar{\alpha}$ on shear stress	90
4.14	Profile of effective strain ($S_{p,eff}$) over the length of PZT	91
4.15	Profile of interfacial effective strain distribution	92
(a)	Effect of shear modulus of bond layer	92
(b)	Effect of bond layer thickness	92
4.16	Effect of inertia parameter $\bar{\alpha}$ on effective strain	92
4.17	Variation of effective stress (T_{eff}) over the length of PZT patch	93
4.18	Influence of shear modulus of elasticity of bond layer on EMI signature	95
(a)	Conductance (G) vs Frequency	95
(b)	Susceptance (B) vs Frequency	95
4.19	Influence of bond thickness on EMI signature	95
(a)	Conductance (G) vs Frequency	95
(b)	Susceptance (B) vs Frequency	95
4.20	Influence of bond layer's damping on EMI signature	96

	(a) Conductance (G) vs Frequency	96
	(b) Susceptance (B) vs Frequency	96
4.21	Influence of sensor length on EMI signature	97
	(a) Conductance (G) vs Frequency	97
	(b) Susceptance (B) vs Frequency	97
4.22	Influence of electric voltage on EMI signature	98
	(a) Conductance (G) vs Frequency	98
	(b) Susceptance (B) vs Frequency	98
5.1	Comparison of conductance of experimental result with continuum shear lag model	104
	(a) Normalized analytical conductance (continuum model) for $h_s/h_p=0.417$ and $h_s/h_p=0.834$	104
	(b) Normalized experimental conductance for $h_s/h_p=0.417$ and $h_s/h_p=0.834$	104
5.2	Comparison of susceptance of Experimental result with continuum shear lag model	105
	(a) Normalized analytical conductance (continuum model) for $h_s/h_p=0.417$ and $h_s/h_p=0.834$	105
	(b) Normalized experimental conductance for $h_s/h_p=0.417$ and $h_s/h_p=0.834$	105
5.3	Comparison of conductance (G) plot	106
	(a) Plot in 0-250 kHz range	106
	(b) Closer view in 150-250 kHz range	106
5.4	Comparison of susceptance (B) plot	107
	(a) Plot in 0-250 kHz range	107
	(b) Closer view in 150-250 kHz range	107
5.5	Effect of mechanical loss of bond layer on new proposed admittance function	108
	(a) Conductance (G) vs Frequency	108
	(b) Susceptance (B) vs Frequency	108

5.6	Effect of shear modulus of bond layer on new proposed admittance function	109
	(a) Conductance (G) vs Frequency	109
	(b) Susceptance (B) vs Frequency	109
5.7	Effect of dielectric loss on new proposed admittance function	110
	(a) Conductance (G) vs Frequency	110
	(b) Susceptance (B) vs Frequency	110
5.8	Effect of dimension change (l^2/h) on new proposed admittance function	111
	(a) Normalized conductance vs Frequency	111
	(b) Normalized susceptance vs Frequency	111
5.9	Effect of combined mass (PZT and adhesive) effect on admittance signature	113
	(a) Conductance (G) vs Frequency	113
.	(b) Susceptance (B) vs Frequency	113
6.1	(a) Series combination of LCR Circuit the inductance (L), the resistance (R), and the capacitance (C).	116
	(b) Impedance triangle for LCR circuit	116
6.2	(a) Vector representation of voltage and current on complex plane	117
	(b) Power triangle	117
6.3	Apparent power consumption in piezo-impedance transducer	124
6.4	Reactive power consumption in piezo-impedance transducer	125
6.5	Active power consumption in piezo-impedance transducer	125
6.6	Comparison of maximum power requirement for piezo-structure interaction models	126
6.7	The efficiency of PZT patch to excite the piezo-active system	127
6.8	The real part of coupled signature illustrating how the active component of electrical power being consumed in electro-mechanical interaction process	128

6.9	Dissipative energy conversion efficiency ratio for integrated piezo-structural model	133
6.10	Reactive energy conversion efficiency ratio for integrated piezo-structural model	133

LIST OF TABLES

TABLE	CAPTION	PAGE NO.
3.1	Piezoelectric properties of PIC 151 (PI Ceramic, 2010).	51
3.2	Material properties of aluminium block and adhesive	59
3.3	Modal Frequencies of PZT bonded with host structure	59
4.1	Parameters of PZT patch, aluminum block and adhesive bond	77

LIST OF SYMBOLS

SYMBOLS	DESCRIPTIONS
$\overline{P_{eff}}$	2D Shear lag parameter for refined model
q_{eff}	2D Shear lag parameter for refined model
ε_0	Absolute dielectric permittivity
$ Y $	Absolute value of admittance
Z_a	Actuator impedance
W_A , W_R and W_D	Apparent, reactive and active power component for piezoelectric effect
V_0	Applied peak voltage
u_s	Average velocity in bond layer
F_1	Axial force
T_p	Axial force along x-direction
T_1	Axial stress
T_1 and T_2	Axial stress along x and y direction for 2D refined model
σ_x	Axial stress along x-direction
σ_y	Axial stress along y-direction
M_x	Bending Moment about x axis
η'	Bond layer damping
δA	Change in area
S_q^*	Circuit sensitivity
ω	Circular frequency
I	Combined inertia parameter
\bar{Y}	Complex admittance
η_{em}^*	Complex conjugate of piezo-mechanical loss

λ_1, λ_2 and λ_3	Complex cubic roots of refined shear lag equation
$\overline{Y^E}$	Complex Young's Modulus
$Z_{xx}, Z_{yy}, Z_{xy}, Z_{yx}$	Component of structural impedance for Zhou's model
G	Conductance
U_{con}	Continuum Displacement
ε_i	Corrected strain for shear lag effect (Sirohi and Chopra, 2000)
C_1, C_2	Correction factors for free PZT patch's signature
k_b and k_p	Correction factors to taken care for shear lag and Poisson's ratio for Sirohi and Chopra (2000)
Z_{ij}, Z_{jk}, Z_{ki}	Cross structural impedance for Ammandas and Soh (2007) Model
ρ	Density
ρ_s	Density of adhesive
ρ_p	Density of PZT Patch
$[K^d]$	Dielectric conductivity matrix
δ	Dielectric Loss of PZT Patch
Z_{si}, Z_{sj}, Z_{sk}	Direct structural impedance for Ammandas and Soh (2007) Model
u_{px}	Displacement along x-direction
u_{py}	Displacement along y-direction
k_r	Dielectric constant
\overline{K}_b	Dynamic stiffness of bond layer
\overline{K}_s	Dynamic stiffness of structure
T_{eff}	Effective axial stress
F_{eff}	Effective Force
$Z_{a,eff}$	Effective impedance of PZT patch

l_{eff}	Effective length
S_{eff}	Effective strain
u_{eff}	Effective velocity
Y_b	Elastic modulus of beam
E_3	Electric potential
E	Electric potential for coupled field analysis
V	Electrical degree of freedom
$\overline{\varepsilon}_{33}^T$	Electrical permittivity
N^V	Electrical Shape function
k_{eff}^2	Electro-mechanical coupling co-efficient
dm	Elemental inertia mass of PZT patch
λ	Energy conversion efficiency ratio
V_c	FE electrical degree of freedom
u_c	FE Structural degree of freedom
f_a	Frequencies at anti resonance point
f_r	Frequencies at resonance point
l	Half length of the PZT patch
u_0	Harmonic displacement
F_0	Harmonic force amplitude
\dot{u}_1	Harmonic velocity along x-direction
\dot{u}_2	Harmonic velocity along y-direction
\ddot{u}	Harmonic velocity amplitude
h_b	Height of beam
j	Imaginary
ξ	Impedance modification factor
$\bar{\alpha}$	Inertia parameter

β , F_d and F_s	Inertia, damping and spring force respectively
F_z	Inertial for bending actuation for Chang and Lim's model (2005)
\bar{I}	Instantaneous current
\bar{V}	Instantaneous voltage
$[M]$	Mass matrix
Z	Mechanical impedance
η	Mechanical loss factor of PZT patch
Z_{pxx}	Modified mechanical impedance along x-direction for Chen and Lim's Model (2005)
Z_{pyy}	Modified mechanical impedance along x-direction for Chen and Lim's Model (2005)
Z_p	Modified mechanical impedance for Chen and Lim's Model (2005)
$\bar{\alpha}'$ and $\bar{\beta}$	Modified shear lag parameter for combined inertia effect on 1D refined shear lag model
$\bar{\alpha}_{eff}$ and $\bar{\beta}_{eff}$	Modified shear lag parameter for combined inertia effect on 2D refined shear lag model
I_o	Peak current
V_0	Peak voltage
P_0	Perimeter of PZT Patch
ϕ	Phase angle
ϕ	Phase angle (power factor)
C	Piezo capacitance
$\lambda_{PZT-str}$	Piezo-dissipative energy conversion efficiency ratio
Q	Piezoelectric charge
D_3	Piezoelectric charge displacement
ρ_{piezo}	Piezoelectric charge displacement
$[K^z]$	Piezoelectric coupling matrix

$[C_v]$	Piezoelectric damping matrix
$[K]$	Piezoelectric stiffness matrix
d_{31}	Piezoelectric strain displacement
η_{em}	Piezo-mechanical loss factor
$\lambda_{PZT-elec}$	Piezo-reactive energy conversion efficiency ratio
ν	Poisson ratio
K_M and K_E	Proportionality factors for total mechanical and electrical energy for Liang et al. (1995)
Z_{res}	Resultant structural impedance
Γ	Shear lag parameter
q	Shear lag parameter for 1D refined model
ξ	Shear lag Ratio
G_s	Shear Modulus
τ	Shear stress
τ_{xz}	Shear stress along z axis in xz-plane
τ_{yz}	Shear stress along z axis in yz-plane
K_s	Static spring coefficient
S_b	Static strain in beam
S_p	Static strain in PZT patch
S_1	Strain
S_1	Strain along x-direction
S_2	Strain along y-direction
B_V	Strain-displacement matrix for electrical DOF
B_u	Strain-displacement matrix for structural DOF
$\{F\}$	Structural force
$[C_u]$	Structural damping matrix

u	Structural degree of freedom
Z_s	Structural impedance
y^2	Structural response (bending) for Liang et al., 1997
N^u	Structural shape function
S	Structural strain for FE coupled field analysis
B	Susceptance
\bar{T}	Tangent ratio
\vec{f}	Tangential Force
h	Thickness of PZT patch
h_p	Thickness of PZT Patch
t	Time
\hat{n}	Unit Vector
$A_1 A_2$ and A_3	Unknown coefficients for refined shear lag equation
$\{L\}$	Vector of nodal, surface and body charges
k	Wave number
k_p	Wave number for PZT patch
w	Width of PZT Patch

LIST OF ABBREVIATIONS

PZT	Piezoelectric Ceramic
SHM	Structural Health Monitoring
EMI	Electro-Mechanical Impedance
NDT&E	Non-destructive Technique and Evaluation
LCR	Inductance (L) Capacitance (C) Resistor (R) (Circuit)
RC	Reinforced Concrete
FE	Finite Element
FEA	Finite Element Analysis
RMS	Root Mean Square
DOF	Degree of freedom
PWAS	Piezo wafer active sensor
AC	Alternating Current

Chapter-1

INTRODUCTION

1.1 RESEARCH BACKGROUND

This research work focuses on the mechanics of the shear layer (adhesive bond layer) coupled between the piezo-impedance transducer and host structure during the electro-mechanical interaction for structural health monitoring (SHM) using the electro-mechanical impedance (EMI) technique. The fundamental scope of work is to develop a simple but rigorously accurate shear lag model with due consideration of all piezo-mechanical variables that influence the overall performance of the transducer. This has finally resulted into a continuum based coupled piezo-elastodynamic model, which ensures a rigorous integration of all shear lag (bonding effect) parameters over the entire sensor area, there by contributing in greater understanding of the phenomenon associated with EMI technique in the field of SHM. The key issues like power consumption and energy efficiency have been studied with the aid of the new model for optimized utilization of the piezo sensor.

1.2 MOTIVATION

Civil infrastructures need timely inspection for the assessment of their integrity and stability for the future benefit of the human society, life safety and cost effectiveness. Their safe and economical performance stands a high benefit for the society, because it stabilizes financial management and safety. In general, their performance contains a large number of uncertainties because they are often subjected to traumatic natural disasters and intensive usage. To overcome these challenges, many organizations and independent research bodies comes up with new techniques for full scale performance assessment and behavioural interpretation of structures, which is termed as structural health monitoring (SHM).

The term SHM originated in the early of 19th century, quite before it had been widely used for practical applications including various non-destructive techniques and evaluation (NDT&E). Basically, SHM denotes the process of acquisition, validation and interpretation of a set of structural data, collected from the structure at different times to facilitate life time risk management decisions (Kesseler, 2002). Health monitoring is typically used to track and evaluate the performance, symptoms of operational incidents and anomalies due to deterioration or damage during operation and after extreme events (Aktan et al., 1998). For any kind of structures, including civil, aerospace, and mechanical engineering infrastructure, SHM is the process of detecting damage, while the structure is in service (Inman, 2005). In contrast to SHM, the non-destructive evaluation (NDE) techniques, such as dye penetrant inspection, magnetic inspection, eddy-current inspection, radiography, and ultrasonic inspection are performed while the system of interest in service (Doherty, 1987).

The ultimate achievement of SHM can be categorized into two aspects; one is “real-time”, which enables the SHM system to obtain immediate response of the structure and hence measures the health of structure. The other feature is “on-line”, which provide us alerting system by audible sound and online imaging. Modern SHM integrates sensing (smart materials), communication and computing systems combined with NDT&E, such as geometric surveys and vibration measurements. The academic research community is greatly attracted towards vibrational response of structures using smart materials or conventional sensors to identify the modal characteristics, which are sensitive to structural damages. These modal parameters reflect the structure’s mass, stiffness and damping properties along with imposed boundary conditions. Changes in modal properties indicate a change in the structure caused by deterioration or defects occurring in the structure, thus enabling damage quantification. A mature SHM system has the potential to be fully integrated into the

operational hardware of a structure. If a defect is sensed, the system should have the intelligence to determine the best course of action.

1.3 SMART MATERIALS AND STRUCTURES

The definition of smart materials or structures is widely varied across the research community. Previously, the words ‘intelligent’, ‘adaptive’ and ‘organic’ were used to characterize the smart system (Rogers, 1988a). However, the workshop organized by US Army Research Office, unanimously agreed to adapt a single term as ‘smart’ which was defined as:

A system or material which has built-in or intrinsic sensor(s), actuator(s) and control mechanism(s) whereby it is capable of sensing a stimulus, responding to it in a predetermined manner and extent, in a short/ appropriate time, and reverting to its original state as soon as the stimulus is removed.

The idea of smart structures has been adopted from nature, where all living organisms possess a system of distributed sensory neurons running all over the body, enabling the brain to monitor the condition of the various body parts (Rogers, 1990). Smart structures have these essential components namely “*sensors*”, “*actuators*”, and “*control mechanism*”. In addition, “*timely response*” is the fourth qualifying term as recognized by (Rogers, 1988b). The combination of above terms enables us to formulate ‘*smart system*’ which can be used at both macroscopic (structure) and microscopic (material) level. Smart materials possess adaptive capabilities to external stimuli, such as loads or environment, with inherent intelligence. In the US Army Research Office Workshop, Rogers et al. (1988a) defined the smart materials as *materials, which possess the ability to change their physical properties in a specific manner in response to specific stimulus input*. The stimuli could be pressure, temperature, electric and magnetic fields, chemicals or nuclear radiation. The associated with changeable physical properties could be shape, stiffness, viscosity or damping. Smart materials such as

piezoceramic patches, sharp memory alloys, fiber-optic sensor, electro-rheological fluids and electro-magnetic fluids facilitate us to build stimulus-response system with much higher resolution than any conventional NDE techniques. In the recent past, Lead zirconate Titanate (Pb_2ZnO_3) piezoceramic (PZT) materials have emerged as front runner materials for SHM. PZT patches utilize the well known piezoelectric effect discovered by Pierre Curie and his brother in 1880. The basic mechanism can be explained as follow

Piezoelectric effect occurs by the displacement of ions, causing the electric polarization of the crystal's structural units. When an electrical field is applied, the ions are displaced by electrostatic forces, resulting in the mechanical deformation of the whole crystal (Encarta Concise Encyclopedia, 2012)

Because PZTs are ceramics, they can be produced in any shape or size, to suit the particular application. The piezoelectric effect provides the ability to use these materials as both sensors and actuators. Strain, for example, can be measured by capturing the voltage created across the PZT material when it is strained. As a sensor, these materials can also be used for damage detection in structures in which they are embedded or surface bonded. Piezoceramics can also be used as actuators because they undergo strain or displacement when an electric voltage is applied across their poling axis. This makes PZT patches good candidates for SHM or active control systems. They are also used as structural dampers because of their ability to transform mechanical energy to electrical energy and vice versa. Since this thesis is primarily concerned with piezoelectric materials and some typical applications i.e. EMI technique, shear lag effect and piezoelectric power and energy issues are our major area of interest.

1.4 BASICS OF EMI TECHNIQUE

The piezoelectric patches have emerged as high frequency mechatronics transducers for SHM (Sun et al., 1995; Ayres et al., 1998; Liang et al., 1994, 1995, 1996; Soh et al., 2000;

Park et al., 2000, 2003, 2008; Lim et al., 2006; Bhalla, 2001; Bhalla and Soh, 2003, 2004a, b, c.; Bhalla et al., 2005, 2009; Annamdas, 2007; Shanker et al., 2011). In this application, the PZT transducers, bonded on the surface of the structure, interact with the host structure to acquire unique health signature, which is function of the structural impedance. For this purpose, they are subjected to high-frequency excitations of electric field using impedance analyzer or LCR meter. Because of the direct and the converse piezoelectric effects, any change in the mechanical impedance of the structure caused by any damage, modifies the electrical admittance of the PZT transducer bonded to it. The technique is popularly called as the EMI technique. Usually, the electro-mechanical admittance signature, comprising of the conductance (real part) and the susceptance (imaginary part) is acquired in the healthy condition of the structure and used as the reference baseline for future checks on the structural integrity. The EMI technique has been shown to be extremely sensitive to incipient damages. The PZT patches can be easily bonded to inaccessible locations of structures and aircraft and can be interrogated as and when required, without necessitating the structures to be placed out of service or any dismantling/re-assembling of the critical components (Rogers et al., 1998b). All these features definitely give an edge to the EMI technique over other existing passive sensor systems.

Since the patch is attached directly to the structure of interest, it has been shown that the mechanical impedance of the structure correlates with the electrical impedance of the patch (Liang et al., 1994, 1995). Using the EMI technique, damage detection feasibility studies have been successfully conducted on a variety of structures ranging from simple beams, plates to bridge truss structures, airplane composites, pipeline structures and reinforced concrete (RC) structures. Different damage mechanisms such as cracking, bolt loosening, composite delaminations and corrosion are successfully detected. A great deal of emphasis

has been placed on using the EMI technique for aerospace related structures (Peairs et al., 2004).

Traditionally, the EMI technique requires the use of an impedance analyzer or LCR meter, which is used to measure and analyze impedance in electrical components and systems. Impedance analyzers generally measure electrical impedance precisely (as well as capacitance, inductance, resistance, etc.) over broad frequency ranges with extensive functionality and display options. In addition to the EMI technique, other applications of PZT transducers are too abundant to list; however, they are mainly used in the fields of ultrasonic (Yamashita et al., 2002), noise and vibration control (Wu et al., 1994; Han et al., 1997) and acoustic emissions etc. (Prabakar and Mallikarjun, 2005). The present form of the EMI technique is still relatively new, and some of its impending issues like wireless signature acquisition through new technological advancements, energy harvesting, inclusion in bio sensing field, application and extensive use of Macro-Fiber Composite (MFC), development of low-cost piezoelectric device for controlling vibration noise and deflections in composite beams and panels, accurate dynamic analysis for bonding effects, power and energy issues and frequency spectrum analysis are still attracting research field.

1.5 SHEAR LAG EFFECT

In the EMI technique based SHM, the PZT patches are either embedded or bonded with adhesive to the host structure to be monitored. When bonded on the surface of the structure, the adhesive bond forms an interfacial layer of finite thickness between the patch and host structure. Since the adhesive does not change the material properties of adherents, attaching the PZT patches with adhesives has a broad range of applications than other bonding method (Wang and Zeng, 2008). The performance (sensing/actuating) of piezo transducer depends upon the ability of the bond layer to transfer the stresses and strains between the active PZT patch and the host structures. The mechanical and geometrical properties of the adhesive

bond layer change the overall performance of the PZT-structure interaction model (Dugnani, 2009). The coupled EMI response of the PZT transducer very much depends on the dynamic behaviour of the host structure as well as the geometry, mechanical properties and the composition of the adhesive layer used to bond the patch.

As far as the EMI technique is concerned, the adhesive is capable of changing the structural signature by lowering the peaks of the conductance and the slope of the suscepantce, as reported by various researchers (Bhalla et al., 2004c; Qing et al., 2006; Dugnani, 2009; Bhalla et al., 2009). As bond layer is solely responsible for changing the coupled signature, the bond characteristics (shear deformation, inertia, mechanical damping) and geometry (bond thickness and bond length) must be chosen so as to ensure best performance of the PZT transducer. However, the existing shear lag models do not account for shear and inertia effects simultaneously as well as the continuous bond deformation variation along bond length. The main objective of this research is to alleviate these shortcomings by accurate modelling of the entire phenomena. These understandings will play significant role to apply the EMI technique on practical structures more effectively.

1.6 POWER AND ENERGY CONSUMPTION FOR BONDING EFFECT

When an active and dynamic piezo-impedance transducer is engaged in the EMI technique, it acts as both sensor and actuator (dual effect) for a range of frequency and couples the electrical and the mechanical parameters. Integrated induced strain actuators provide the energy for intelligent material systems and structures to respond adaptively to internal or external stimuli. The electrical energy consumed in piezo-impedance transducer can be described in accordance with their applications, i.e. whether it is used for shape control, vibration control, or acoustic control, as well as the associated electronic systems, including the power supply itself. In our prospect, we will not include the power supply system in the coupled electro-mechanical analysis by assuming that the power supply system can always

satisfy the current need of the actuators (Liang, et al., 1994, 1995). For a material system with integrated PZT patches, the power consumed by patch consist of two parts: the energy used to drive the system, which is dissipated in terms of heat as a result of the structural damping, and energy dissipated by the PZT patches themselves because of their dielectric loss and internal damping (Liang et al, 1994, 1995, 1996). This issue was noticed in the early development and implementation of PZT patches. However, the effect of finite thickness bond has not yet been studied in power computation involving the PZT patch.

Several static-based modeling techniques were developed to determine static forces or moments (Bailey and Hubbard, 1985; Crawley and Luis, 1987, Crawley and Anderson, 1990; Dirmitriadi et al., 1989; Wang and Rogers, 1991). An approximate dynamic analysis using the static models is not accurate because active forces provided by the PZT actuators are usually harmonic in nature. The dynamic interaction between the host structure and the active elements always exists and affects the performance of both the structure and the patch. Various impedance-based analytical models provide a platform for understanding the mechanics of the PZT element-driven systems (Liang et al., 1994; Zhou et al., 1993, 1994). The frequency-dependent force output behavior is accurately predicted by the impedance model.

When a PZT patch is integrated with active mechanical system, energy conversion efficiency factor is required to quantify the efficiency of the piezo-active system which depends upon the mechanical damping, intermolecular bonding between the patch and the structure (with adhesive bond), structural stiffness, piezo-electric properties of the patch and the imposed boundary condition. In this research, the power and energy efficiency aspects have been deeply explored using the developed piezo-bond elasto-dynamic model. The computation is expected to result in more accurate quantification as compare to previous models with due consideration of bond effect.

1.7 VARIOUS SHM TECHNIQUES: A COMPARISION

SHM is defined as the acquisition, validation and analysis of technical data to facilitate life cycle management decisions (Aktan, 2000). It denotes a reliable system with ability to detect and interpret adverse “changes” in a structure due to damage or normal operations (Kessler et al., 2002). The SHM system consists of sensor, actuator, amplifiers and signal conditioners. The recent developments in the area of smart materials and systems have initiated new openings for SHM and NDE. Smart materials, such as the piezoceramics, the shape memory alloys and the fiber optics materials are extensively used for SHM. In broad sense the SHM techniques can be divided in to two categories.

- a) Global SHM techniques
- b) Local SHM techniques

1.7.1 *Global SHM:*

These can further sub divided in two cases- dynamic and static. In global dynamic techniques, the test structure is subjected to low frequency excitation, either harmonic or impulse and the resulting vibration responses (displacement, velocity and accelerations) are picked at specified locations along structure. The vibration data is processed for first few mode shapes and the corresponding natural frequencies, which, when compared with corresponding data for healthy state, yield information pertaining to the location and severity of damage (Pandey et al., 1991; Stubbs and Kim, 1994; Zimmerman and Kaouk, 1994; Naidu, 2004). Being global in nature, it is not very sensitive to incipient damage (Pandey and Biswas, 1994; Farrer and Jauregui, 1998).

1.7.2 *Local SHM:* As opposed to global SHM techniques, numerous local SHM methods are available, which rely on localized structural interrogation for detecting damages. Some of the techniques in this category are ultrasonic techniques, acoustic emissions, eddy currents, impact echo testing, magnetic field analysis and penetration dye testing (Boller, 2000; Park,

2000; Giurgiutiu and Rogers, 1997). A common limitation of local methods is usually, probes, fixtures and other equipment need to be physically moved around the test structure for recording data. Beside these, the wave propagation based SHM has also attracted wide attention in recent years. This technique employs PZT patches as actuator-sensor pairs, on the other side, in EMI technique the dual effect (acts as both actuator and sensor) of PZT is utilized. The wave propagation dynamics (reflection, refraction and transmission) governs the damage detection and localization (Gopalkrishnan et al, 2008, 20011). However, the guided wave NDT is limited to simple structure because of complicated and huge data interpretation. Also, it is observed that sensitivity decreases with propagation distance and sensor spacing (Grisso, 2004).

Fiber optic sensors, which were originally used for communication, have recently emerged as new sensors for SHM (Meltz et al., 1989; Kersey at al., 1997; Wan and taylor, 2003; Tjin et al., 2001). Their use has been demonstrated for various monitoring application. The fiber optic sensors are made up of glass and silica and utilize fiber properties to generate optoelectronics signals indicative of external parameters to be measured. Any mechanical strain in the fibre will shift the wave length through expansions/contraction of periodicity. The major limitation of the fiber optic sensors is fragility and inability to monitor at high frequency dynamic strain (Tjin et al., 2004). In addition, contrary to PZT patches, the fiber optic sensoes are passive in nature.

A very thorough review of SHM technique is covered by Park (2004), Naidu (2004), Bhalla (2004) and Shanker (2010) in their thesis.

1.8 THESIS ORGANIZATION

This thesis is divided into eight chapters. Chapter-1 (present chapter) consists of introduction, objectives, scope and summarizes the original contributions of the research. It contains brief

description of smart materials and structures, EMI technique and its applications in SHM, inclusion of shear lag mechanism and power and energy issues for the piezo-active model. The Chapter-2 discusses the literature review and the working principle of impedance and the EMI technique. Literature related to shear lag effect and coupled field Modelling for piezo-impedance transducer has also been covered in this chapter.

Chapter-3 presents preliminary investigations of shear lag effect based on coupled finite element (FE) analysis. It covers the FE coupling theory for piezoelectric analysis and FE modelling steps for ANSYS. Various parametric studies are also included in this chapter to illustrate the piezo-structure interaction numerically.

The detailed derivation of new refined shear lag model and its experimental verification with supported parametric study has been covered in Chapter-4. The corresponding shear stress and strain profile along the adhesive bond layer and their interpretations for SHM application are also included in this chapter.

Chapter-5 deals with the derivation of new and modified continuum based admittance model and compares its performance with previous models. Effect of parametric variation of bond properties on the EMI signature have also been studied in this chapter.

Chapter-6 deals with the power consumption and energy efficiency of the PZT patch based on new continuum model. The triangular component of power and its interconnection with piezo-energy flow in physical system has been elaborated in this chapter. Modified efficiency ratio and electro-mechanical co-efficient has derived in this chapter. The performance assessment of piezo-structural interaction system for various piezo-mechanical losses has also been covered in this chapter.

Finally, conclusions and recommendations are presented in Chapter 7, which is followed by a list of author's publications, a comprehensive list of references and appendices.

Chapter-2

IMPEDANCE BASED MODELLING OF PIEZO-STRUCTURE INTERACTION

2.1 INTRODUCTION

The most popular approach in SHM is to use modal parameters, such as natural frequencies, damping ratios and mode shapes, to determine the existence of damage in structures. Other modal properties, such as eigen vector and eigen value matrices, curvature mode shapes, modal assurance criterion, energy transfer ratio and many others, have also been explored for damage detection (Pandey and Biswas, 1994; Kawiecki, 2001). Aktan et al. (1998) has reported an extensive survey of SHM on civil infrastructures health monitoring. Several researchers have attempted to develop non-modal approach for SHM, the wave propagation approach being one of them. In this approach, global defects can be detected by a change in the wave number-frequency relation and local defects by a change in the scattering stiffness matrix elements.

In general, SHM or damage detection techniques based on the vibration response of the structure can be classified into two categories: model based (which require a model of the structure to start with) and non model based (in which model is not pre requisite). The impedance-based technique belongs to the non model based category. Most of the current work in the impedance based SHM is focused on adapting the EMI technique for application on real world structures. This involves miniaturization of the data acquisition hardware, combination with wireless telemetry and addressing powering issues including energy harvesting techniques. The basic concept of the EMI technique is to monitor the variations in mechanical impedance of structure caused by the occurrence of damage. Since the measurement of mechanical impedance of structure is very difficult, especially at high frequency, the EMI technique utilizes the

electromechanical coupling property of the PZT patch bonded on the structure. Through this coupling property, the electrical admittance of the PZT patch is directly related to the mechanical impedance of the host structure, and is directly affected by the occurrence of structural damage. The major advantage of this electro-mechanical coupling is that even small changes in the natural frequency (caused by damage) can be used to create beat phenomena, which causes a large response to the small changes in frequency and is thus highly sensitive.

A global-based technique may assess damage quantitatively if the model is appropriate. However, it is difficult to apply it on complex structures for which we can hardly generate a satisfactory model. In contrast, the EMI technique is sensitive enough to detect very small damage and can be applied on complex structures. Sun et al. (1995) first detected damage in a lab-sized truss structure using the EMI technique. Recently, the EMI technique has been increasingly tested on civil and mechanical structures (Varadan and Varadan, 2002; Park et al., 2000a, b; Soh et al., 2000; Bhalla, 2001) as well as aerospace structures (Chaudhary et al., 1995; Giurgiutiu, 2000; Giurgiutiu and Zagrai, 2002; Ghoshal et al., 2001). Bhalla and Soh (2004a, b) proposed a damage quantification approach, based on identifying the equivalent system parameters from signatures. This approach utilized both real and imaginary components of the signature and paved way for identifying the system parameter from experimental data, enabling parametric damage quantification.

2.2 EMI BASED STRUCTURAL HEALTH MONITORING

The EMI-based SHM technique utilizes piezoelectric materials as sensors and actuators. For piezoelectric materials, the relation between the mechanical and electrical variables is governed by the following constitutive equations

$$D_3 = \overline{\varepsilon_{33}^T} E_3 + d_{31} T_1 \quad 2.1(a)$$

$$S_1 = \frac{T_1}{\overline{Y^E}} + d_{31} E_3 \quad 2.1(b)$$

where T_1 is stress, d_{31} the piezoelectric strain displacement, S_1 and D_3 the actuating strain along axis (1) (see Figure. 2.1) and the piezoelectric charge displacement respectively, E_3 the electric field along axis (3), $\overline{Y^E}$ and $\overline{\varepsilon_{33}^T}$ are the complex young's modulus at constant electric field and the complex electric permittivity matrix of PZT material. The EMI technique utilizes a small PZT patch attached to the host structure to impart a harmonic force on the structure by applying an electric field (AC voltage signal) across the patch. The structural response comprises of peaks and valleys in 'admittance vs frequency' plot, which is known as the electro-mechanical (EM) 'admittance signature'. If damage occurs in the structure, its mechanical impedance will change, which will modify the admittance signature, thereby providing indication of the damage. The next paragraph defines mechanical impedance of the structure and the patch for use in EMI technique.

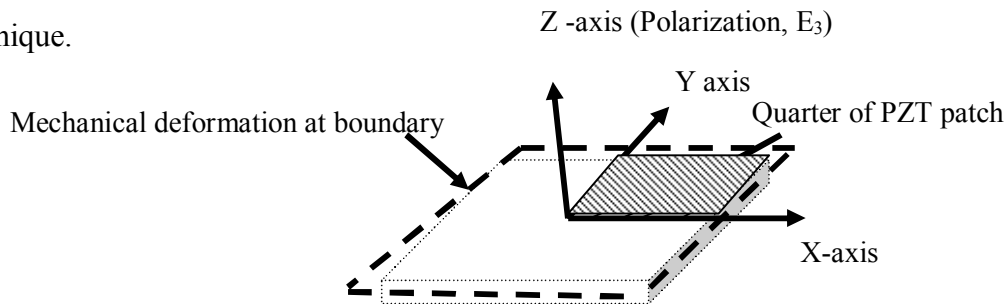


Figure 2.1 A deformed PZT patch

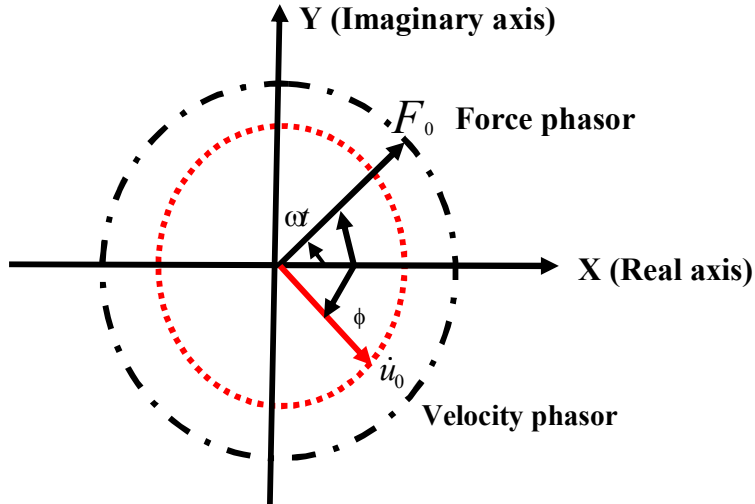


Figure 2.2 Representation of harmonic force and velocity by rotating phasor (Bhalla, 2004)

A harmonic force, acting upon a structure, can be represented by a rotating phasor on a complex plane, as shown in Figure 2.2 (Bhalla, 2004). Let F_o be the magnitude of the phasor and let it be rotating anti-clockwise at an angular frequency ω (same as the angular frequency of the harmonic force). At any instant of time ' t ', the angle between the phasor and the real axis is ' ωt '. The instantaneous force (acting upon the structure) is equal to the projection of the phasor on the real axis i.e. $F_o \cos \omega t$. The projection on the ' y ' axis can be deemed as the 'imaginary' component.

Using complex notation, the force can be presented

$$F(t) = F_0 \cos \omega t + jF_0 \sin \omega t = F_0 e^{j\omega t} \quad (2.2)$$

The resulting velocity response \dot{u} , at the point of application of the force, is also harmonic in nature. It lags behind the applied force by a phase angle ϕ , due to the 'mechanical impedance' of the structure, and can be expressed as

$$\dot{u} = \dot{u}_o e^{j(\omega t - \phi)} \quad (2.3)$$

where \dot{u}_0 is the peak velocity. The mechanical impedance of a structure, at any point, is defined as the ratio of the driving harmonic force to the resulting harmonic velocity, at that point, in the direction of the applied force. Mathematically, the mechanical impedance Z_s , can be expressed as

$$Z_s = \frac{F}{\dot{u}} = \frac{F_0}{\dot{u}_0} e^{j\phi} \quad (2.4)$$

As a general practice, the mechanical impedance of a PZT patch is determined in short circuited condition, as shown in Figure. 2.3, so as to eliminate the piezoelectric effect and to invoke pure mechanical response alone.

If F is the force applied on the PZT patch, then from Eq. (2.4), the short-circuited mechanical impedance of the patch, Z_a , can be determined as

$$Z_a = \frac{F_{(x=l)}}{\dot{u}_{(x=l)}} = \frac{whT_{1(x=l)}}{\dot{u}_{(x=l)}} = \frac{wh\overline{Y^E}S_{1(x=l)}}{\dot{u}_{(x=l)}} \quad (2.5)$$

where \dot{u} is the he velocity response and l , w and h are the dimensions of the patch as shown in Figure. 2.3. It should be noted that we are considering one symmetrical half of the PZT patch only, that is l = half length.

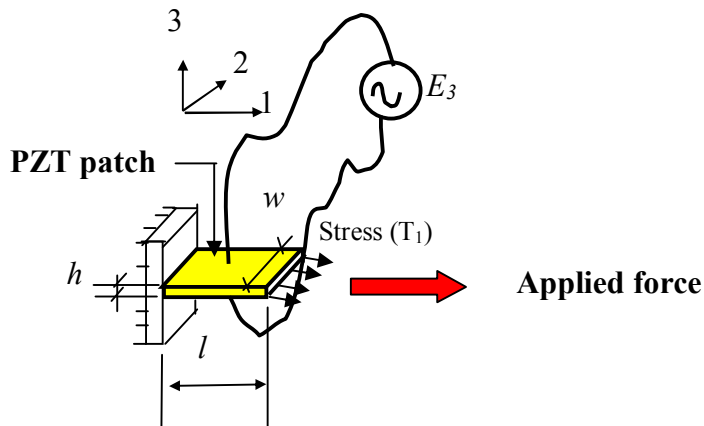


Figure 2.3 Determination of mechanical impedance PZT patch

2.3 PIEZO-STRUCTURAL INTERACTION MODELLING FOR EMI TECHNIQUE

In the EMI technique, on application of an alternating voltage across a bonded PZT patch, deformations are produced in the patch as well as in the local area of the host structure surrounding it. The response of this area to the imposed mechanical vibrations is transferred back to the PZT wafer in the form of electrical response, as conductance and susceptance signatures. As a result of this interaction, the structural characteristics are reflected in the signatures. Though the EMI technique does not demand a prior knowledge of the structure in terms of model, understanding of the PZT-structure interaction becomes necessary for improving the damage prognosis using EMI technique. Additional benefits of such knowledge are optimization of the frequency range and the sensor location when designing the SHM system and allowing better insight into sensor self-diagnostics, transfer impedance and other related issue.

Several approaches have been proposed to model PZT-structure interaction in general. The earliest effort was the static approach, which was later followed by the impedance (dynamic) approach. Some important early modelling approaches are briefly described in this following subsection.

2.3.1 Static Approach

Crawley and de Luis (1987) analytically modelled PZT patch as a part of an intelligent structure. The model is capable of reasonably predicting the response of a structural member under an applied voltage under low frequency and could provide guidance for optimal location of sensor. They performed static analysis for two cases (i) perfectly bonded patch and (ii) finite bonding layer. In either case, the ends of the patch are stress-free and the patch is assumed to have a uniform strain through its thickness.

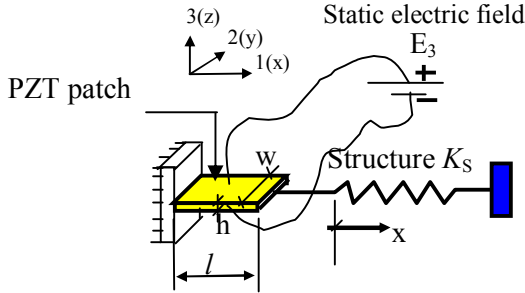


Figure 2.4 Modelling of PZT-structure interaction by static approach

Crawley and de Luis (1987) modelled piezo patch to be attached to the structure, represented by spring (K_s) excited by static electric field (E_3), as illustrated in Figure 2.4. They determined the static force or moment using Euler-Bernoulli's beam equation. In this configuration, owing to static condition, the imaginary component of the complex term in the PZT constitutive relation (Eqs. 2.1(a) and (b)) can be dropped. The axial force in the PZT patch can be expressed as

$$F_p = whT_1 = wh(S_1 - d_{31}E_3)Y^E \quad (2.6)$$

where T_1 and S_1 are the stress and strain for static case. Similarly, the axial force in the structure can be determined as

$$F_s = -K_s x = -K_s l S_1 \quad (2.7)$$

where x and K_s are the spring displacement and spring constant. The negative sign signifies that a positive displacement in PZT patch causes compressive force in the spring (the host structure). From force equilibrium, they derived the equilibrium strain, S_{eq} as

$$S_{eq} = \frac{d_{31}E_3}{\left(1 + \frac{K_s l}{Y^E w h}\right)} \quad (2.8)$$

In order to determine the response of the system under an alternating current, the static approach recommends that a dynamic force with amplitude $F_s = K_s l S_{eq}$ be applied to host structure,

irrespective of the frequency of actuation. Since the approach employs only static PZT properties, the effect of damping and inertia, which significantly affect PZT output characteristics especially under high frequencies, are completely ignored.

Lin and Rogers (1993) developed another static impedance model using elasticity approach with variation of non-linear distribution of the equivalent force and the moment. But Static stiffness approach is not accurate since the performance of the actuator and the structure, vary with frequency. Hence, this approach is only suitable for preliminary computation.

2.3.2 Impedance Approach

The impedance approach was proposed by Liang et al. (1994). In this approach, the whole system is modelled as a PZT patch attached to structural impedance Z_s , as shown in Figure 2.5. Liang et al. (1994) validated their model experimentally, which was further used to determine the actuator power consumption and energy flow in the coupled electro-mechanical system. The patch undergoes axial vibrations under an alternating electric field E_3 . The mechanical impedance of the structure can be related to the force F by

$$F = -Z u \quad (2.9)$$

where u is the velocity at the tip of the patch. The one-dimensional vibrations of the PZT patch are governed by the dynamic equilibrium equation given by

$$\overline{Y^E} \frac{\partial^2 u}{\partial t^2} = \rho \frac{\partial^2 u}{\partial x^2} \quad (2.10)$$

where u is the displacement at any point on the patch and $\overline{Y^E} = Y^E(1 + \eta j)$ is complex Young's modulus of the PZT patch (at constant electric field), where η the mechanical loss factor.

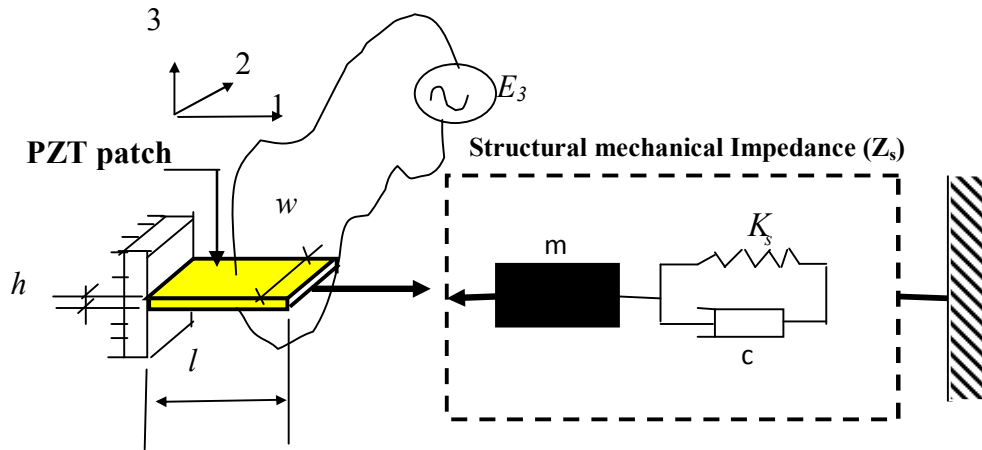


Figure 2.5 Liang's 1D impedance model

The solution of the one-dimensional (1D) governing differential equation (Eq. 2.10) is given by

$$u = (A \sin kx + B \cos kx) e^{j\omega t} \quad (2.11)$$

where k is the wavenumber, related to the angular frequency of excitation ω , the density ρ and the complex Young's modulus of elasticity of the patch by

$$k = \omega \sqrt{\frac{\rho}{Y^E}} \quad (2.12)$$

Hence, strain and velocity in PZT patch can be determined by solving the differential equation (2.10), expressed as (Liang et al., 1994)

$$s_1(x) = \frac{\partial u}{\partial x} = A e^{j\omega t} k \cos kx \quad (2.13)$$

and velocity

$$\dot{u}(x) = \frac{\partial u}{\partial t} = A j \omega e^{j\omega t} k \cos kx \quad (2.14)$$

Equation (2.9) can be rewritten as

$$F = -Z \dot{u} = wh T_1 \quad (2.15)$$

Making use of fundamental piezo constitute relations (Eq. 2.1(a) and (b)) and the expressions for strain (Eq. 2.13) and velocity (Eq. 2.14) and applying the boundary condition ($u=0$ at $x=0$), we can derive

$$A = \frac{Z_a V_0 d_{31}}{hk \cos(kl)(Z + Z_a)} \quad (2.16)$$

where Z_a is the short circuited mechanical impedance of the PZT patch and V_0 is the peak harmonic voltage, Z_a can be derived using Eq. (2.5) as

$$Z_a = \frac{k\omega \overline{Y^E}}{(j\omega) \tan(kl)} \quad (2.17)$$

The electric current, which is the time rate of change of charge, can be obtained as

$$\bar{I} = \iint_A \dot{D}_3 dx dy = j\omega \iint_A D_3 dx dy \quad (2.18)$$

Making use of the PZT constitutive relation (2.1(a)) and integrating over the entire surface of the PZT patch, Liang et al. (1995) obtained following an expression for the electro-mechanical admittance

$$\bar{Y} = \omega j \frac{wl}{h} \left[\left(\bar{\epsilon}_{33}^T - 2d_{31}^2 \overline{Y^E} \right) + \left(\frac{Z_a}{Z_s + Z_a} \right) d_{31}^2 \overline{Y^E} \left(\frac{\tan kl}{kl} \right) \right] \quad (2.19)$$

where $\overline{\epsilon_{33}^T} = \epsilon_{33}^T (1 - \delta j)$ the complex electric permittivity (at constant stress), where δ denotes the dielectric loss factor

Zhou et al. (1996) extended the formulations of Liang et al. (1994) to model the PZT element coupled to a two-dimensional (2D) host structure shown in Figure 2.6. They replaced the single term Z_s by a matrix consisting of the direct impedances Z_{xx} and Z_{yy} , and the cross impedances Z_{xy}

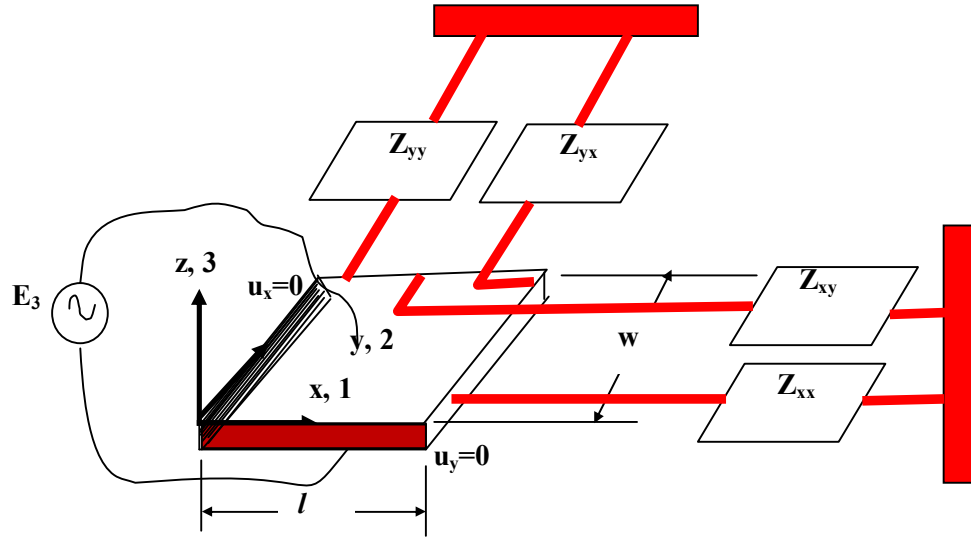


Figure 2.6 2D impedance model of Zhou et al. (1996)

and Z_{yx} , related to the planar forces F_1 and F_2 (along axes 1 and 2, respectively) and the corresponding planar velocities \dot{u}_1 and \dot{u}_2 , by

$$\begin{bmatrix} F_1 \\ F_2 \end{bmatrix} = - \begin{bmatrix} Z_{xx} & Z_{xy} \\ Z_{yx} & Z_{yy} \end{bmatrix} \begin{bmatrix} \dot{u}_1 \\ \dot{u}_2 \end{bmatrix} \quad (2.20)$$

They derived following expressions for dynamic equilibrium of an infinitesimal PZT element for 2D case (De Faria, 2003)

$$\frac{\partial \sigma_x}{\partial x} + \frac{\partial \tau_{xy}}{\partial y} = \rho_p \frac{\partial^2 u_{px}}{\partial t^2} \quad 2.21(a)$$

$$\frac{\partial \sigma_y}{\partial y} + \frac{\partial \tau_{yx}}{\partial x} = \rho_p \frac{\partial^2 u_{py}}{\partial t^2} \quad 2.21(b)$$

Dropping the shear stress term, The solution for 2D case was derived by Zhou et al. (1996) as

$$u_1 = [A \sin(k x_p) + B \cos(k x_p)] e^{j\omega t} \quad 2.22(a)$$

$$u_2 = [C \sin(k y_p) + D \cos(k y_p)] e^{j\omega t} \quad 2.22(b)$$

where wave number k for 2D case can be defined as

$$k = \omega \sqrt{\frac{\rho(1-\nu^2)}{Y^E}} \quad (2.23)$$

Applying boundary conditions $u_1=0$ at $x=0$ and $u_2=0$ at $y=0$, the unknown coefficients A , B , C and D can be evaluated. Finally, they obtained an expression four complex electro mechanical admittance signature for the 2D case as

$$\bar{Y} = j\omega \frac{wl}{h_p} \left\{ \begin{array}{l} \mathcal{E}_{33}^T - \frac{2d_{31}^2 \bar{Y}^E}{(1-\nu)} + \frac{d_{31}^2 \bar{Y}^E}{(1-\nu)} \left[\begin{array}{cc} k \cos(kl) \left(1 - \nu \frac{w}{l} \frac{Z_{xy}}{Z_{axx}} + \frac{Z_{xy}}{Z_{axx}} \right) & k \cos(kw) \left(\frac{l}{w} \frac{Z_{xy}}{Z_{axx}} - \nu \frac{Z_{yy}}{Z_{ayy}} \right) \\ k \cos(kl) \left(\frac{l}{w} \frac{Z_{xy}}{Z_{axx}} - \nu \frac{Z_{xx}}{Z_{axx}} \right) & k \cos(kw) \left(1 - \nu \frac{l}{w} \frac{Z_{yx}}{Z_{ayy}} + \frac{Z_{yy}}{Z_{ayy}} \right) \end{array} \right] \begin{pmatrix} 1 \\ 1 \end{pmatrix} \end{array} \right\} \quad (2.24)$$

The main limitation of Zhou's model is that, it is difficult to determine structure's mechanical impedance experimentally. This is because it consist four complex unknowns (Z_{xx} , Z_{yy} , Z_{xy} and Z_{yx}) (eight real unknowns) with two available equations, thus rendering the system of equation to be highly indeterminate.

Giurgiutiu and Rogers (1999) developed a theoretical model for the EMI response of a damaged composite beam interrogated by a PZT patch. The effective axial force and bending moments induced by the PZT wafer into the beam were considered. The resulting response and the applied force were utilized to deduce general expressions for pointwise dynamic stiffness and compliance. They concluded that the real part of the impedance and the real part of the coupled admittance are direct measures of the structural response.

Park et al. (2000b) modelled piezo bonded 1D structure using the wave propagation approach. Direct frequency response function data were utilized to detect and locate damage in the structure. They derived spectral formulation for a dynamic finite element, referred to as the spectral finite element or the dynamic stiffness matrix formulation, suitable for high frequency analysis. This technique was shown to be more useful in identifying and tracking small defects,

in the sense that damage is local phenomena and a high frequency effect. However, high frequency modes are subjected to higher uncertainty than the lower order modes, and this limits the application of the approach, although recently laser vibrometer has been shown to be capable of high frequency measurement, its application is limited to small structures and is quite cumbersome for large structure analysis (Giurgiutiu and Zagrai (2000)). Giurgiutiu and Zagrai (2000) developed a model for free, fully constrained and elastically constrained piezoelectric patch, excited at very high frequencies (up to 1500 kHz). However, the impedance response of the sensors attached to a beam structure was modelled and experimentally verified only up to 30 kHz only and on plates up to 40 kHz only.

Bhalla and Soh (2003) proposed mechanical impedance based parametric approach for damage diagnosis by means of changes in the structural mechanical impedance at high frequencies, modes from admittance signature. The main feature of the developed approach was that both the real as well as the imaginary component of the admittance signature were used in damage quantification. A complex damage metric was proposed to quantify damage parametrically based on the extracted structural parameters, i.e. the stiffness, the mass, and the damping associated with the drive point of the PZT patch. Their scheme eliminated the need for any a priori information about the phenomenological nature of the structure or any ‘model’ of the structural system.

In order to alleviate the shortcomings inherent in the Zhou’s model, a new concept of “effective impedance” was introduced by Bhalla and Soh (2004a, b). They defined the “effective impedance” considering force transfer distribution along the boundary of the PZT patch, as shown in Figure 2.7. The term “effective velocity” was introduced as an alternative to ‘drive point velocity’ used previously. Effective impedance is based on the premise that the

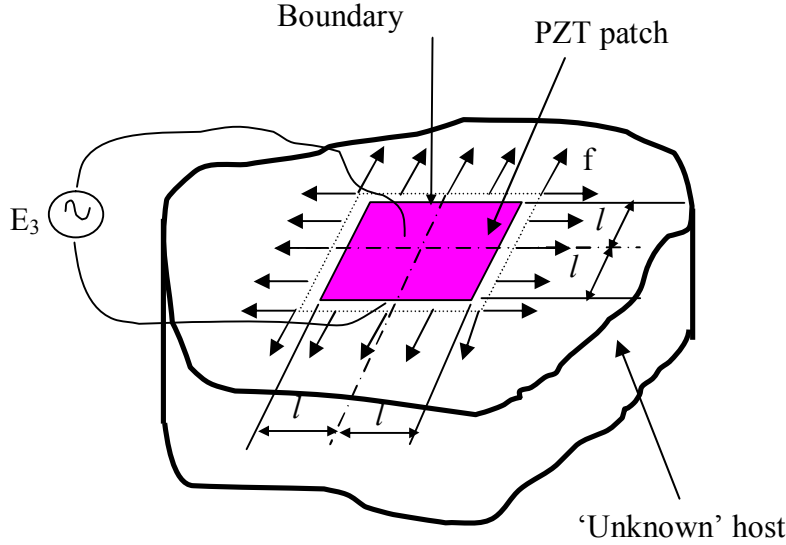


Figure 2.7 Effective impedance model (Bhalla and Soh, 2004a)

transmission of forces between the PZT patch and host structure occurs along the 2D peripheral boundary of the patch bonded to the structure. They mathematically expressed the effective impedance as

$$Z_{a,eff} = \frac{F_{eff}}{\dot{u}_{eff}} = \frac{\oint_s \vec{f} \cdot \hat{n} ds}{j\omega u_{eff}} \quad (2.25)$$

where \hat{n} is a unit vector normal to the boundary and ' F_{eff} ' represents the effective peripheral force due to PZT patch's deformation. $u_{eff} = \frac{\delta A}{P_0}$ is the effective displacement, with δA equal to the change in PZT patch's area and P_0 its perimeter in the undeformed condition. Consequently, effective velocity can be expressed as

$$\dot{u}_{eff} = j\omega u_{eff} \quad (2.26)$$

With this definition, following expression was derived by Bhalla and Soh (2004b) for $Z_{a,eff}$, the effective mechanical impedance of the PZT patch

$$Z_{a,eff} = \frac{2h\bar{Y}^E}{j\omega(1-\nu)\bar{T}} \quad (2.27)$$

where the term \bar{T} is given by

$$\bar{T} = \frac{1}{2} \left(\frac{\tan C_1 kl}{C_1 kl} + \frac{\tan C_2 kl}{C_2 kl} \right) \quad (2.28)$$

where C_1 and C_2 are the peak correction factors to be determined experimentally from signature of PZT patch in free-free condition. The mechanical impedance of structure ($Z_{s,eff}$) can be similarly defined, by applying a distributed effective force along the proposed boundary of the PZT patch. The final expression for the admittance for the 2D case derived by Bhalla and Soh (2004b) was

$$\bar{Y} = \frac{\bar{I}}{\bar{V}} = G + Bj = 4\omega j \frac{l^2}{h} \left[\bar{\epsilon}_{33}^T - \frac{2d_{31}^2 \bar{Y}^E}{(1-\nu)} + \frac{2d_{31}^2 \bar{Y}^E}{(1-\nu)} \left(\frac{Z_{a,eff}}{Z_{s,eff} + Z_{a,eff}} \right) \bar{T} \right] \quad (2.29)$$

Yang et al. (2005) developed a generic impedance model for predicting the EMI response for PZT-structure system for 1D and 2D cases. In this approach, the effect of piezo interaction with the host structure is represented by its force impedance at the boundary of the patch, which is obtained semi analytically. These force impedances are assumed to be the same at the opposite edges/ ends of the PZT patch. This assumption holds if the dimensions of the host structure are much larger than that of the PZT patch and the PZT patch is not close to the boundary.

Cheng and Lin (2005) formulated the coupling between the PZT patch and the host structure, using the impedance approach. A modified structural impedance model of the host structure was proposed to include the inertia effect caused by the PZT patch on the vibration response of the host structure, which proves to be important for a typical intelligent structure usually bonded with multiple PZT patches. A schematic representation of their model is shown in Figure. 2.8. In this model, modified mechanical impedance is expressed as

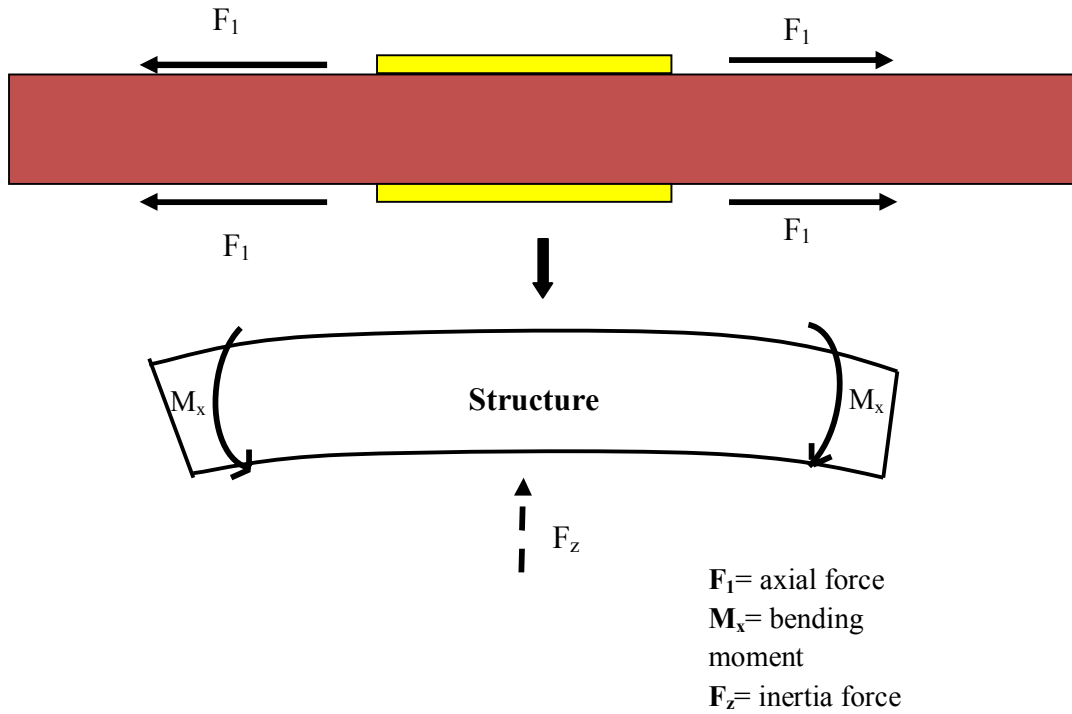


Figure 2.8 A schematic representation of actuating forces from PZT patch acting on the host structure (Cheng and Lim, 2005).

$$Z_p = \begin{bmatrix} Z_{pxx} & 0 \\ 0 & Z_{pyy} \end{bmatrix} \quad (2.30)$$

where

$$Z_{pxx} = \frac{F_1}{\dot{u}_1} = -j \frac{h\overline{Y^E}}{\omega} \frac{kw}{\tan(kh)} \quad (2.31)$$

$$Z_{pyy} = \frac{F_2}{\dot{u}_2} = -j \frac{h\overline{Y^E}}{\omega} \frac{kw}{\tan(kh)} \quad (2.32)$$

They concluded that the inertia effect caused by the PZT patch's mass on the vibration response is important and the results showed that the output force from each PZT patch was overestimated without including the mass of the PZT patch during the vibration synthesis. The added mass by the PZT patch on the host structure increases the electrical admittance and thus it requires a smaller output force from each PZT patch to produce a designated vibration response.

Annamdas and Soh (2007a, b) extended the 2D impedance modelling to three-dimensional (3D), especially suitable for a thick PZT patch, by proposing a directional sum impedance model, taking into account the PZT patch's vibrations along all the three directions. They defined the sum of direct impedance (Z_{si} , Z_{sj} , Z_{sk}) and cross impedance (Z_{ij} , Z_{jk} , Z_{ki}) equal to

$$Z_s = -(Z_{si} + Z_{sj}) + Z_{sk} - 2Z_{ij} + 2Z_{jk} + 2Z_{ki} \quad (2.33)$$

where Z_s denotes the direction sum impedance along three directions $i(\mathbf{x})$, $j(\mathbf{y})$ and $k(\mathbf{z})$, which can be individually expressed as

$$Z_{si} = \frac{F_i}{\dot{u}_i} \quad (2.34)$$

The cross impedances, which are produced by shear forces or stresses acting on the planes $ij(\mathbf{xy})$, $jk(\mathbf{yz})$, and $ki(\mathbf{zk})$, are given by

$$Z_{ij} = -\frac{Z_{si}Z_{sj}}{Z_{si} + Z_{sj} - Z_{sk}} \quad (2.35)$$

where F_i and \dot{u}_i are the transducer force on host structure and transducer velocity. For simplification, the shear stress equation was ignored and the constants of integration were proposed to be obtained through finite element analysis for this model, thereby necessitating modelling of the structure concerned. Unlike the effective impedance model of Bhalla and Soh (2004a) the directional sum impedance approach could not be independently used with experimental data alone for solving the inverse problem of extracting mechanical impedance from experimental signatures.

2.4 INCLUSION OF SHEAR LAG EFFECT IN IMPEDANCE BASED MODELS

The electromechanical behaviour of PZT sensor/actuator patches attached to the structure with bond layer is one of the most fundamental issues surrounding the effectiveness of a PZT patches in a smart structure system. An accurate assessment of the shear stress and strain distribution around the interfacial bond plays a dominant role in determining the actuation effect being transferred from the actuator to the host structure. The efficiency of the actuation depends on the ability of the adhesive layer to transfer stress and strain between the active and the passive constituents. As sensors, piezoelectric patches are usually bonded to structures to measure the strain by transforming mechanical deformation into electric voltage. The existence of bond layer introduces a strain lag effect, as a result of which the strain induced in the PZT sensor is less than that on the surface of the host structure.

It becomes, therefore, an important issue to study the coupled electromechanical behaviour of the PZT patch with bonding layers to reliably evaluate the relation between the measured signal and the local mechanical deformation. The bonding materials are usually much more complicated than the host structure, and in many practical applications, surface roughness entails relatively thick adhesive layers. Hence, understanding the effect of the properties of the adhesive layer on the performance of the entire system is crucial to the analysis, design and use of smart structures with bonded PZT patches, both as sensors and actuators. Due to the presence of material discontinuity between the patch and the host structure, complicated stress fields are generated when an external electric field is applied to the actuators.

Crawley and de Luis (1987) modelled the elastic bonding layer as a finite thickness between the PZT patch and structural beam, where patch was employed only as actuators. They assumed that the 1D PZT patch be actuated in pure bending with the strain linearly varying along the beam

thickness and the adhesive layer deforming in pure shear. This analysis showed that the outgoing strain on the PZT patch gets lowered due to bond layer's deformation. They quantified the effect in shear lag ratio “ ξ ” and expressed as

$$\xi = \left(\frac{S_p}{S_b} - 1 \right) \quad (2.36)$$

where S_p and S_b are the corresponding strains in PZT patch and the adhesive bond layer. In particular, the largest strain differences are predicted at the edge of the sensor, known as stress singularity. In addition, the analysis showed that, because of the shear lag effect, the sensor ‘appeared to the structure’ as if its dimensions were smaller than in actual. Crawley and Anderson (1990) further analyzed the previous strain transfer mode (Crawley and De Luis, 1987) based on Euler–Bernoulli beam theory. Sirohi and Chopra (2000a) derived an equation for ‘effective length’, l_{eff} , of the sensor, as

$$\frac{l_{eff}}{l} = 1 - \frac{\tanh(\Gamma l)}{(\Gamma l)} \quad (2.37)$$

$$\Gamma^2 = \left(\frac{G_s}{Y_p h h_s} + \frac{3G_s w_p}{Y_b h_b h w_b} \right) \quad (2.38)$$

where

and G_s is the shear modulus of the adhesive, Y_b the Young's modulus of elasticity of beam, h_s and h the thicknesses of the adhesive layer and PZT patch respectively and w_b the width of the beam. They concluded that for $\Gamma > 30 \text{ cm}^{-1}$, the shear lag effect can be assumed to be negligible and the force is transferred effectively over the end regions of the patch. The main limitation of effective length approach for EMI technique, however, is that it is not complete since in EMI technique, both sensor and actuator effects are utilized.

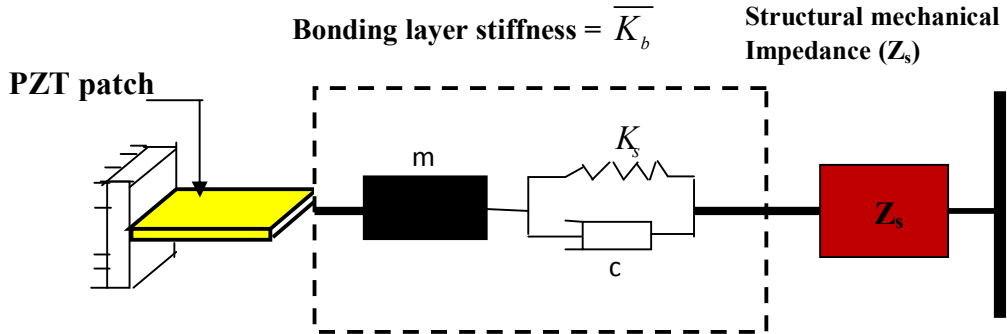


Figure 2.9 Modified impedance model of Xu and Liu (2002) including bond layer

Xu and Liu (2002) treated the bonding layer between the piezo element and the host structure as a spring-mass-damper system. The admittance of Liang's model was modified by incorporating the mechanical impedance (Z_b) of the bonding layer. The bond layer's impedance was placed 'in series' (see Figure. 2.9) with the structural impedance (Z_s) of the structure, so as to result in the equivalent impedance, can be expressed as

$$Z_{res} = \frac{Z_b Z_s}{(Z_b + Z_s)} = \xi Z_s \quad (2.39)$$

where ξ is the impedance modification factor

Ong et al. (2002) partially included the shear lag effect in the EMI technique by incorporating the effective length parameter suggested by Siorhi and Chopra (2000) for sensor case (ignoring the actuator effect).

A detailed derivation to integrate the shear lag effect into impedance formulation was proposed by Bhalla and Soh (2004c), with assumption of pure shear deformation of the adhesive layer. Bhalla's parametric study concluded that use of higher shear modulus of elasticity and small thickness of bond layer ensures better transformation of strain from the structure to the patch and

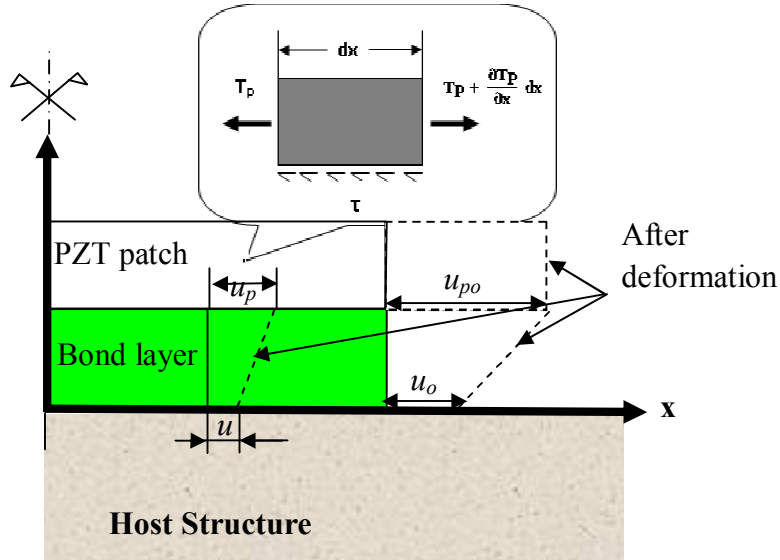


Figure 2.10 Force/strain transfer mechanism through adhesive bond (Bhalla and Soh, 2004)

vice versa. The governing dynamic shear lag equation (Bhalla and Soh, 2004c) for infinitesimal element shown in Figure 2.10, and can be formulated as

$$\tau wdx + (dm) \frac{\partial^2 u_p}{\partial t^2} = \frac{\partial T_p}{\partial x} h wdx \quad (2.40)$$

where u_p is the displacement in the PZT patch, dm the mass of the infinitesimal element, τ the interfacial shear stress and T_p the axial stress in the PZT patch. After neglecting the inertia term, the impedance modification factor (ξ), which was only ‘qualitatively’ described by Xu and Liu (2002), was rigorously derived by Bhalla and Soh (2004c) and for a square PZT patch as

$$\zeta = \frac{1}{1 + \left(\frac{1}{\bar{P}_{eff}} \frac{u'_0}{u_0} \right)} \quad (2.41)$$

where \bar{P}_{eff} is defined as

$$\bar{P}_{eff} = \frac{w \bar{G}_s}{Z_s h_s j \omega} \quad (2.42)$$

where u_o is the displacement at the surface of the host structure at the end point of the PZT patch as shown in Figure. 2.10, and u'_o is the corresponding strain. The main limitation of the model is that inertia term of Equation 2.40 is neglected.

Qing et al. (2006) experimentally studied the effect of both the thickness adhesive as well as the type of adhesive layer used to bond the patch to the host structure. It was found that the both the adhesive composition and the thickness could considerably affect the measured EMI signature, the observation closely matching those of Bhalla and Soh 2004c. Annamdas et al. (2007a, b) presented a numerical 3D FE model to obtain the EMI signature, for a rectangular PZT patch mounted on a structure, including the effects of the adhesive layer. The numerical results describing the structural responses were then used as inputs for theoretical 3D EMI model. Unfortunately, the researchers did not formulate a closed-form solution for the concerned effects.

Han et al. (2008) found that the dynamic behaviour of a piezoelectric sensor depends on the bonding condition along the interface between the sensor and the host structure. Both numerical and analytical comparative study was conducted to simulate 2D electro-mechanical behaviour of the integrated system. They concluded that the loading frequency should not be too high in order to ensure accuracy in sensor output. In addition, the material combination of the sensor and the host structure needs to be carefully selected in order to improve sensor efficiency.

Dugnani (2009) showed that for a circular PZT patch, the effect of the adhesive layer is frequency dependent and the losses due to shear deformation of the adhesive layer are predominant near the first radial resonance frequency. The model neglected the inertia terms of

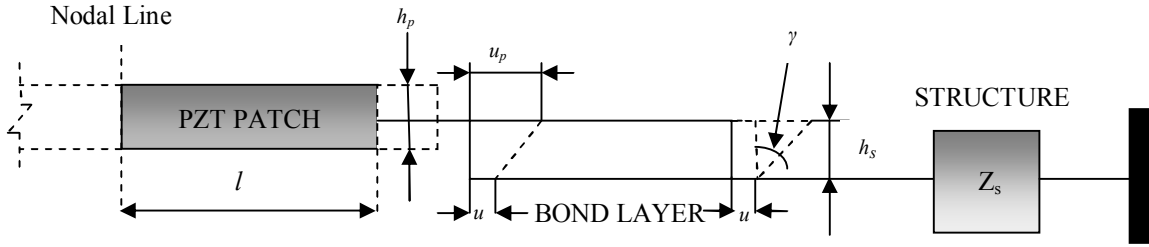


Figure 2.11 Simplified 1D impedance model (Bhalla et al., 2009)

the adhesive layer and assumed that the piezoelectric sensor was loaded by the host structure at the edge. Park et al. (2008) found that the effects of the bond layer are very significant in terms of both modifying the phase and amplitude of the produced electrical signals and also the measured EMI admittance spectrum. They observed that the imaginary part of the electrical admittance is more capable for detecting the deterioration of the bond layer.

Bhalla et al. (2009) presented a simplified impedance model to incorporate shear lag effect into electro-mechanical admittance formulation for both 1D and 2D cases. Their model (see Fig. 2.11) provides a closed-form analytical solution of the inverse problem, i.e. to derive the true structural impedance from the measured conductance and susceptance signature, thus an improvement over the previous models. The effective structural impedance as equivalent impedance $Z_{s,eq}$ was derived as

$$Z_{s,eq} = \frac{Z_s}{\left[1 - \left(\frac{Z_s \omega h_s j}{w l G_s} \right) \right]} \quad (2.43)$$

Huang et al. (2010) reviewed the development of analytical, numerical and hybrid approaches for modelling of the coupled piezo-elastodynamic behaviour including the bonding effect. They highlighted various issues like the effective use of PZT patch quantitatively and accurate

characterization of the local interfacial stress distribution between the patch and the host structure.

Tinoco et al. (2010) carried out a numerical study to understand adhesive layer's effects on the electro-mechanical coupling of the PZT patches bonded to structure. They identified that the deformations along the bonded interface present a nonlinear distribution of the strain and displacement. Electric potential generated across the PZT patch, when the structure is subjected to a known force, is modified when the thickness of the adhesive layer varies. The mechanical effects of the adhesive thickness are reflected on strains and electrical effects are reflected on electric potential generated by the PZT sensor. They also performed parametric study for stress and strain profile along the bond and found that the shear stresses are affected by the length of the sensor. Transmitted shear forces create a localized effect at the ends of the PZT sensor, where the shear stresses high. On the other hand, if the PZT sensors have small lengths, the mechanism to transmit forces is completely via shear stress throughout the interface.

2.5 NUMERICAL INVESTIGATION OF SHEAR LAG EFFECT OF FE PIEZO-STRUCTURE INTERACTION MODEL

The development of FE based piezoelectric models are primarily meant for vibration control of machinery and structural elements under static and dynamic loads. In early days, the major technical difficulty in conducting a successful FE simulation of the transducer was the lack of understanding of interaction between structural and electrical fields in the piezoelectric systems. The conventional numerical approach considered only structural degree of freedom, neglecting the electrical degree of freedom. The modern day coupled-field analysis on the other hand, takes into account the interaction between both the structural and the electrical fields. The new

piezoelectric finite element, available in several commercially available software, makes them very powerful tool in an integrated process of designing, prototyping and testing a transducer.

Various FE models on PZT-structure interaction have been proposed since the 1990s. Lalande et al. (1995) provided an excellent and insightful review into FE approaches for the simulation of PZT-structure interaction. They broadly classified the FE models into three categories, namely direct formulation of elements for specific application, utilization of a thermo elastic analogy, and the use of commercially available FE analysis (FEA) codes incorporated with piezoelectric element formulation. They attempted the dynamic FEA of ring and shell structures using the commercially available software ANSYS 5.0. Fairweather (1998) developed an FEA based impedance model for the prediction of structural response resulting from induced strain actuation. The model utilized FEA to determine the host structure's impedance based on eigen values and mass normalized eigen vectors. He derived the driving point mechanical impedance by evaluating the ratio of the applied known force to the resulting velocity, determined from the analysis.

For the application of the EMI technique, the mechanical impedance obtained could be used to determine the bonded PZT patch's admittance signature as if it were measured by an impedance analyzer, through the impedance based electromechanical coupling equation (Liang et al., 1994; Bhalla and Soh, 2004a). Initial applications of the above-mentioned models were mainly focused on a relatively low frequency of excitation, typically lower than 1 kHz. The FEA based impedance model was later applied to the EMI technique, which involves a much higher frequency of excitation, in the order of tens to hundreds of kHz. A study conducted by Makkonen et al., (2001) showed that fairly accurate results could be obtained for dynamic harmonic problems by FEA, even up to frequency of the order of GHz. With these

developments, the ability of FEA to model the behaviour of a PZT-structure interaction in the EMI technique has been significantly enhanced.

Bhalla (2001) simulated PZT-concrete interaction via 3D FE modelling. 1D impedance model was coupled to the 3D numerical model of the host structure, a concrete block. Damage was simulated using the built-in crack propagation scheme of ANSYS. Lim (2006) showed reasonably good agreement of between the experimental and the FEA based impedance results for an aluminium beam, truss and concrete cube. In fact, the above described models were semi-analytical, since they coupled the impedance based analytical model separately into the FE output consisting of displacement response.

Liu and Giurgiutiu (2006) investigated the use of FE model to simulate various SHM techniques with PZT patch. For the simulation of the EMI technique, simple models, like free piezo patches of different shapes and one-dimensional beam bonded with PZT patches were investigated. For the wave propagation technique, a long beam with several PZT patch installed was excited by tone burst signals with axial and flexural guided wave propagation along the beam. The existence of a crack will cause the echo to be reflected back. They highlighted the accuracy of the coupled field analysis with close agreement of simulated result to the experimental signature. Liu and Giurgiutiu (2007) compared the real part of the electrical impedance from both the FEA based impedance model (semi analytical) and the coupled field FE model for a 1D thin beam structure to experimental results. The coupled field FE model exhibited closer agreement to the experimental results.

Yang et al. (2008) simulated the PZT-structure interaction for the high frequency range (up to 1000 kHz) using the commercially available finite element (FE) software, ANSYS version 8.1, through the direct use of coupled field elements. Yang et al. (2011) derived the coupled field

governing equation for the strain on the patch and the surface of the host structure for both static and dynamic cases. They numerically simulated the strain ratio (piezo strain to that of structure) (S_p/S_b) and compared with the theoretical solution. They observed the strain at the ends of patch changes abruptly due to singularity, which cannot be simulated by FE multiphysic and also studied the effect of circuit resistance on the shear lag.

Jin and Wang (2011) predicted, through their numerical simulation, that the increase of the bond layer thickness will increase the shear stress distribution level along the internal of the actuator, and decrease the strain concentration at the tips of the actuator. Besides, the material combination of the actuator and the host structure needs to be carefully selected in order to improve actuator efficiency.

Zhang et al. (2011) derived a coupled EMI model of Timoshenko beam with a pair of PZT patches bonded on the top and bottom surfaces of the beam, with the bonding layer assumed as a Kelvin-Voigt model. The shear lag model was introduced to investigate the influence of the crack and the inertial forces of PZT patch and adhesive layers on the coupled structural response. They concluded with two significant results.

1. The inertial forces of the PZT patch and the bonding layer should be considered in the high frequency band, especially for a thin beam structure. Because the EMI technique employs high frequency, the inertial force should taken into account
2. In order to improve the accuracy of damage identification, the high frequency band which contains many peak frequencies should be chosen.

The coupled element based simulated result apparently have several advantages over the conventional uncoupled or semi-analytical approaches, such as direct acquisition of electrical

admittance/impedance and the ability to model various piezo active control system for different complexities.

2.6 SUMMARY: CRITICAL POINTS OF REVIEW

From the discussion in this chapter, it has been found that, the inclusion of the shear lag effect is still not complete. It needs to be properly addressed in coupled electro-mechanical impedance signature. Based on the critical review of literatures, the following points can be noted:

1. All the existing models do not consider the force/strain transfer phenomena completely, taking care of all the dynamic parameters involved in the piezo deformation process. They have included the shear lag parameters partially to avoid the complexity of the problem.
2. Crawely and de Luis (1987) added the bond layer in piezo-actuator beam but did not consider the inertial force in account due to negligible PZT mass. Also, their model is strictly based upon the quasi-static conditions, and especially suited to condition that the PZT patch serves as actuator only (dual effect ignored). Further, the results are not generic and restricted to beams only.
3. Siorhi and Chopra (2000) included the shear lag effect for sensor case by defining effective length factor.
4. Xu and Liu (2002) modelled the effect as single degree of freedom (SDOF) system by including bond stiffness (K_b). The model was however incomplete. No expression was derived for K_b , which highly depends upon bonding process and bond thickness and no experimental validation was attempted.
5. Ong et al. (2002) attempted characterization of shear lag effect for EMI technique using the analysis of Siorhi and Chopra (2000) through the concept of effective length. As they considered the patch as sensor only, the shear lag effect was included only partially.

6. Bhalla and Soh (2004c) carried out step-by-step derivation for shear lag effect considering by dynamic equilibrium equation (Equation (2.40)). But for the sake of simplicity, the inertia term (dm) and shear stress (τ) terms were solved separately and later superimposed. The solution was thus an approximation.
7. Bhalla et al. (2009) proposed simplified impedance model in which the bond layer was considered attached in series between the PZT patch and host structure, undergoing pure shear deformation. It was a simplified approach because the bond layer was not connected throughout the sensor length and attached as end-to-end connection.

2.7 GAPS IDENTIFIED IN PREVIOUS RESEARCH

The main gaps identified from the previous models developed for including the bond effect is the incorporation of inertia of the patch and the adhesive in the dynamic solution of the impedance based shear lag model. For the static case, the shear lag effect was quantified in static analysis in terms of shear lag ratio (Crawley and de Luis, 1987; Sirohi and Chopra, 2000a, b). From the dynamic interaction point of view, the bonding layer has been modelled as an added SDOF stiffness to the structure (Xu and Liu, 2002; Ong et al., 2002). For 2D case, Bhalla and Soh (2004) quantified the bonding effect on PZT-structure interaction through shear lag parameter $\overline{P_{eff}}$ and q_{eff} through effective impedance approach. But they solved the dynamic shear lag equilibrium equation (Eq. 2.40) by considering the inertia term (dm) and shear stress (τ) terms separately. In the earlier modelling, the bond layer was assumed to be attached at the ends of PZT patch and the host structure as a connector.

This research has aimed for the modelling the bonding effect more accurately and efficiently for impedance based SHM by solving inertia and shear term simultaneously and simulating the bond layer as continuum area between the patch and the structure.

2.8 RESEARCH OBJECTIVES

Keeping the above discussion in view, the following objectives have been addressed in this research work.

1. To perform preliminary investigation for the shear lag effect on piezo-impedance model numerically by performing FE coupled-field piezoelectric analysis.
2. To derive complete solution of the dynamic equilibrium equation (Eq. 2.40) for shear lag effect by considering the inertial parameter $(dm)\ddot{u}_p$ and shear stress τwdx simultaneously for were rigorous model.
3. To model the interfacial bond layer as a continuous medium of force transfer, between the PZT patch and the structure throughout sensor length, i.e. considering the stresses and the strains developed at interface due to PZT deformation continuously, and not just the end strains as in the previous models.
4. To investigate the effect of the bond layer on power consumption in piezo-driven systems using the new continuum based shear lag model.
5. To quantify the different losses occurring within piezo-active control system, by defining energy conversion efficiency ratio and to study their effect on the overall performance of the system.
6. To evolve a modified electro-mechanical coupling coefficient based on the continuum based piezo-mechanical system, duly considering all loss parameter and shear lag effect.

Chapter -3

SIMULATION OF SHEAR LAG EFFECT BY COUPLED FIELD FINITE ELEMENT MODELLING

3.1 INTRODUCTION

The current trend of engineering activities for the development and industrial applications of piezoelectric transducers has prompted the development and simulation and design tools to aid designing applications such as oscillators for electronic circuits, acceleration sensors and gyroscopes, sound transducers, vibration monitoring, vibration control and energy harvesting. Except for very few applications where the structure's geometry including the piezoelectric elements is simple and can be solved through analytical solution, otherwise numerical methods, such as the finite element method (FEM), have to be used to simulate complex electro-mechanical systems.

For decades, the FEM has been extensively applied for stress analysis of structures. The advantage of FEM over analytical solutions is that stress and electrical field measurements for systems of complex geometries, and their variations throughout the device, can be easily determined by FEM. It eliminates the need to manufacture and test numerous specimens. The major earlier technical difficulty in conducting a successful simulation on piezo transducers was the lack of appropriate tools for modelling the interaction between the patch and the host structure, which involves complicated coupling of mechanical and electrical domains. It is not enough to understand these areas individually. However, by capturing the coupled effects of these phenomena simultaneously, a step could be made forward for an efficient and optimized piezo-active model for practical applications. This can be possible by using coupled-field analysis through FEM, which can take care of the interactions between the mechanical and electrical domains concurrently.

This chapter focuses on numerical modelling of piezo-structure interaction through bond layer for both 2D and 3D using ANSYS 12.0 (2010). For electro-mechanical coupled simulations, there are several ingredients, the major being the format of input of the key parameters. Hence, this chapter has aimed to model piezo shear lag model with modified input of material properties in the recommended format, resulting in accurate piezoelectric analysis for the EMI technique.

3.2 FE MODELLING INVOLVING PZT TRANSDUCERS

In particular, the actuators action on a structure appears as an external force proportional to the applied voltage, whereas the system's stiffness is purely elastic. In case of sensors, the problem appears as an added stiffness term due to the open-circuit condition of the piezoelectric patch, whose terminal voltage (the sensor output) is proportional to the mechanical displacement. If the piezoelectric elements are used either as sensors or actuators for sensing or active vibration control, it is worth remarking that the electrical unknowns can be condensed or coupled so that the problem has the form of a standard elastic vibration problem.

A pioneering work on piezoelectric finite element by Allik and Hughes (1970) proposed the formulation of coupling between the mechanical displacement and the electric potential field, taking into account both direct and inverse effects. This formulation formed on the basis of numerical studies involving an elastic structure with coupled piezoelectric elements (Tzou and Tseng, 1990; Hwang and Park, 1993; Vasques and Rodrigues, 2005; Kim et al., 1997; Saravanos et al., 1997; Trindade et al., 2001; Lammering et al., 2003; Carrera and Boscolo, 2007). However, the need of modelling for both sensing and actuation at the same time is required by applications where a passive electric circuit is connected to the piezoelectric elements. Shunt techniques were proposed by Hagood and flowtow (1991) and reviewed by

Lesieurte (1998). The initial models used for simulating these shunted systems were lumped, with only two degrees of freedom (DOF) (one mechanical and one electrical, in most cases one vibration mode and the electric-free charge). On the contrary, richer models can be obtained through present day piezoelectric FEM commercial software, by simulating the shunt as an active controller with simultaneous sensing and actuation (Nguyen et al., 2006). This later case is often numerically intensive. In addition to simulating the vibratory behaviour of the mechanical structure coupled to an electric circuit, another achievement is the optimization of the whole system, in terms of size/shape/location of the piezoelectric patches as well as the choice of the electric circuit components. The coupled element based simulated results have several advantages over the conventional uncoupled or semi-analytical approaches, such as direct output of electrical admittance/impedance and the ability to model the PZT patch and the bonding layer simultaneously. Therefore, the next section will follow complete modelling of the PZT-structure interaction including the bonding layer using commercially available FE software, ANSYS 12.0 through inbuilt coupled field element. Performing the harmonic analysis, the outcomes will be compared to impedance based semi analytical solution (Bhalla et al., 2004a) as well as the experimental signatures (Bhalla et al., 2004b).

3.3 REVIEW OF FE MODELLING USING COUPLED-FIELD ANALYSIS

In certain engineering problems, the behaviour of some system requires additional conditions or degree of freedom. For example, certain points (nodes) may be expected to have the same displacement in a certain direction. One can take advantage of this behaviour and enforce it in order to achieve an accurate solution with minimum computational resources. If particular degrees of freedom at several nodes are expected to have the same unknown value, these degrees of freedoms can be coupled. Piezoelectric analysis comes under the category of coupled field analysis. Coupled field analysis considers the interaction or coupling between

two or more disciplines of engineering (ANSYS, 2012). Piezoelectric analysis caters for the interaction between structural and electric fields for static, modal, harmonic and transient analyses. Basically, two types coupling methods are used for FE modelling. Strong or simultaneous coupling is mainly used for piezoelectric analysis. Week or sequential coupling is mostly used for high temperature acoustic applications.

Various FE coupled elements, in different forms such as solid, shells and plates have been developed to model piezoelectric adaptive structures. Coupled field elements, incorporating both mechanical and electrical degrees of freedoms, reflect the electro-mechanical coupling character of piezoelectric materials to study the interactions of piezoelectric active sensors with host structures. The present coupled FE study uses 3-D brick elements having eight nodes with up to six DOF at each node. When used for piezoelectric analysis, it adds an extra electrical voltage DOF in addition to six displacement DOFs. For each DOF of a node, there is a reaction force. Reaction force F_X , F_Y , F_Z corresponds to the X , Y , Z displacements respectively and charge Q corresponds to the voltage DOF, which is utilized to calculate the admittance.

3.4 THEORY OF COUPLED PIEZOELECTRIC ANALYSIS

The piezoelectric material parameter format suggested in the IEEE standard 176 (1987) is drastically different from the ANSYS format. The IEEE Standard specifies standard 1x6 format for stress matrix as $\{\sigma_x, \sigma_y, \sigma_z, \sigma_{yz}, \sigma_{xz}, \sigma_{xy}\}$. ANSYS, on the other hand, uses the standard structural mechanics format where the order is $\{\sigma_x, \sigma_y, \sigma_z, \sigma_{xy}, \sigma_{yz}, \sigma_{xz}\}$. Material data which is considered in the IEEE format having the polarization axis along Z-direction, where as in ANSYS format, the Y axis is considered for polarization (see Figure 3.1(a) and (b)). Thus, the supplied material data must be transformed appropriately. Some of the term

conversions are discussed here. Anisotropic elastic compliance matrix in IEEE standard format (polarization axis Z-axis) is

$$\begin{bmatrix} S_{11} & S_{12} & S_{13} & 0 & 0 & 0 \\ S_{21} & S_{22} & S_{23} & 0 & 0 & 0 \\ S_{31} & S_{32} & S_{33} & 0 & 0 & 0 \\ 0 & 0 & 0 & S_{44} & 0 & 0 \\ 0 & 0 & 0 & 0 & S_{55} & 0 \\ 0 & 0 & 0 & 0 & 0 & S_{66} \end{bmatrix} \quad (3.1)$$

As per ANSYS format, this should be transformed as

$$\begin{bmatrix} S_{11} & S_{12} & S_{13} & 0 & 0 & 0 \\ S_{21} & S_{22} & S_{23} & 0 & 0 & 0 \\ S_{31} & S_{32} & S_{33} & 0 & 0 & 0 \\ 0 & 0 & 0 & S_{66} & 0 & 0 \\ 0 & 0 & 0 & 0 & S_{44} & 0 \\ 0 & 0 & 0 & 0 & 0 & S_{55} \end{bmatrix} \quad (3.2)$$

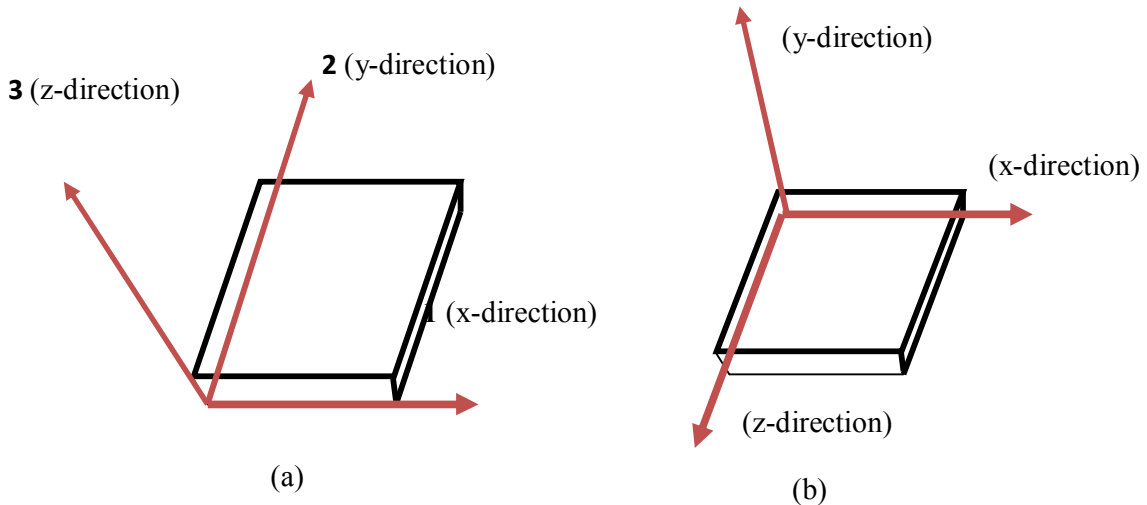


Figure 3.1 A piezoelectric material sheet with

- a) Axes as per IEEE standard
- b) Axes as per ANSYS format

Further, in addition to converting the elasticity data from the IEEE format to the ANSYS format, it must be also rotated so that the polarization direction will be Y rather than Z, that is, Z and Y terms need to be interchanged, so that the matrix is

$$\begin{bmatrix} S_{11} & S_{13} & S_{12} & 0 & 0 & 0 \\ S_{31} & S_{33} & S_{32} & 0 & 0 & 0 \\ S_{21} & S_{23} & S_{22} & 0 & 0 & 0 \\ 0 & 0 & 0 & S_{66} & 0 & 0 \\ 0 & 0 & 0 & 0 & S_{55} & 0 \\ 0 & 0 & 0 & 0 & 0 & S_{44} \end{bmatrix} \quad (3.3)$$

The piezoelectric strain co-efficient matrix in IEEE standard input is

$$\begin{pmatrix} 0 & 0 & d_{31} \\ 0 & 0 & d_{32} \\ 0 & 0 & d_{33} \\ 0 & d_{42} & 0 \\ d_{15} & 0 & 0 \\ 0 & 0 & 0 \end{pmatrix} \quad (3.4)$$

Rearranging the rows of 4, 5 and 6, the matrix in the ANSYS format will be

$$\begin{pmatrix} 0 & 0 & d_{31} \\ 0 & 0 & d_{32} \\ 0 & 0 & d_{33} \\ 0 & 0 & 0 \\ 0 & d_{42} & 0 \\ d_{15} & 0 & 0 \end{pmatrix} \quad (3.5)$$

Finally, Y being the axis of polarization instead of Z, must be accounted for; hence the transformation can be presented as

$$\begin{array}{c} \begin{array}{ccc} x & y & z \\ d_{11} & d_{21} & d_{31} \\ d_{21} & d_{22} & d_{23} \\ d_{31} & d_{32} & d_{33} \\ d_{41} & d_{42} & d_{43} \\ d_{51} & d_{52} & d_{53} \\ d_{61} & d_{62} & d_{63} \end{array} & \xrightarrow{\hspace{10em}} & \begin{array}{ccc} x & z & y \\ d_{11} & d_{31} & d_{21} \\ D_{31} & D_{33} & D_{32} \\ D_{21} & D_{23} & D_{22} \\ d_{61} & d_{63} & d_{62} \\ d_{51} & d_{53} & d_{52} \\ d_{41} & d_{42} & d_{43} \end{array} \end{array}$$

Hence, the final piezoelectric strain co-efficient matrix in the ANSYS format shall be

$$\begin{pmatrix} 0 & d_{31} & 0 \\ 0 & d_{33} & 0 \\ 0 & d_{32} & 0 \\ 0 & 0 & 0 \\ 0 & 0 & d_{42} \\ d_{51} & 0 & 0 \end{pmatrix} \quad (3.6)$$

In the same manner, the dielectric permittivity matrix at constant stress can be expressed in the ANSYS format (for Y-axis as the polarization axis) as

$$\begin{bmatrix} \varepsilon_{22} & 0 & 0 \\ 0 & \varepsilon_{11} & 0 \\ 0 & 0 & \varepsilon_{33} \end{bmatrix} \quad (3.7)$$

The finite element discretization is performed by establishing nodal solution variables and element shape functions over an element domain, which approximates the solution, that is

$$\{u_c\} = [N^u]^T \{u\} \quad (3.8)$$

$$\{V_c\} = [N^V]^T \{V\} \quad (3.9)$$

where $\{u_c\}$ represents the structural displacements within the element domain in the x , y , and z directions, and V_c is the electrical potential for the same coupled FE element. $[N_u]$ and $[N^V]$ are the shape functions for structural displacement and electrical potential of the considered element respectively. $\{u\}$ and $\{V\}$ are the vectors of the nodal displacements and the nodal electrical potential respectively.

Expanding the terms,

$$[N^u]^T = \begin{bmatrix} N_1 & 0 & 0 & \dots & N_n & 0 & 0 \\ 0 & N_1 & 0 & \dots & 0 & N_n & 0 \\ 0 & 0 & N_1 & \dots & 0 & 0 & N_n \end{bmatrix} \quad (3.10)$$

and

$$[N^V]^T = (N_1 \ N_2 \ \dots \ N_n) \quad (3.11)$$

The structural displacement $\{u\}$ and electric nodal displacements $\{V\}$ can be represented as

$$\{u\} = \begin{Bmatrix} u_{x1} & u_{y1} & u_{z1} \\ u_{x2} & u_{y2} & u_{z2} \\ u_{x3} & u_{y3} & u_{z3} \\ \dots & \dots & \dots \\ \dots & \dots & \dots \\ u_{xn} & u_{yn} & u_{zn} \end{Bmatrix} \quad \text{and} \quad \{V\} = \begin{Bmatrix} V_1 \\ V_2 \\ \vdots \\ V_n \end{Bmatrix} \quad (3.12)$$

The constitutive matrices $[B_u]$ and $[B_V]$ respectively for the structural and electrical DOF are related to the structural and electrical displacement as follows

$$\{S\} = [B_u]\{u\} \quad (3.13)$$

$$\{E\} = -[B_V]\{V\} \quad (3.14)$$

where $\{B_u\}$ and $\{B_V\}$ respectively expressed as

$$\{B_u\} = \begin{bmatrix} \frac{\partial}{\partial x} & 0 & 0 \\ 0 & \frac{\partial}{\partial y} & 0 \\ 0 & 0 & \frac{\partial}{\partial z} \\ \frac{\partial}{\partial y} & \frac{\partial}{\partial x} & 0 \\ 0 & \frac{\partial}{\partial z} & \frac{\partial}{\partial y} \\ \frac{\partial}{\partial z} & 0 & \frac{\partial}{\partial x} \end{bmatrix} [N^u]^T \quad (3.15)$$

and

$$[B_V] = \begin{bmatrix} \frac{\partial y}{\partial x} \\ \frac{\partial y}{\partial y} \\ \frac{\partial y}{\partial z} \end{bmatrix} \{N^V\}^T \quad (3.16)$$

Using variation principle, the coupled FE matrix for piezoelectric analysis can be expressed as (ANSYS, 2010; Allik, 1970).

$$\begin{bmatrix} [M] & [0] \\ [0] & [0] \end{bmatrix} \begin{Bmatrix} \{\ddot{u}\} \\ \{\ddot{V}\} \end{Bmatrix} + \begin{bmatrix} [c] & [0] \\ [0] & [0] \end{bmatrix} \begin{Bmatrix} \{\dot{u}\} \\ \{\dot{V}\} \end{Bmatrix} + \begin{bmatrix} [K] & [K^Z] \\ [K^Z]^T & [K^d] \end{bmatrix} \begin{Bmatrix} \{u\} \\ \{V\} \end{Bmatrix} = \begin{Bmatrix} \{F\} \\ \{L\} \end{Bmatrix} \quad (3.17)$$

where $\{u\}$ is the structural displacement vector, $\{V\}$ the vector of nodal electric potential (the dot above a variables denotes time derivative), $\{L\}$ the vector of nodal, surface and body charges.

The piezoelectric coupling matrix $[K^Z]$ and $[K^V]$, the dielectric conductivity, can be defined as

$$[K^Z] = \int_{vol} [B_u]^T [\varepsilon] [B_V] d(vol) \quad (3.17.1)$$

$$[K^d] = \int_{vol} [B_V]^T [\varepsilon] [B_V] d(vol) \quad (3.17.2)$$

The Raleigh damping matrix $[C]$ has been considered structural damping can be expressed as

$$[C] = \alpha [M] + \beta [K] \quad (3.17.3)$$

where $\alpha = 0$ and $\beta = \frac{\eta}{\omega}$. $[M]$ denotes the structural mass matrix and $\{F\}$ presents the structural force developed due to coupled piezo deformation. For the FE modelling, plane 13 and solid 5 elements were chosen for 2D and 3D PZT patch's modelling respectively. The excitation of the PZT patch in this study is well within the linear range, as in the EMI technique, due to the use of very small voltage (typically 1V). Effect of hysteresis is also assumed to be negligible due to the use of relatively thin and small patch with very low voltage of excitation. For piezoelectric analysis, one needs to couple the bottom and top nodes of the PZT patch with "VOLT" DOF. Performing the full harmonic analysis, the resultant output can be obtained as reaction force (-Q) labelled as AMPS from time history post processor of ANSYS 12.0. (Lim, 2010). For obtaining current, one has to consider the negative of the charge (Lim, 2010) and differentiate charge with respect to time that is

$$\begin{aligned} -Q &= -(Q_r + Q_j j) e^{j\omega t} \\ I &= \frac{d(-Q)}{dt} = (-I_r - I_j j) e^{j\omega t} \end{aligned} \quad (3.18)$$

Finally, the electro-mechanical admittance can be obtained by

$$\bar{Y} = \frac{\bar{I}}{\bar{V}} \quad (3.19)$$

With the aid of ANSYS 12.0, the electric current can be directly computed for the admittance signature from the EMI technique (with $\bar{V} = 1V$), saving all the hassle of converting the mechanical impedance into electrical admittance through the impedance based electromechanical coupling equation (Equation 2.13) as, required in the FEA based semi-analytical impedance models. The mechanical and electrical properties of PZT patch have been enlisted in Table 3.1.

Table 3.1: Piezoelectric properties of PIC 151 (PI Ceramics, 2010).

Parameters	Symbols	Values	Unit
Density	ρ	7800	Kg/m ³
Dielectric loss factor	$\tan\delta$	0.02	$10^{-12} \text{ m}^2/\text{N}$
	S_{11}	15.0	
	$S_{22}=S_{33}$	19.0	
	$S_{12}=S_{21}$	-4.50	
	$S_{13}=S_{31}$	-5.70	
	$S_{23}=S_{32}$	-5.70	
	$S_{44}=S_{55}$	39.0	
Compliance	S_{66}	49.4	$10^{-12} \text{ m}^2/\text{N}$
	ε_{11}^T	1.75	
	ε_{22}^T	1.75	
Electric Permittivity	ε_{33}^T	2.12	10^{-8} F/m
	d_{31}	-2.10	
	d_{32}	-2.10	
	d_{33}	5.0	
	d_{24}	5.80	
Piezoelectric Strain Coefficients	d_{15}	5.80	10^{-10} m/V

3.5 2D FE MODELLING OF ADHESIVELY BONDED PZT PATCH

Figure 3.2 presents the a 2D FE model, where a host structure (48x10mm) is instrumented with a PZT patch (5mm x 0.3mm) with the help of epoxy adhesive of thickness 0.03mm.Though the structure is 2D, the PZT-structure interaction is 1D in nature (i.e. the displacement of PZT patch and structure is coupled along x-axis only). The material properties of the structure listed in Table-3.2 and those of PZT patch listed in Table 3.1 were used for modelling in the ANSYS 12.0 workspace. Due to geometric symmetry, only one half of the piezo structural system (24x10mm) has been modelled. The convergence study was done, resulting in a suitable element mesh size of 0.5mm. The comparison between the outputs of PZT-structure interaction system with and without adhesive (perfect bonding condition) is shown in Figure 3.3. For this case, the conversion of material input for polarization axis is required, because for 2D shear lag model, the normalized Y- axis is being considered for polarization axis. Along the line of symmetry thr x component of displacement is locked, other boundary conditions are self explanatory.

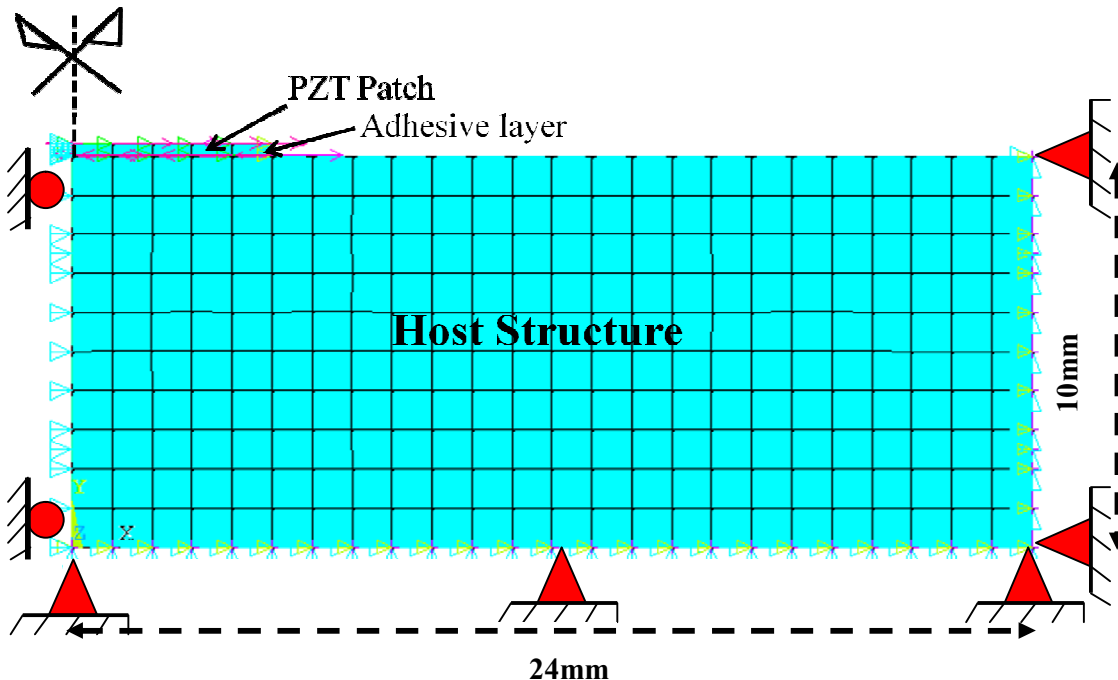


Figure 3.2 FE model of 2D PZT- Structure interaction

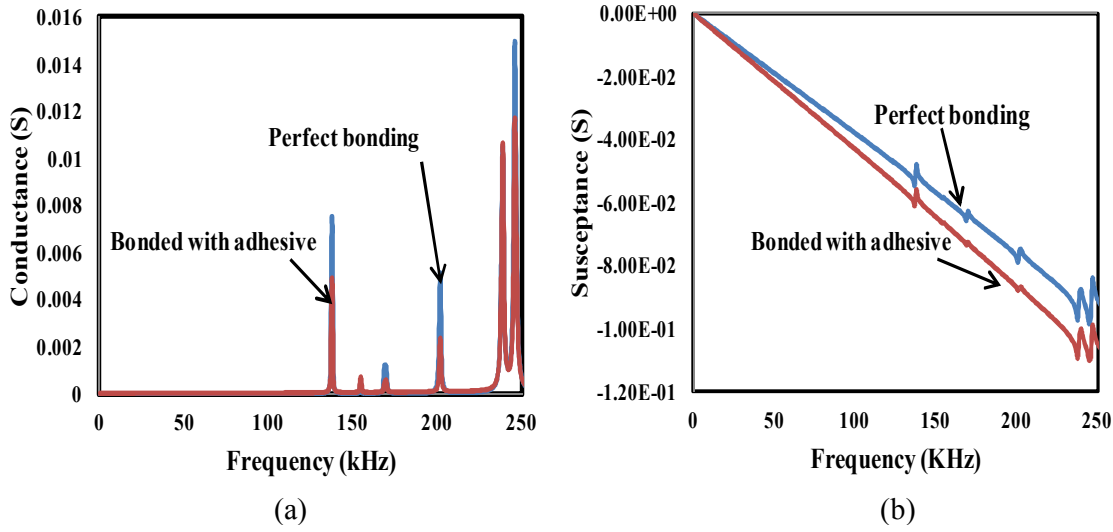


Figure 3.3 Effect of adhesive on PZT-Structure interaction signature

- (a) Conductance (G) vs Frequency
- (b) Susceptance (B) vs Frequency

It can be clearly observed from figure that the presence of the bond layer has significantly influenced on the admittance signature in terms of shifting of peaks downwards in the conductance (G) plot and change in the slope of the susceptance (B) plot. It is also observed that the imaginary part (B) of the numerically simulated admittance signature is negative contrary to actual observation. The susceptance plot reported by Yang et al. (2008) performing similar analysis was possibly incorrect because material properties were not in proper ANSYS format. The shifting of resonance peak in conductance plot implies inaccurate detection of structural resonance frequencies in presence of bonding. Similarly the bond deterioration can be interpret form the shifting of slope in susceptance curve.

The result from the present numerical analysis is compared with the 1D impedance based analytical signature contributed by Liang et al. (1994) (no bond layer), Bhalla and Soh (2004c) (with bond layer) and Bhalla et al. (2009) (with bond layer) in Figure 3.4. For the sake comparison, the absolute value of susceptance is considered. Further, in order to investigate the characteristics of basic piezo-ceramic properties and their effects on the signature, a parametric study has been carried out.

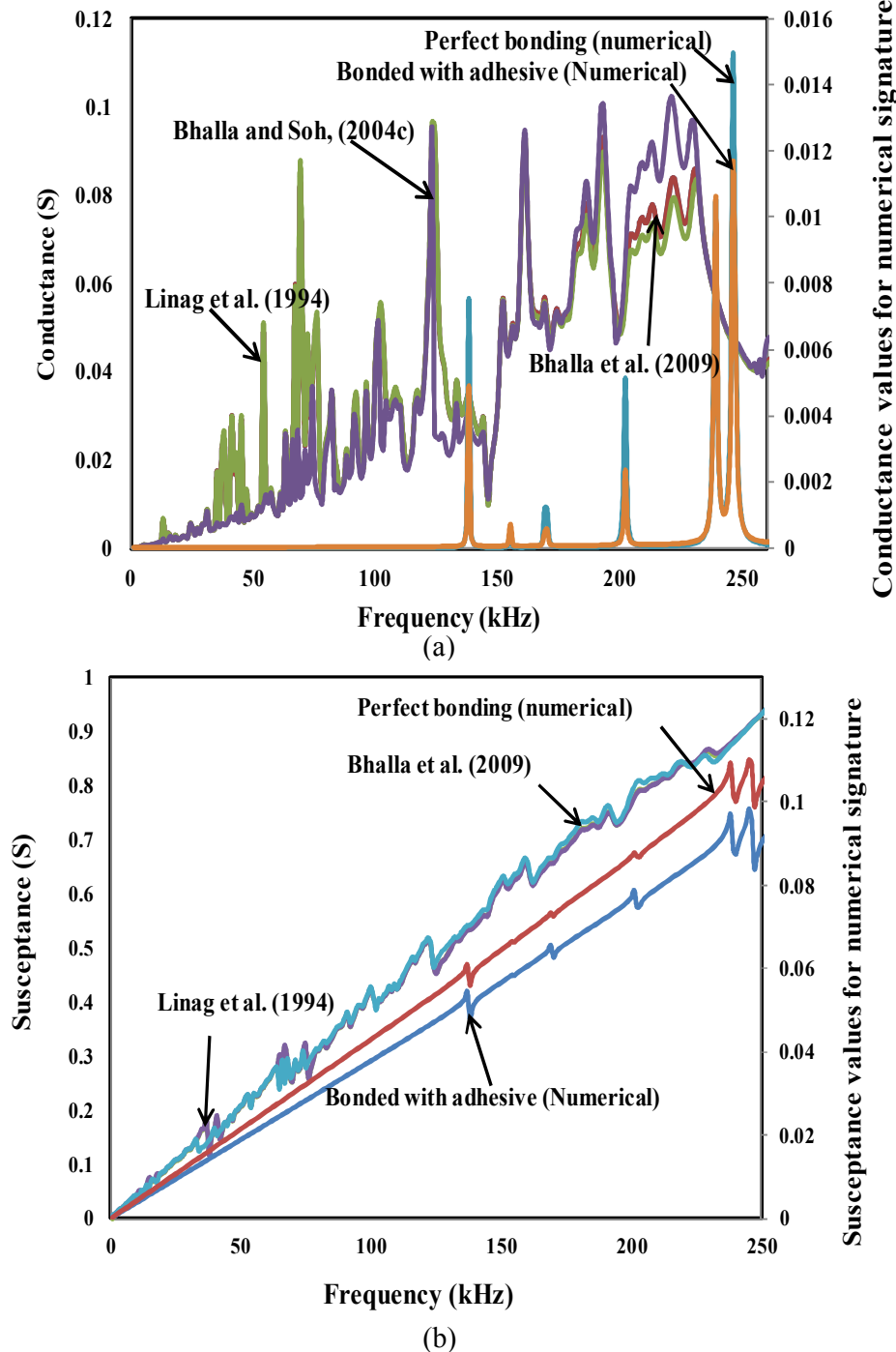


Figure 3.4 Comparison of coupled field numerical result with other analytical results

- (a) Conductance (G) vs Frequency
- (b) Susceptance (B) vs Frequency

Figure 3.5 shows the variation of admittance signature with alteration of the bond thickness.

It is observed that by altering the bond thickness to lower values, the peaks of admittance plot have reduced significantly. Similarly, the effect of other parameters like shear modulus and damping of the bond layer is depicted in Figures 3.6 and 3.7 respectively. It is very apparent from Figure 3.7, that the mechanical loss factor has very negligible effect on admittance signature compared to shear modulus, which alters the signature drastically.

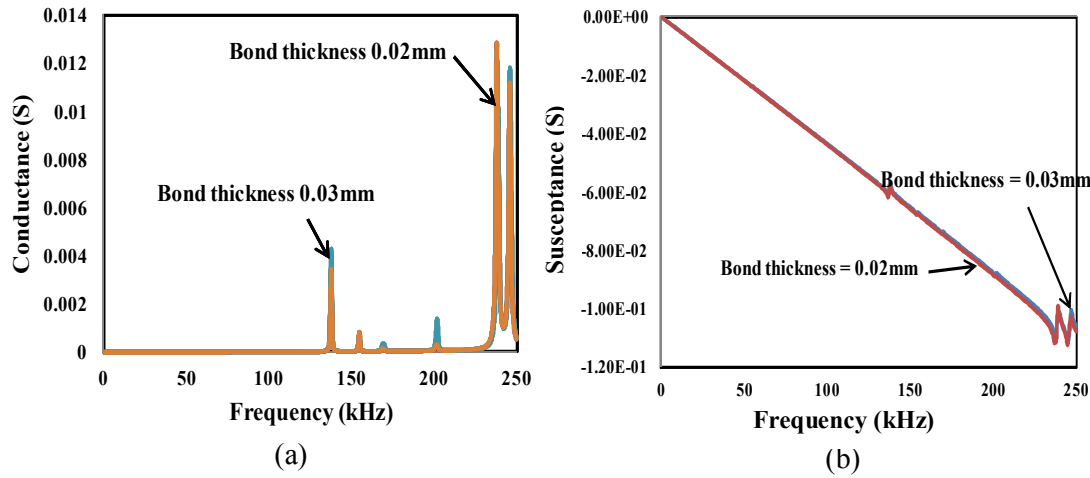


Figure 3.5 Effect of bond thickness on electro-mechanical admittance signature

- (a) Conductance (G) vs Frequency
- (b) Susecptance (B) vs Frequency

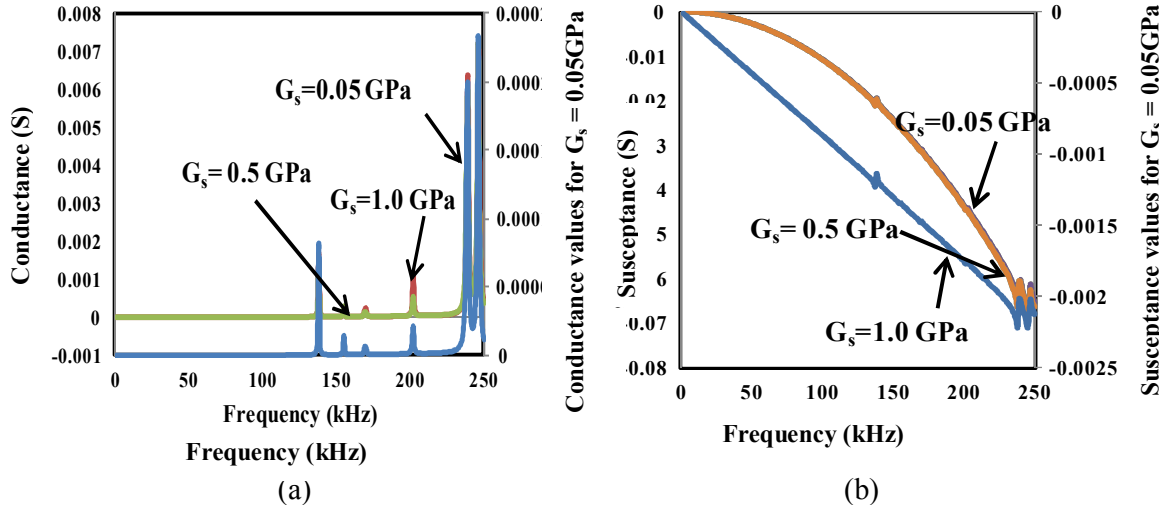


Figure 3.6 Effect of shear modulus of bond layer on electro-mechanical admittance signature

- (a) Conductance (G) vs Frequency
- (b) Susceptance (B) vs Frequency

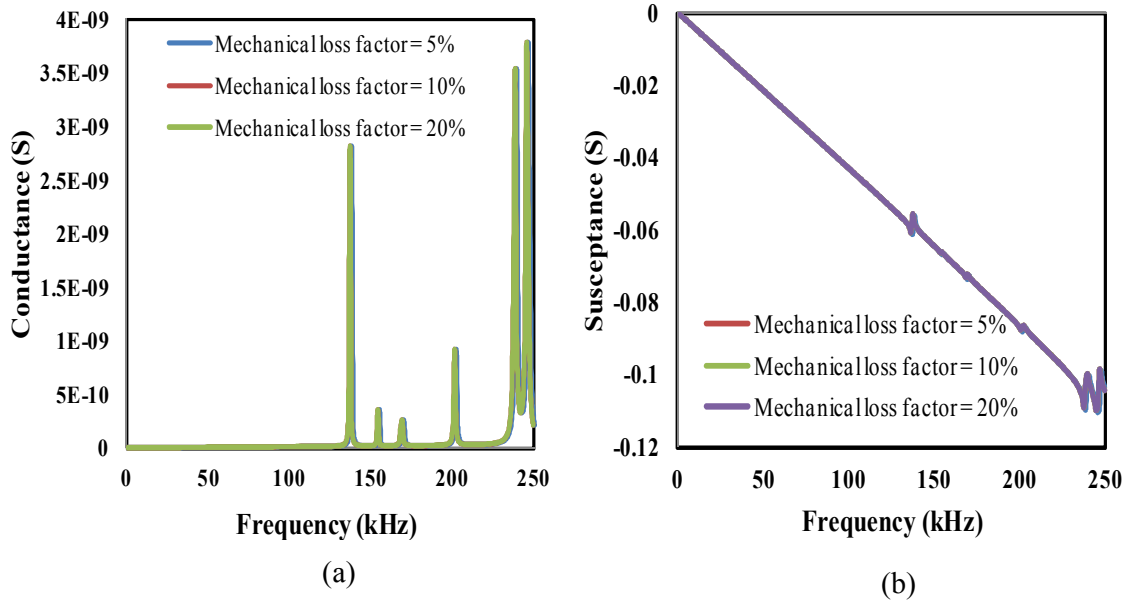


Figure 3.8 Effect of mechanical loss factor on electro- mechanical admittance signature

- (a) Conductance (G) vs Frequency
- (b) Susceptance (B) vs Frequency

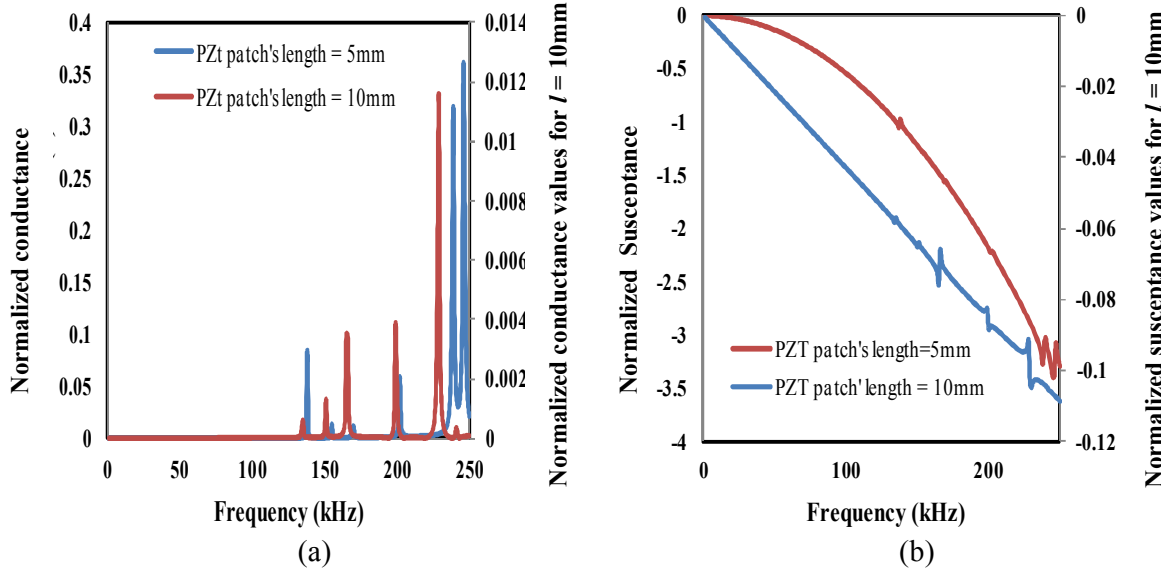


Figure 3.8 Effect of sensor length on electro- mechanical admittance signature

- (c) Conductance (G) vs Frequency
- (d) Susceptance (B) vs Frequency

Figure 3.8 shows the effect of sensor length on the admittance spectrum. In real part (conductance), the resonance peaks are shifted towards the left with higher peak value as the sensor length increase. On the other hand, in the imaginary part (susceptance) the peaks of the curve have changed abruptly. Hence, it can be stated that the change in sensor length affects the mechanics of the PZT-structure interaction has changed.

3.6 3D MODELLING OF ADHESIVELY BONDED PZT PATCH

The previous sections have demonstrated the feasibility of FEM for the modelling of 2D PZT-structure interaction. In this section, the FE modelling has been extended to the simulation of PZT-structure interaction for 3D case, including the interfacial adhesive layer. From the point of view the PZT patch, the interaction is 2D in nature. The PZT patch has been modelled with the Solid 5 element. This is due to the fact that the Solid 5 element possesses lesser nodes, which is more convenient in modelling multiple structures interactions. Also, according to recommendation by ANSYS 12.0 (2010), a smaller size element with lesser nodes is preferred rather than a larger size element with more nodes. The material properties of the aluminium beam and adhesive listed in Table 3.2 were considered. The type of element used for both bonding layer and aluminium block is Solid 45, specified for modelling of solid structures with eight nodes having three degree of freedom at each node.

Solid 5 elements is eight noded 3D coupled field brick element having six degrees of freedom (u_x , u_y , u_z , VOLT, TEMP and MAG DOF), For piezoelectric analysis, we need only four degree of freedom (u_x , u_y , u_z , VOLT). Solid 5 has 3-D magnetic, thermal, electric, piezoelectric and structural field capability with limited coupling between the fields. The element has special advantages over other elements i.e. iterative solution for field coupling, large deflection and stress stiffening.

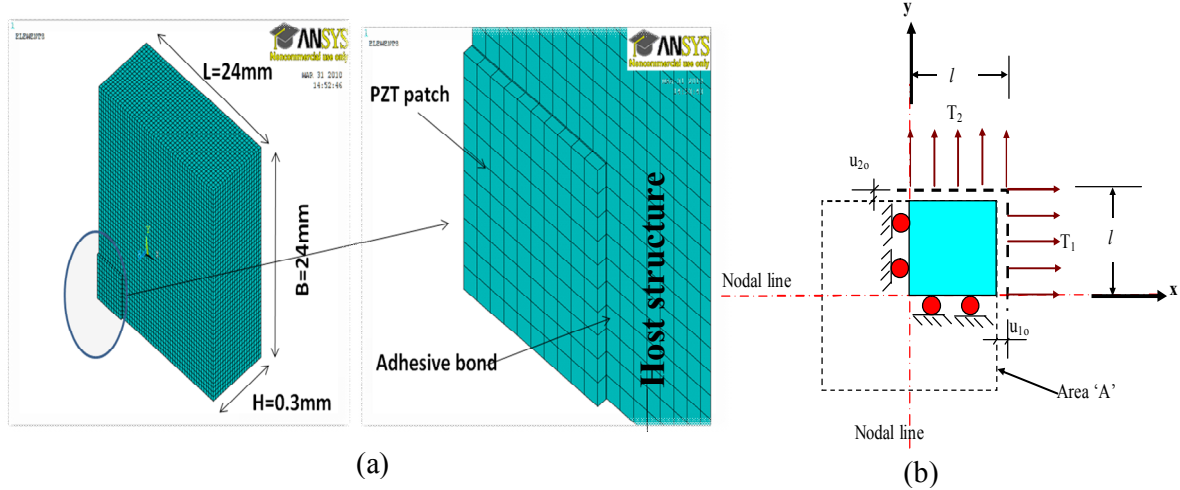


Figure 3.9 (a) Isometric view of one-fourth of aluminium block (48mm x 48mm x 10mm) adhesively bonded with PZT-patch modelled in ANSYS12.0 workspace. (b) Illustration of geometric and loading symmetry of the model.

A simple rectangular aluminium block sized 48mm x 48mm x 10mm was considered as the host structure in this study. A PZT patch of size 10mm x 10mm x 0.3mm was assumed to be bonded at the centre of the block (see Figure 3.9). Again, taking advantage of the geometrical and loading symmetry, only one-fourth of the system was modelled.

It is worth mentioning that the patch was simulated to be ‘bonded’ to the aluminium beam through the bonding layer by merging the interfacial nodes between the patch and the bond layer. Merging of the nodes ensures that the interfacial nodes carry the same displacements and thus ensuring strain transfer. Both planes (top and bottom plane) of the PZT patch lies in xy plane (i.e. poling axis is Z-direction). Hence, the polarization axis (Z-axis) is the same as in IEEE format for this coupled field analysis. Therefore, for this case, the input material properties were not converted for polarization axis which was needed for 2D shear lag model. Equations (3.2), (3.5) and (3.7) are quite sufficient for this piezo harmonic analysis. Element sized 0.5mm was adopted throughout the entire modelling. The Table 3.3 present mesh convergence test result for perfectly bonded PZT patch, which shows that an element size of 0.5mm is sufficient to ensure satisfactory results.

Table- 3.2: Material properties of Aluminium block and adhesive

Parameter	Symbols	Material	values	Unit
Density	ρ	Aluminium Epoxy	2715 1000	Kg/m^3
Poisson's ration	ν	Aluminium Epoxy	0.3 0.4	
Young's Modulus	\overline{Y}^E	Aluminium Epoxy	68.95 5.1	10^9N/m^2
Constant stiffness multiplier (Rayleigh Damping)	β	Aluminium Epoxy	1×10^{-9} 6×10^{-9}	

Table 3.3 Modal frequencies of the host structure.

No of modes extracted	Modal Frequency (kHz)				
	Element Size Mode No	2mm	1.5mm	1mm	0.8mm
1	82	81.801	81.453	81.362	81.257
2	89.63	89.639	89.055	88.966	88.874
3	91.293	91.256	90.716	90.631	90.525
4	107.02	1.07E+02	1.06E+02	1.06E+02	1.06E+02
5	126.44	1.26E+02	1.25E+02	1.25E+02	1.24E+02
6	138.64	1.38E+02	1.37E+02	1.37E+02	1.37E+02
7	140.39	1.40E+02	1.39E+02	1.39E+02	1.39E+02
8	142.96	1.42E+02	1.41E+02	1.40E+02	1.40E+02
9	145.18	1.44E+02	1.44E+02	1.43E+02	1.43E+02
10	149.39	1.50E+02	1.48E+02	1.48E+02	1.47E+02
11	150.6	1.50E+02	1.49E+02	1.49E+02	1.49E+02
12	157.01	1.56E+02	1.54E+02	1.54E+02	1.54E+02
13	158.22	1.58E+02	1.55E+02	1.55E+02	1.54E+02
14	165.31	1.65E+02	1.63E+02	1.62E+02	1.62E+02
15	169.58	1.68E+02	1.67E+02	1.66E+02	1.66E+02
16	178.49	1.75E+02	1.73E+02	1.73E+02	1.72E+02
17	182.49	1.81E+02	1.79E+02	1.79E+02	1.78E+02
18	183.4	1.84E+02	1.81E+02	1.81E+02	1.80E+02
19	187.46	1.85E+02	1.83E+02	1.82E+02	1.82E+02
20	192.88	1.90E+02	1.88E+02	1.87E+02	1.87E+02

The signatures obtained from the dynamic harmonic analysis of the PZT- structure interaction are shown in Figure 3.10. From this figure, it can be observed that in both conductance (G)

and susceptance (B) plots, the conductance curve has acquired much lower value as compared to perfect bonding condition (where the adhesive is completely ignored). It is also observed that the peak values and the slope of susceptance signature for the adhesively bonded PZT-structure are much lower than that of the perfectly bonded PZT-structure system due to additional damping introduced by the adhesive. Again, susceptance is negative here.

The numerical coupled signatures are compared with analytical and experimental results published by Bhalla and Soh (2004c) as shown in Figure 3.11. For the sake comparison, absolute values of susceptance are considered and plotted. Both the real part as well as imaginary component has good agreement for resonance peak frequencies. For conductance, the numerical signature does not follow the slope of analytical and experimental signature. Also, the peak values are much lower than other plots. Similar observations are also found for also susceptance case.

In overall it can be recommended that the numerical signature for coupled FE piezo-elastodynamic model is not quite adequate because the slope and peak values are drastically different from analytical and experimental approach. In addition, the numerical approach FE approach leads to negative value of susceptance. This could possibly be due to some inherent error in processor of ANSYS.

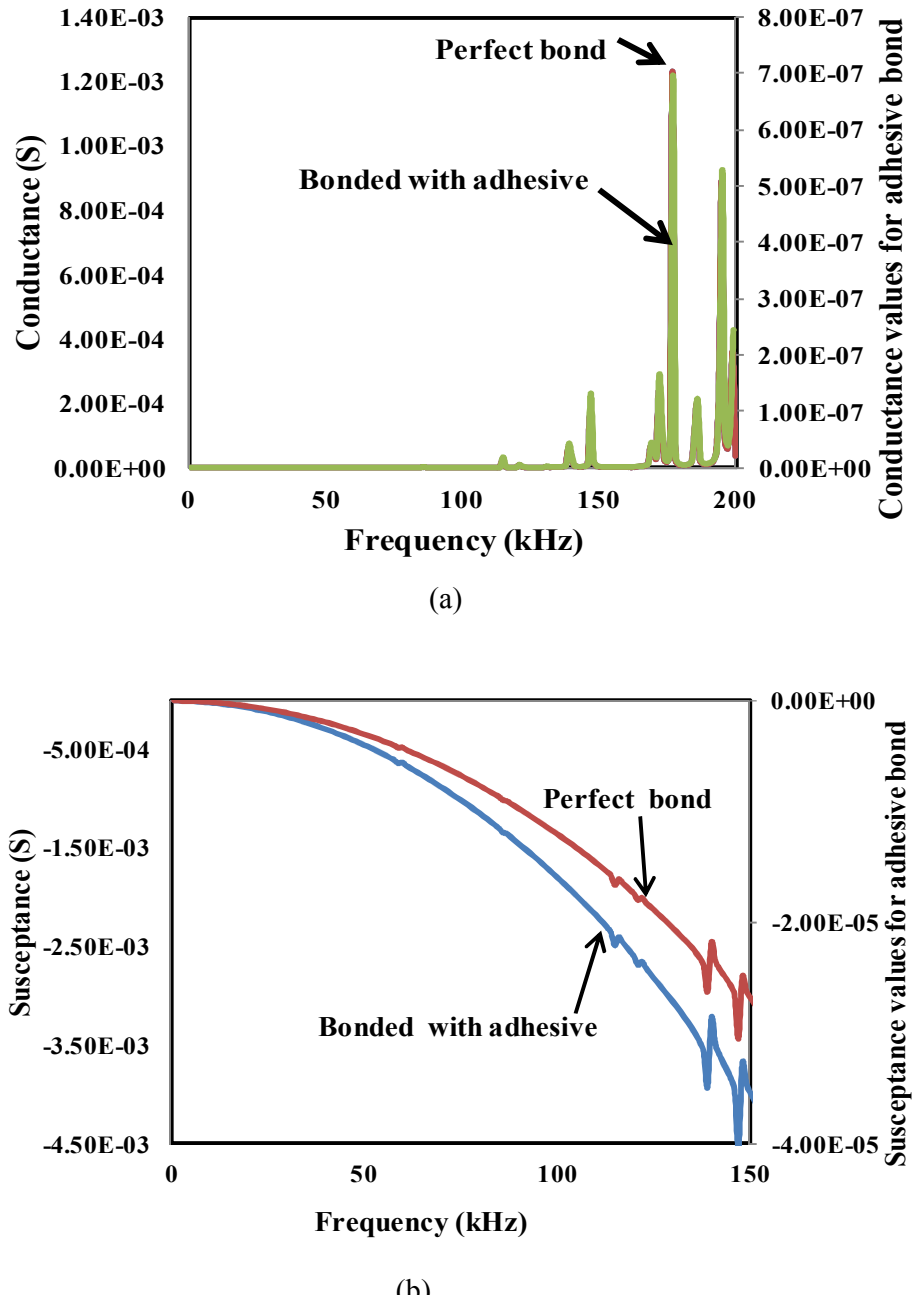


Figure 3.10 Comparison of numerical obtained signatures of perfectly bonded PZT-structure system and adhesively bonded PZT-structure interaction system

(a) Conductance (G) vs Frequency

(b) Susceptance (B) vs Frequency

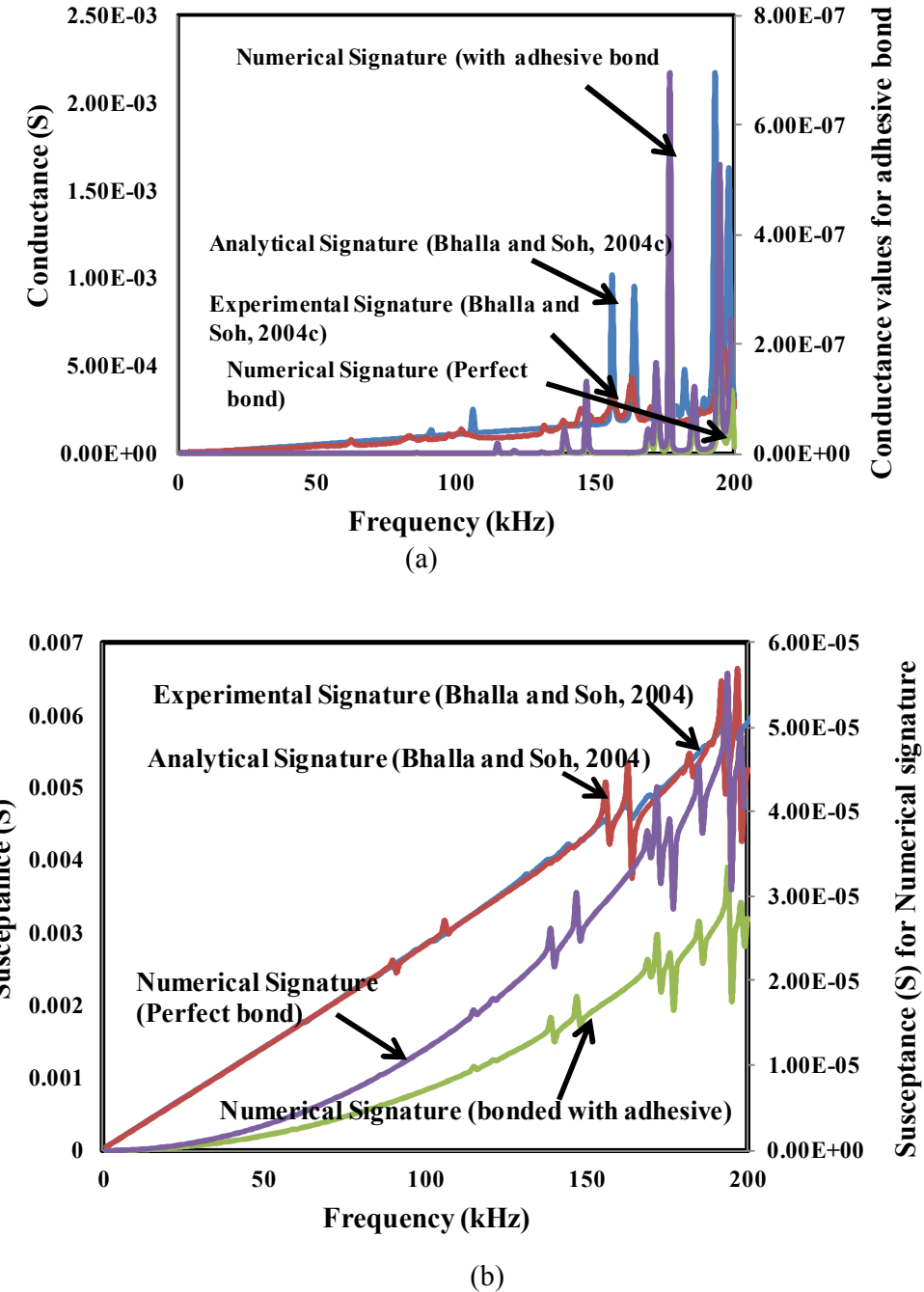


Figure 3.11 Comparison of 3D numerical EMI signature with analytical and numerical admittance signatures (Bhalla and Soh, 2004c)

(a) Conductance (G) vs Frequency

(b) Susceptance (B) vs Frequency

3.7.1 Parametric Studies for Piezo Structural Interaction

This subsection presents a brief parametric study carried out using the 3D FE model presented before.

(a) Effect of bond layer thickness

Figure 3.12 shows the plots for two different bond thicknesses i.e. 0.03mm and 0.05mm. It can be observed that, the thickness of the bond layer has significantly altered the piezo-resonance peak as it is clearly depicted from the figure.

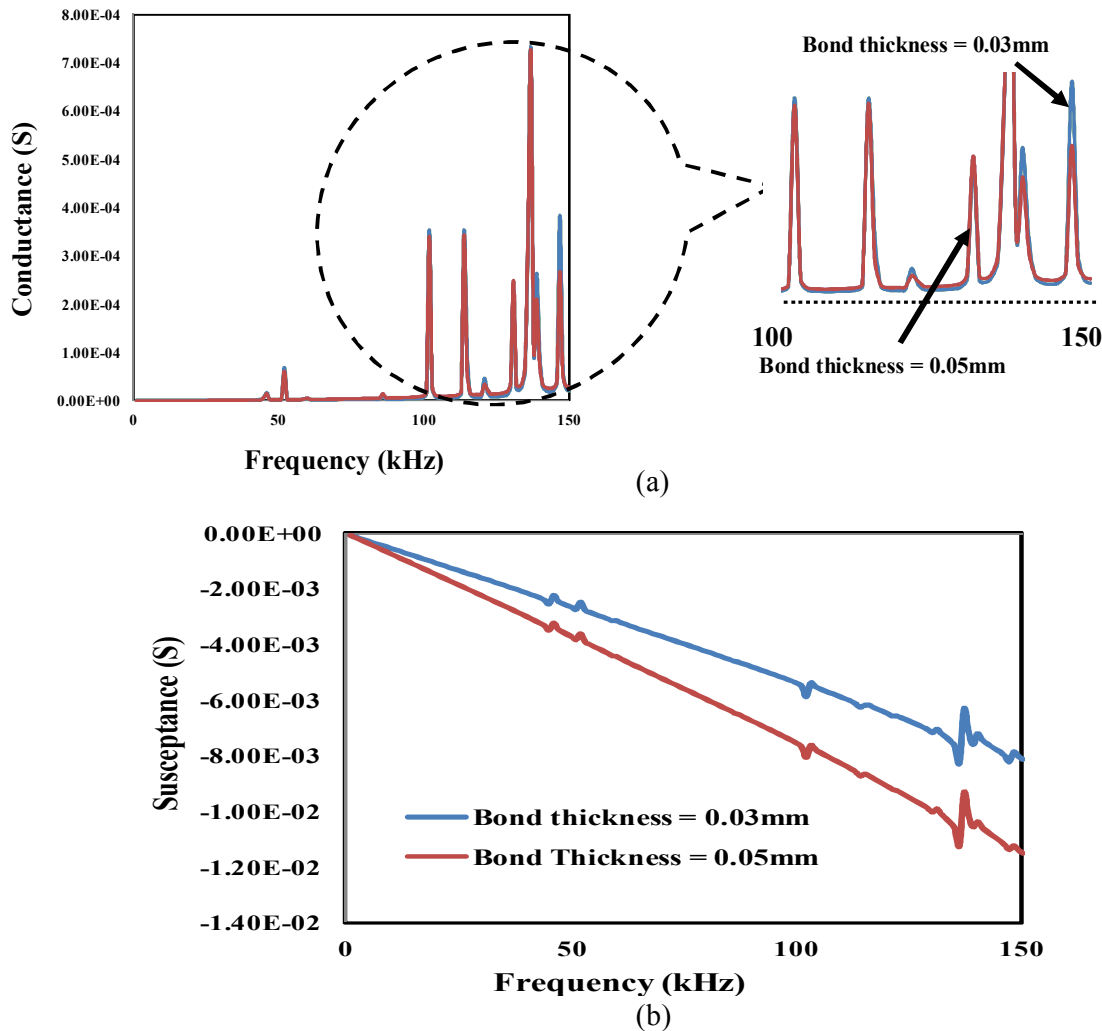


Figure 3.12 Effect of bond layer thickness on electro-mechanical admittance signature for 3D coupled analysis field

- (a) Conductance (G) vs Frequency
- (b) Susceptance (B) vs Frequency

It is apparent that as bond layer thickness increases, the peaks subside down and shift rightwards. Besides, the average slope of the susceptance curve falls down.

(b) Effect of shear modulus

Figure 3.13 shows the influence of bond layer's shear modulus on the conductance and susceptance signature. It is observed that as G_s decreases, the peaks of conductance and subsides down. In the susceptance plot, it is observed that the average slope of the curve falls down slightly, besides peaks subsiding drastically.

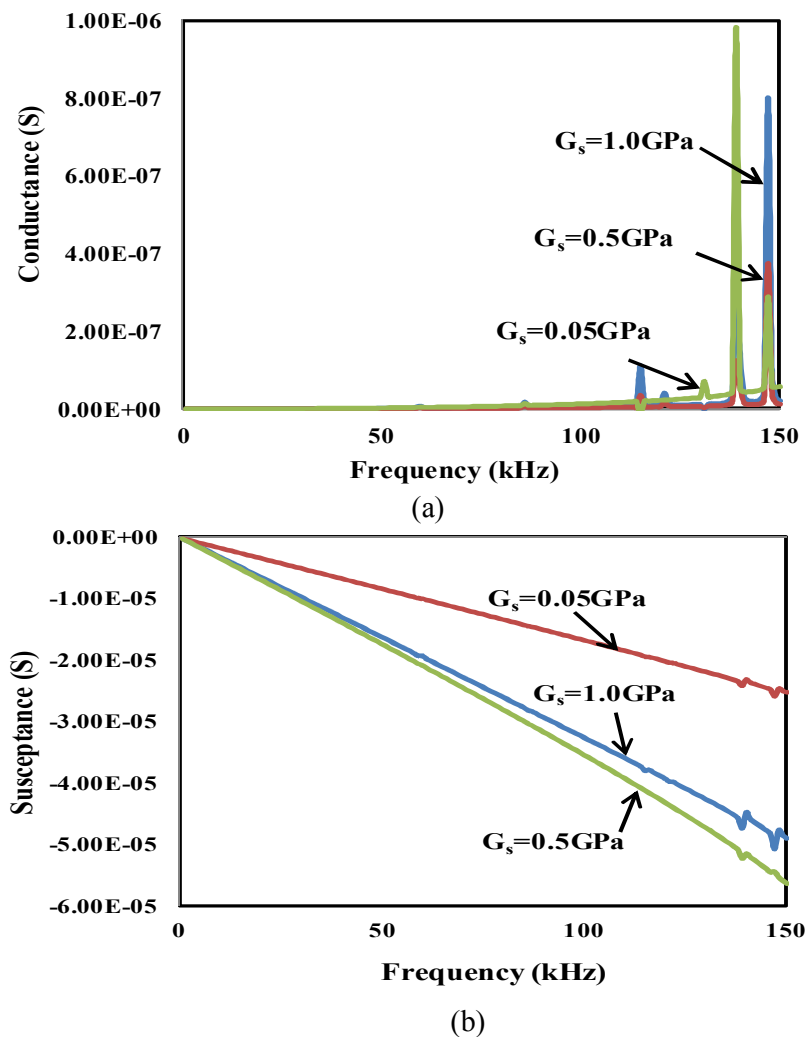


Figure 3.13 Effect of shear modulus of adhesive on electro-mechanical admittance signature obtained through 3D coupled field analysis

- (a) Conductance (G) vs Frequency
- (b) Susceptance (B) vs Frequency

In this regard, it should be noted that the imaginary part undergoes much earlier identifiable change. Hence, it could be utilized in detecting problems related to the bond layer.

(c) Effect of bond layer damping

The effect of bond layer damping on coupled FE signature is represented by Figure 3.14. It is clear from the figure that as the damping increases, the slope of the baseline conductance tends to fall down. Susceptance (see Fig 3.14(b)), also undergoes increase in the value with increase of the mechanical loss factor.

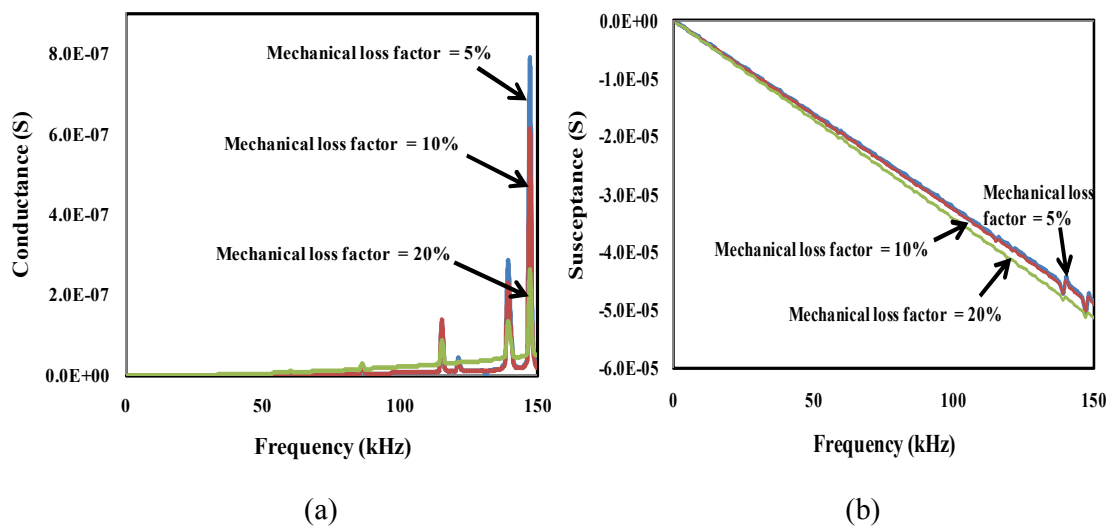


Figure 3.14 Effect of bond layer damping on coupled FE admittance signature

- (a) Conductance(G) vs Frequency
- (b) Susceptance(B) vs Frequency

3.8 CONCLUDING REMARKS

This chapter covers the coupled field analysis covering 2D and 3D FE model with inclusion of bond layer through coupling of the structural and the electrical DOF for a high range of frequency in kHz. Proposed FE model is adapted for ANSYS 12.0 by carrying out appropriate change for parameters from IEEE format to ANSYS format. This is an improvement over the previously reported work of Yang et al. (2008), where this part was ignored. The simulated signature from 2D numerical model is in good enough to capture the

shear lag effect both in conductance and susceptance plot. However, it is very much deviated from the experimental and the analytical result. For 3D case, the EMI signatures are roughly matching with experimental and previous existing semi-analytical signatures. Supportive parametric study is followed by altering piezo-mechanical parameters as well as bond conditions. The advantage offered by the coupled field analysis is that it furnishes the results directly, without the necessity of additional computation on the ANSYS output. The values are drastically different than the analytical and experimental value. However, currently it is advised to use the real part (G) only since B (susceptance) is found to be negative in values. If however, B is to be used, its sign needs to be changed by multiplying (-1). So here, we can conclude that the numerical approach for modelling shear lag phenomena is not very accurate. It is at most suitable for preliminary investigation only.

Chapter-4

DEVELOPMENT OF REFINED SHEAR LAG MODEL

4.1 INTRODUCTION

The preceding chapter has highlighted the limitations of the coupled field numerical modelling for piezo-bond structural system. The earlier analytical models of shear lag effect also have limitations as described in Chapter 2. To alleviate these problems, this chapter presents a new refined analytical model for inclusion of the shear lag effect in modelling of adhesively bonded PZT patches for consideration in the EMI technique. The previous analytical models neglected the inertial term in shear lag formulations for simplicity. The present refined model, on the other hand, considers the inertial and the shear lag effects simultaneously, and is therefore more rigorous and complete. The model is first derived for 1D case and then extended to 2D PZT-structure interaction. The refined formulations are employed for a detailed stress analysis of the bond layer. The chapter concludes with a parametric study on the influence of various sensor parameters on the EMI signatures.

4.2 DERIVATION OF PROPOSED 1D SHEAR LAG MODEL

The governing dynamic shear lag equation (Bhalla and Soh, 2004c) for a structural element shown in Figure 4.1, can be written as

$$\tau wdx + (dm) \frac{\partial^2 u_p}{\partial t^2} = \frac{\partial T_1}{\partial x} h wdx \quad (4.1)$$

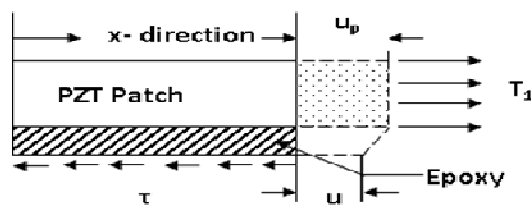


Figure 4.1 Deformation in bond layer and PZT patch.

where u_p is the displacement in the PZT patch, dm the mass of the infinitesimal element, τ the interfacial shear stress and T_1 the axial stress in the PZT patch. However, they simplified Equation (4.1) by ignoring the inertia term $(dm)\ddot{u}_p$. The simplified equation was combined with another equation adopted from the definition of mechanical impedance, that is

$$F = T_1 wh = -Z_s j\omega u \quad (4.2)$$

where Z_s is the mechanical impedance of the structure and u the host structure's displacement. The combination of the two equations (simplified Equation 4.1 and 4.2) resulted in a fourth order differential equation, which was solved for u and u_p . This equation was derived by considering equilibrium of forces at a vertical section passing through the PZT patch, as given by Equation (4.2), which basically equates the axial force in the PZT patch (negative sign implies compression) with the product of mechanical impedance and velocity (note that $\dot{u} = j\omega u$). It is assumed herein that Z_s is constant over the entire length of the PZT patch, due to its being infinitesimally small as compared to the host structure. This equation however, is not satisfied at the ends of the PZT patch, where $T_1 = 0$, as imposed by the boundary conditions that the ends of the PZT patch are stress free. In addition to this error, the model ignored the inertia term as pointed out earlier.

The refined model presented in this chapter consider Equation (4.1) in total, by duly considering the inertial term that was neglected in the previous model of Bhalla and Soh (2004c). Making substitution for following terms in the Equation (4.1),

$$dm = \rho wh dx \quad 4.3(a)$$

$$\ddot{u}_p = -\omega^2 u_p \quad 4.3(b)$$

$$T_p = \overline{Y^E} (u'_p - \Lambda) \quad 4.3(c)$$

and

$$\tau = \frac{\overline{G}_s (u_p - u)}{h_s} \quad 4.3(d)$$

where ρ is the density of the PZT patch, $\Lambda = d_{31} E_3$ the free piezoelectric strain and \overline{G}_s the complex shear modulus of elasticity of the adhesive bond layer and h_s the adhesive thickness, the equation can be reduced to a compact form as

$$\bar{\alpha} u_p - u = \frac{1}{q} u''_p \quad (4.4)$$

where

$$\bar{\alpha} = 1 - \frac{\rho h h_s \omega^2}{\overline{G}_s} \quad (4.5)$$

and

$$q = \frac{\overline{G}_s}{Y^E h_s h} \approx \frac{G_s}{Y^E h_s h} \quad (4.6)$$

Here, $\bar{\alpha}$ can be termed as the inertia parameter. $\bar{\alpha} = 1$ implies no shear lag effect (i.e. previous model of Bhalla and Soh, 2004c) and $\bar{\alpha} = 0$ implies maximum contribution of shear lag effect.

In present approach, in addition to considering the first equation rigorously, the second equation is derived from the shear stress transfer mechanism illustrated in Figure 4.1, which shows the portion of the PZT patch between coordinates 0 and x . Equating the shear force transferred between these two coordinates to the force-impedance relation, we can write

$$\int_x^l \tau w dx = Z_s j \omega u \quad (4.7)$$

or

$$\int_x^l \frac{w \overline{G}_s (u_p - u) dx}{h_s} = Z_s j \omega u \quad (4.8)$$

Differentiating both sides with respect to x , we get

$$-\frac{w\bar{G}_s(u_p - u)}{h_s} = Z_s j \omega u' \quad (4.9)$$

which can be simplified to

$$u_p = u + \frac{u'}{\bar{p}} \quad (4.10)$$

Where \bar{p} is the shear lag parameter defined by Equation (2.42). Equations (4.4) and (4.10) are the governing shear lag equations for the refined model with the shear lag parameters \bar{p} and q being same as in the previous model (Bhalla and Soh, 2004c). Differentiating Equation (4.10) twice with respect to x , we get

$$u''_p = u'' + \frac{u'''}{\bar{p}} \quad (4.11)$$

Eliminating u_p and u''_p from Equation (4.4), (making the use of Equation 4.10 and 4.11), we get the governing differential equation as

$$u''' + \bar{p}u'' - \bar{\alpha}qu' + (1 - \bar{\alpha})\bar{p}qu = 0 \quad (4.12)$$

This is homogenous differential equation, whose characteristic equation is

$$\lambda^3 + \bar{p}\lambda^2 - \bar{\alpha}q\lambda + (1 - \bar{\alpha})\bar{p}q = 0 \quad (4.13)$$

The above equation is a polynomial equation with complex coefficients, whose roots λ_1 , λ_2 and λ_3 lead to following solution for u , the displacement on the surface of the host structure.

$$u = A_1 e^{\lambda_1 x} + A_2 e^{\lambda_2 x} + A_3 e^{\lambda_3 x} \quad (4.14)$$

where A_1 , A_2 and A_3 are constants to be determined from the boundary conditions. Differentiating the Equation (4.14) with respect to x , we get

$$u' = A_1 \lambda_1 e^{\lambda_1 x} + A_2 \lambda_2 e^{\lambda_2 x} + A_3 \lambda_3 e^{\lambda_3 x} \quad (4.15)$$

Hence, from Equation (4.10), an expression for u_p can be written as

$$u_p = A_1 \left(1 + \frac{\lambda_1}{\bar{p}} \right) e^{\lambda_1 x} + A_2 \left(1 + \frac{\lambda_2}{\bar{p}} \right) e^{\lambda_2 x} + A_3 \left(1 + \frac{\lambda_3}{\bar{p}} \right) e^{\lambda_3 x} \quad (4.16)$$

Appropriate boundary conditions are now required to be imposed to determine the unknown constants A_1 , A_2 and A_3 . The first boundary condition is that at $x=0$, $u=0$, which leads to (from Equation 4.14)

$$A_1 + A_2 + A_3 = 0 \quad (4.17)$$

The second boundary condition, that is $x=0$, $u_p = 0$ leads to (from Equation 4.16)

$$\left(1 + \frac{\lambda_1}{\bar{p}} \right) A_1 + \left(1 + \frac{\lambda_2}{\bar{p}} \right) A_2 + \left(1 + \frac{\lambda_3}{\bar{p}} \right) A_3 = 0 \quad (4.18)$$

The third and the final boundary condition is that the ends of the PZT patch are stress free (Crawley and de Luis, 1987), which means that at $x=l$, the strain u'_p is equal to the free piezoelectric strain $\Lambda = d_{31}E_{31}$ (see Equation 4.3c). Hence, making use of Equation (4.16) (after differentiation), we can derive

$$\left(1 + \frac{\lambda_1}{\bar{p}} \right) \lambda_1 e^{\lambda_1 l} A_1 + \left(1 + \frac{\lambda_2}{\bar{p}} \right) \lambda_2 e^{\lambda_2 l} A_2 + \left(1 + \frac{\lambda_3}{\bar{p}} \right) \lambda_3 e^{\lambda_3 l} A_3 = \Lambda \quad (4.19)$$

The constants A_1 , A_2 and A_3 can now be obtained by solving Equations (4.17) to (4.19) simultaneously. Once determined, the constants can facilitate the determination of u and u_p at $x = l$, from which the equivalent mechanical impedance (with due consideration of shear lag effect), can be determined as (Bhalla and Soh, 2004c)

$$Z_{eq} = Z_s \frac{u_{(x=l)}}{u_{p(x=l)}} \quad (4.20)$$

which, when used in Equation (2.13), in place of $Z_{s,eff}$, facilitates deriving admittance signatures for adhesively bonded PZT patch for 1D case. The next section extends the formulations to 2D case, suitable for the 2D effective impedance model of Bhalla and Soh (2004a, 2004b).

4.3 EXTENSIONS OF REFINED SHEAR LAG FORMULATIONS TO 2D

The 2D equilibrium equations (similar to Equation 4.1 for 1D case) deduced from the free body diagram (see Figure 4.2) can be expressed as follows (De Faria, 2003 ; Zhou et al., 1996)

$$\frac{\partial T_1}{\partial x} - \frac{\tau_{zx}}{h} = \rho \ddot{u}_{px} \quad (4.21)$$

$$\frac{\partial T_2}{\partial y} - \frac{\tau_{zy}}{h} = \rho \ddot{u}_{py} \quad (4.22)$$

and

where u_{px} , u_{py} and T_1 , T_2 are the displacements and the axial stresses on the PZT patch along x and y directions respectively. From 2D PZT-structure constitutive relations (Bhalla and Soh 2004a; 2004c), the stress T_1 along x-axis can be expressed as

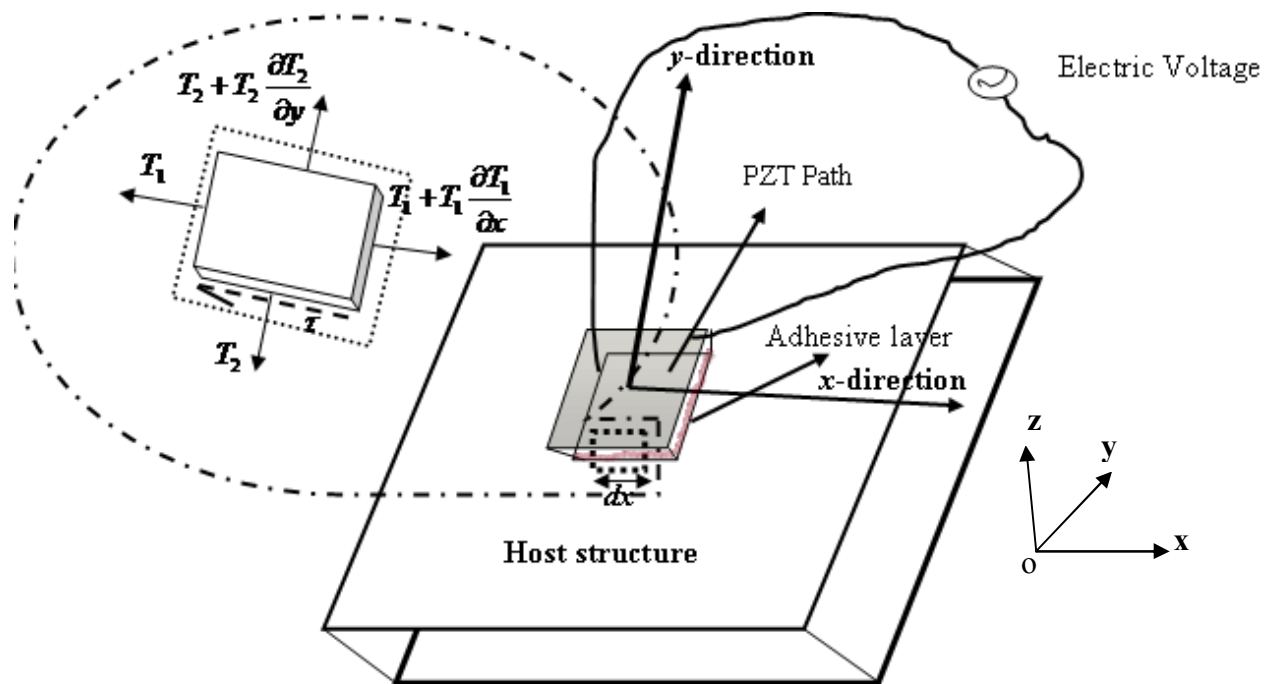


Figure 4.2 2D schematic view of PZT structure interaction model

$$T_1 = \frac{\overline{Y^E}}{(1-\nu^2)} [S_1 + \nu S_2 - \Lambda(1+\nu)] \quad (4.23)$$

where S_1 and S_2 are the strains along x and y axes respectively and ν is the Poisson's ratio.

Making note of the fact that $S_1 = u'_{px}$, and differentiating with respect to x , we get

$$\frac{\partial T_1}{\partial x} = \frac{\overline{Y^E}}{(1-\nu^2)} u''_{px} \quad (4.24)$$

Substituting Equation (4.24), 4.3(b) and 4.3(d) into Equation (4.21), and solving, we get

$$\frac{\overline{Y^E}}{(1-\nu^2)} u''_{px} - \frac{\overline{G_s}}{h h_s} (u_{px} - u_x) = -\rho \omega^2 u_{px} , \quad (4.25)$$

which can be further reduced as

$$\bar{\alpha} u_{px} - u_x = \frac{1}{q_{eff}} u''_{px} \quad (4.26)$$

$$\text{where } q_{eff} = \frac{\overline{G_s}(1-\nu^2)}{\overline{Y^E} h h_s} \quad (4.27)$$

is the 2D equivalent shear lag parameter as q for 1D. Similarly, using Equation (4.22) for y direction, we can derive

$$\bar{\alpha} u_{py} - u_y = \frac{1}{q_{eff}} u''_{py} \quad (4.28)$$

Adding Equations (4.26) and (4.28) and dividing by 2, we get

$$\bar{\alpha} \left(\frac{u_{px} + u_{py}}{2} \right) - \left(\frac{u_x + u_y}{2} \right) = \frac{1}{q_{eff}} \left(\frac{u''_{px} + u''_{py}}{2} \right) \quad (4.29)$$

Making use of the definition of effective displacement (Bhalla and Soh, 2004a), this can be expressed in a compact form as

$$\bar{\alpha}u_{(p,eff)} - u_{eff} = \frac{1}{q_{eff}}u''_{(p,eff)} \quad (4.30)$$

The second governing 2D shear lag equation (equivalent to Equation 4.11 for 1D case), can similarly be derived, using the concept of effective displacement, as

$$\left(\frac{u_{px} + u_{py}}{2}\right) = \left(\frac{u_x + u_y}{2}\right) + \frac{\left(\frac{u'_x + u'_y}{2}\right)}{\bar{p}_{eff}} \quad (4.31)$$

or

$$u_{p,eff} = u_{eff} + \frac{u'_{eff}}{\bar{p}_{eff}} \quad (4.32)$$

where

$$\bar{p}_{eff} = -\frac{2l\bar{G}_s(1+\nu)}{Z_{eff}j\omega h_s} \quad (4.33)$$

is the 2D equivalent shear lag parameter as p for 1D (Bhalla and Soh, 2004c). Combining Equations (4.30) and (4.32) as in the 1D case and solving, the governing differential equation results as

$$u'''_{eff} + \bar{p}_{eff}u''_{eff} - \alpha q_{eff}u'_{eff} + (1-\bar{\alpha})\bar{p}_{eff}q_{eff}u_{eff} = 0 \quad (4.34)$$

For solving the above homogenous equation, its characteristic equation can be written as

$$\lambda^3 + \bar{p}_{eff}\lambda^2 - \bar{\alpha}q_{eff}\lambda + (1-\bar{\alpha})\bar{p}_{eff}q_{eff} = 0 \quad (4.35)$$

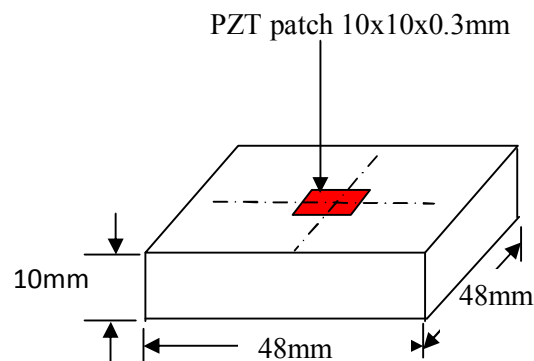
Now, this expression is similar to the polynomial equation with complex coefficients for the 1D analysis (see Equation 4.13) but the parameters represent 2D interaction. It has similar three roots λ_1, λ_2 and λ_3 as for the 1D case. The final solution for u_{eff} and $u_{p,eff}$ is similar to the 1D case with same boundary conditions. The equivalent effective impedance ($Z_{s,eq,eff}$) for 2D refined shear lag model can thus be determined as

$$Z_{s,eq,eff} = Z_{s,eff} \left(\frac{u_{eff}(x=l)}{u_{p,eff}(x=l)} \right) \quad (4.36)$$

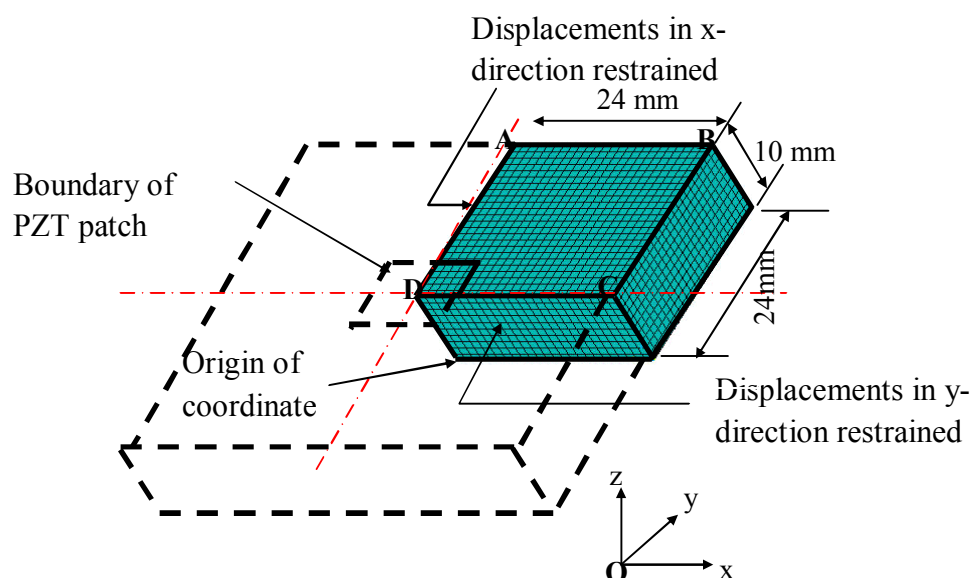
The above 2D shear lag based impedance term can be directly used in Equation (2.29) using $Z_{s,eq,eff}$ in place of $Z_{s,eff}$ to obtain the admittance signature duly considering the shear lag effect. A matlab code is enlisted in Appendix A for the refined EMI signature.

4.4 COMPARISION WITH PREVIOUS MODELS AND EXPERIMENT

The new formulations derived above were compared with the results published by Bhalla and Soh (2004b, 2004c). The test structure consisted of an aluminium block (grade Al 6061 T6), 48×48×10 mm in size, instrumented with a PZT patch of size 10×10×0.3mm (grade PIC 151, PI Ceramic 2003), as shown in Figure 4.3(a). Table 4.1 lists the key physical parameters of the PZT patch, the aluminium block and the adhesive, considered while deriving the theoretical signatures. Figure 4.3(b) shows the 3D finite element model of a quarter of the test structure (Bhalla and Soh 2004b), developed to determine the effective impedance, $Z_{s,eff}$, for use in deriving the theoretical signatures. $Z_{s,eff}$ was obtained by applying a distributed harmonic force along the boundary of the PZT patch (see Figure 4.3(b)), carrying out dynamic harmonic analysis, and obtaining the effective displacement u_{eff} , from which $Z_{s,eff}$ was obtained as the ratio of the effective force to the effective velocity (see Equation 2.19). The equivalent effective impedance (taking into consideration the shear lag effect as per the new refined model) was obtained using Equation (4.36). The PZT patch was assumed to be bonded to the block using RS 850-940 two-part epoxy adhesive (RS Components, 2003). A bond layer thickness of 0.125mm was considered with $G_s = 1.0$ GPa and the related mechanical loss factor η' as 10% respectively.



(a)



(b)

Figure 4.3 PZT-Structure Interaction Model

(a) Aluminum block structure

(b) Finite element model of a quarter of structure

Table 4.1 Parameters of PZT patch, aluminum block and adhesive bond

MATERIAL	PHYSICAL PARAMETER	VALUE
PZT Patch	Electric permittivity ϵ_{33}^T (F/m)	1.7785×10^{-8}
	Peak correction factor (C_1)	0.898
	$k = \frac{2d_{31}^2 Y^E}{(1-\nu)}$ (N/V ²)	5.35×10^{-9}
	Mechanical loss factor η	0.0325
	Dielectric loss factor δ	0.0224
Aluminum Block	Young's modulus (GPa)	68.95
	Density (Kgm ⁻³)	2715
	Poisson's ratio	0.33
	Rayleigh damping coefficients	
Adhesive	α	0
	β	3×10^{-9}
Adhesive	Shear modulus (G_s) (GPa)	1
	Mechanical loss factor η'	0.1

Figures 4.4 and 4.5 shows a comparison of the plots of conductance (G) and susceptance (B) respectively over a frequency range 0-250 kHz with those obtained using the previous model (Bhalla and Soh 2004c). It can be observed that using the new refined model, the peaks of both the conductance as well as susceptance plots are lower than the predictions of the previous model, a consequence of the inclusion of the inertial effects. This can be more appreciated by the graph shown in part (b) of Figures 4.4 and 4.5, where the focus is near the resonance peaks.

For experimental comparison, the adhesive layer thickness was maintained at 0.125 mm for two specimens using two optical fiber pieces of this diameter (Bhalla and Soh, 2004c). The two specimens have (h_s/h_p) ratio equal to 0.417 and 0.833 respectively.

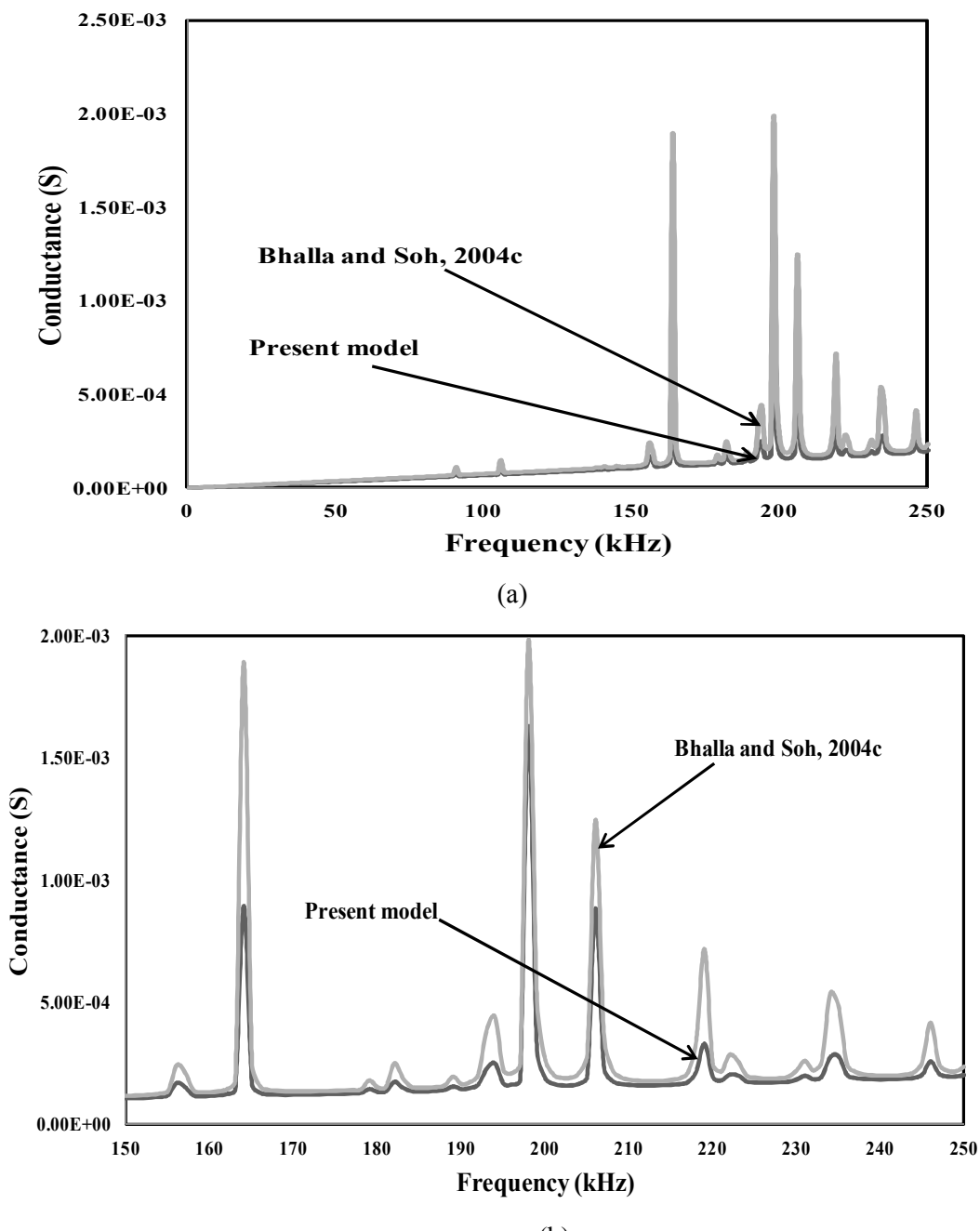


Figure 4.4 Comparison of refined conductance signature with previous analytical model (Bhalla and Soh, 2004c)

(a) Plot in 0-250 kHz range

(b) Closer view in 150-250 kHz range

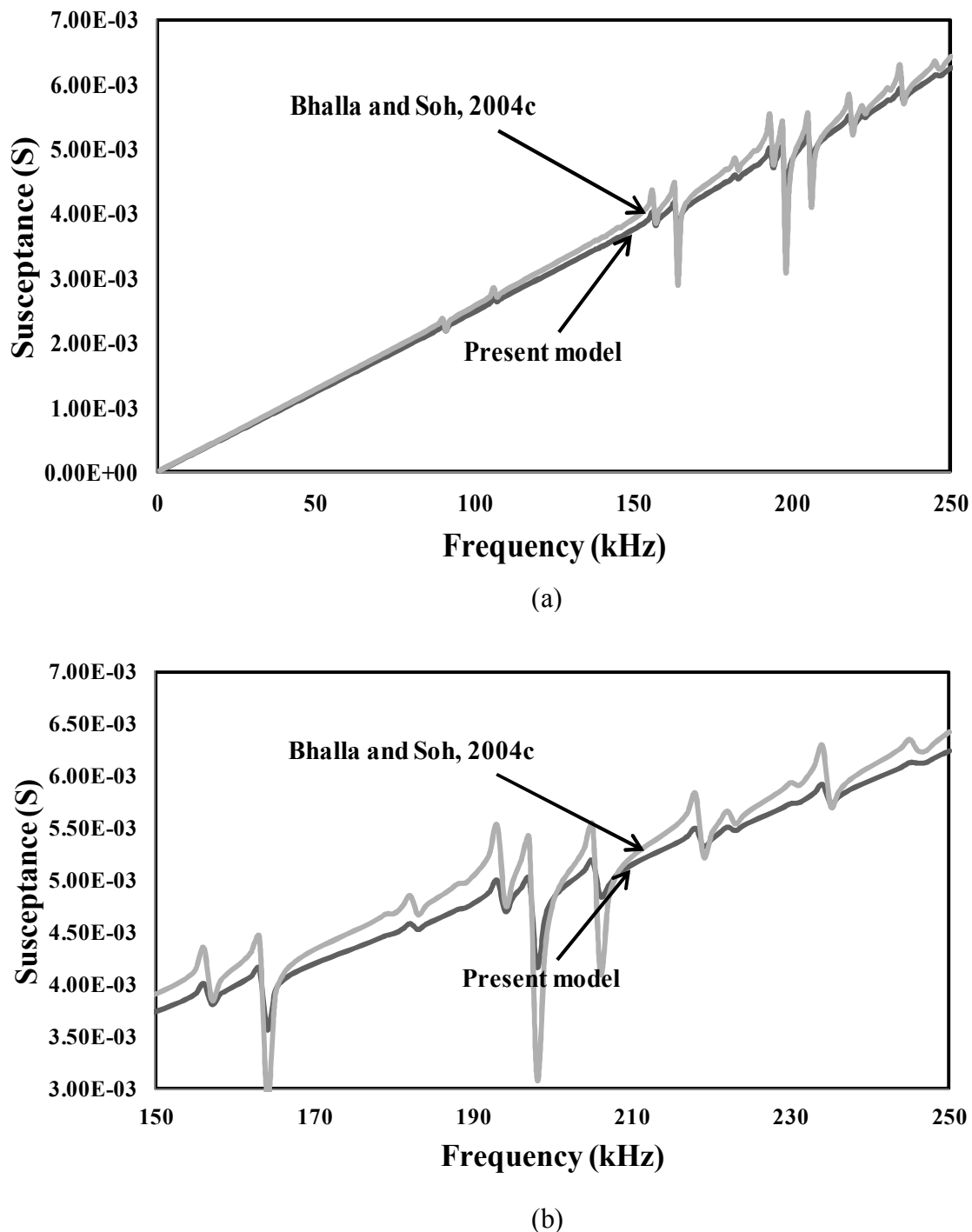


Figure 4.5 Comparison of refined susceptance signature with previous analytical model (Bhalla and Soh, 2004c)

(a) Plot in 0-250 kHz range

(b) Closer view in 150-250 kHz range

Figure 4.6 compares signatures of three model i.e. Zhou et al., (1994) (Perfect bond), Bhalla and Soh (2004c), and the present refined model. The bond effect makes significant impact on coupled signature as visible from the figures.

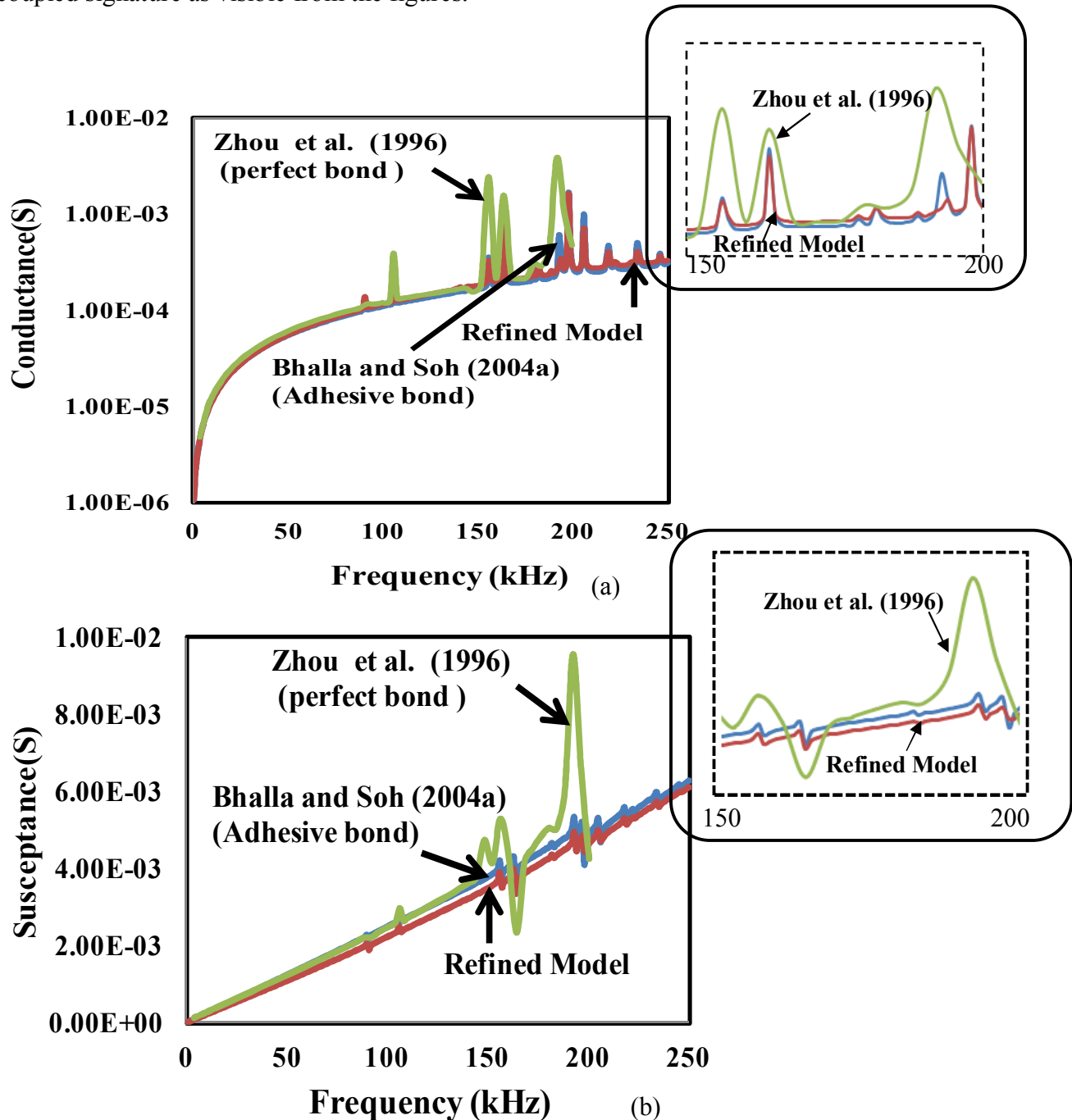


Figure 4.6 Comparison of admittance signature with previous analytical models (Zhou et al., 1996 (perfect bond); Bhalla and Soh, 2004c)

- (a) Conductance (G) vs Frequency
- (b) Susceptance (B) vs Frequency

Figures 4.7 and 4.8 compare the analytical and experimental conductance and susceptance signatures respectively for the two different bond thickness ratio ($h_s/h_p = 0.417$) and ($h_s/h_p = 0.834$). Since bond thickness was kept constant and PZT patches are of different thicknesses (0.3mm and 0.15mm respectively) has been used, normalized values, i.e. Gh/l^2 and Bh/l^2 are compared rather than the absolute values. From these comparisons, it can be observed that the present model is qualitatively much better match with experimental observations.

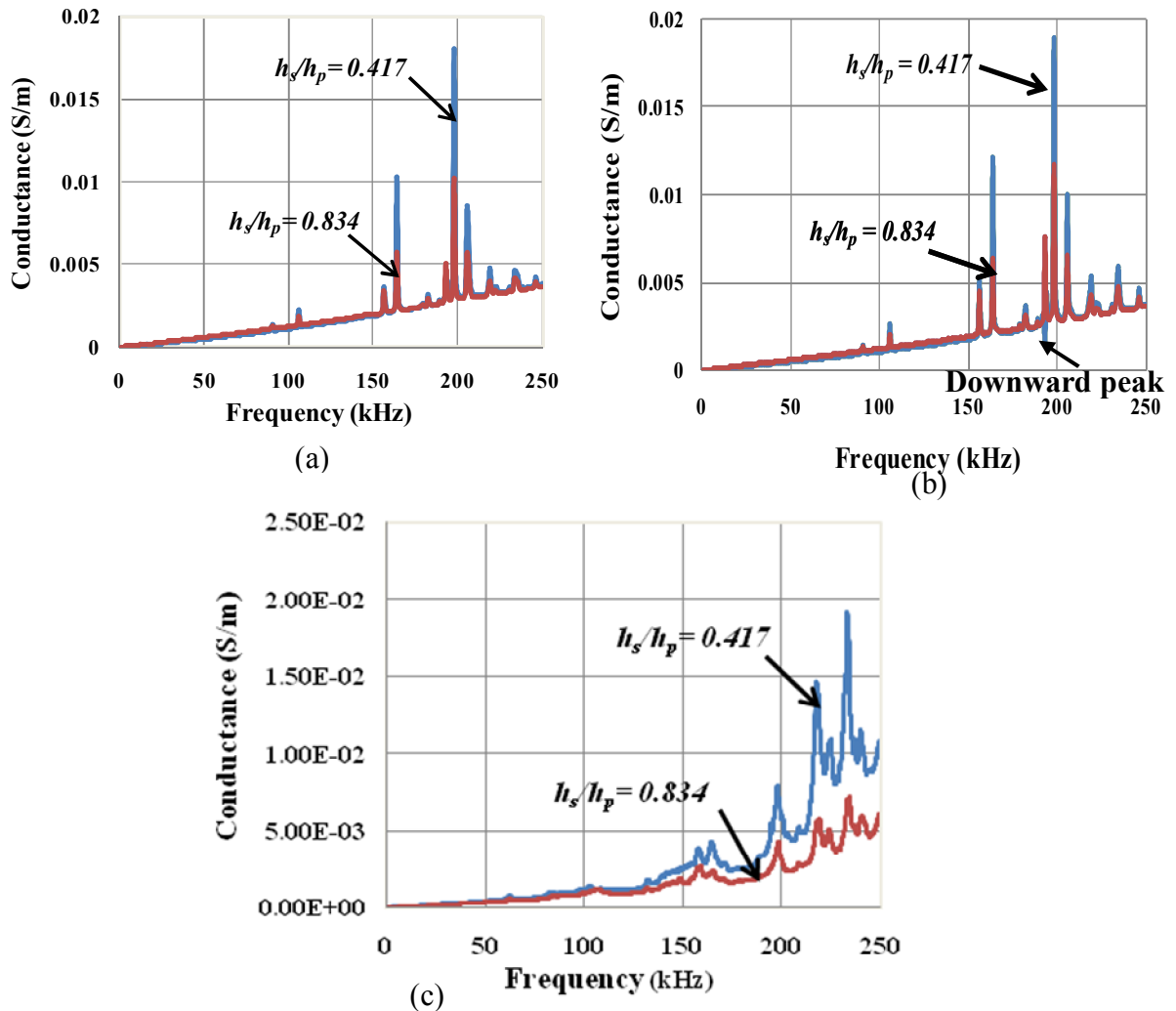


Figure 4.7 Comparison of conductance of experimental data (Bhalla and Soh, 2004c) with proposed model

- (a) Normalized analytical conductance (Refined model)
- (b) Normalized analytical conductance (Bhalla and Soh, 2004c)
- (c) Normalized experimental conductance (Bhalla and Soh, 2004c)

The resonance peak of refined model has more sensitive to bonding effect as it can be seen that, the peak values dropped to low as accordance to bond thickness ratio (h_s/h_p) as shown in Figure 4.7(a). This is because of the more accurate modelling and involving the inertia term. The refined model's performance is further enhanced in sense that it removes a discrepancy (negative peak around 198kHz) that lied with previous model (see Figure 4.7(b)).

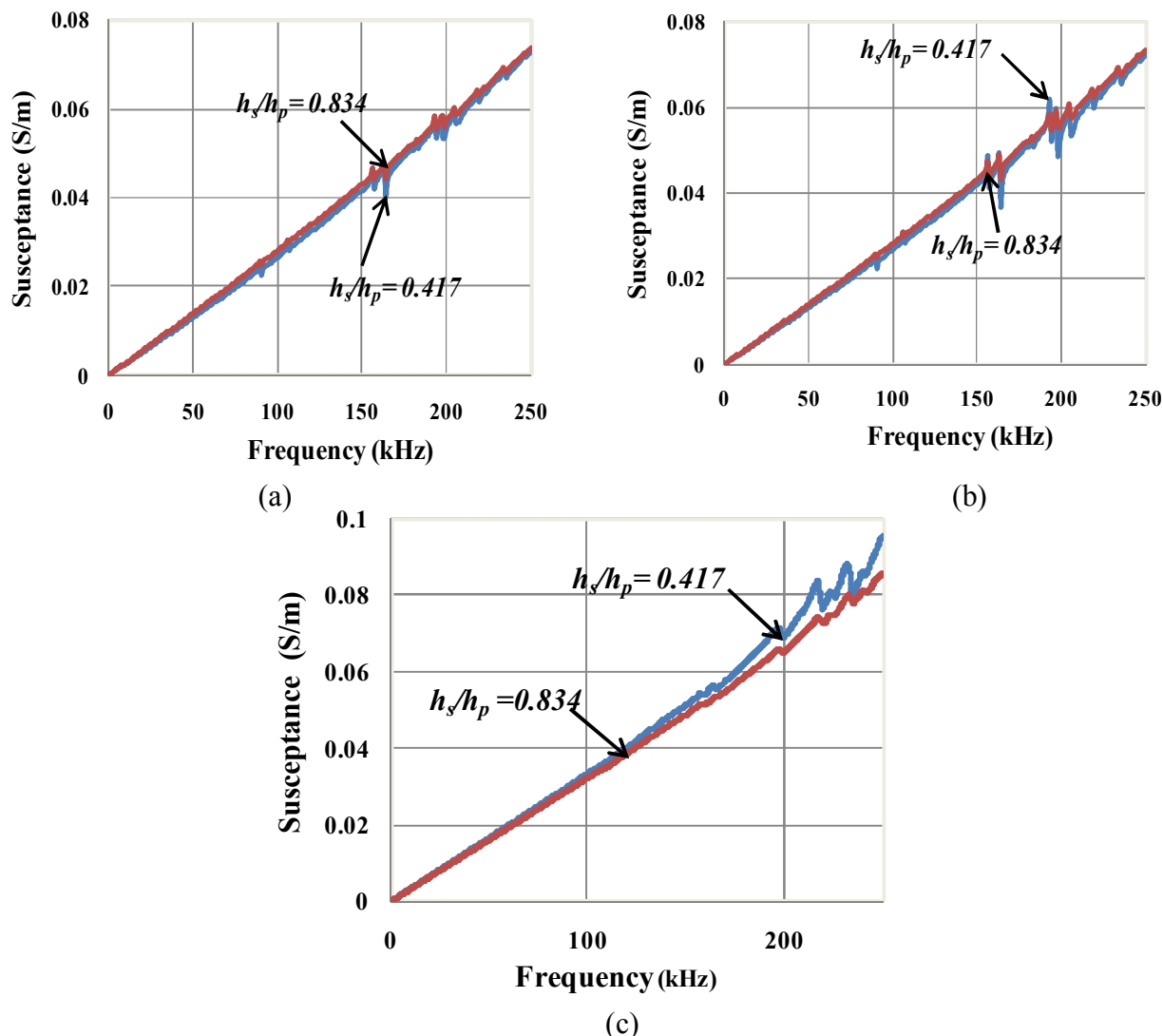


Figure 4.8 Comparison of susceptance of experimental data (Bhalla and Soh, 2004c) with proposed model

- (a) Normalized analytical susceptance (Refined model)
- (b) Normalized analytical susceptance (Bhalla and Soh, 2004c)
- (c) Normalized experimental susceptance (Bhalla and Soh, 2004c)

4.5 EFFECT OF INCLUSION OF ADHESIVE MASS

After properly accounting for the inertia effect of the PZT patch, this section goes one step further to include the mass of adhesive (in term dm of Equation 4.1) so far not considered in any previous approach. After considering the mass of the adhesive, the inertial term of Equation (4.1) can be rewritten as

$$I = dm_p \ddot{u}_p + dm_s \ddot{u}_s \quad (4.37)$$

where dm_p and dm_s are the differential masses of the PZT patch and the adhesive respectively and \ddot{u}_p and \ddot{u}_s the corresponding velocities.

Further,

$$dm_p = \rho wh \quad 4.38(a)$$

$$dm_s = \rho_s wh_s \quad 4.38(b)$$

$$\ddot{u}_p = -\omega^2 u_p \quad 4.38(c)$$

$$\ddot{u}_s = -\omega^2 \left(\frac{u_p + u}{2} \right) \quad 4.38(d)$$

where ρ_s is the density of the adhesive. It may be noted from Equation 4.38 (d) that average velocity has been considered for the adhesive layer, assuming a linear variation from u (at surface of host structure) to u_p (at bottom of the PZT patch), as can be seen from Figure (4.1)). With above substitutions, Equation (4.4) can be modified as

$$\left[1 - \frac{\rho h h_s \omega^2}{\bar{G}_s} - \frac{\rho_s h_s^2 \omega^2}{2\bar{G}_s} \right] u_p - \left[1 + \frac{\rho_s h_s^2 \omega^2}{2\bar{G}_s} \right] u = \frac{1}{q} u''_p \quad (4.39)$$

In compact form, we can write

$$\overline{\alpha}' u_p - \overline{\beta} u = \frac{1}{q} u''_p \quad (4.40)$$

where $\overline{\alpha}'$ is the modified inertia parameter (see Equation 4.5), expressed as

$$\overline{\alpha}' = 1 - \frac{\left(\rho h + \frac{\rho_s h_s}{2} \right) h_s \omega^2}{\overline{G}_s} \quad (4.41)$$

and $\overline{\beta}$ is the second inertia parameter, given by

$$\overline{\beta} = 1 + \frac{\rho_s h_s^2 \omega^2}{2 \overline{G}_s} \quad (4.42)$$

Similarly, for the case of 2D effective impedance, Equation (4.25), can be reformed for x -direction (adding inertia term for the adhesive)

$$\frac{\overline{Y}^E}{(1-\nu^2)} u''_{px} - \frac{\overline{G}_s}{h h_s} (u_{px} - u_x) = -\rho \omega^2 u_{px} - \rho_s \omega^2 \left(\frac{u_{px} + u_x}{2} \right) \quad (4.43)$$

Equation (4.30) thus gets modified for inclusion of adhesive mass as

$$\left[1 - \frac{\rho h h_s \omega^2}{G_s} - \frac{\rho_s h h_s \omega^2}{2 G_s} \right] u_{p,eff} - \left[1 + \frac{\rho_s h h_s \omega^2}{2 G_s} \right] u_{eff} = \frac{1}{q_{eff}} u''_{p,eff} \quad (4.44)$$

In compact form, it can be expressed as

$$\overline{\alpha}'_{eff} u_{p,eff} - \overline{\beta}_{eff} u_{eff} = \frac{1}{q_{eff}} u''_{p,eff} \quad (4.45)$$

where q_{eff} is given by Equation (4.27) and $\overline{\alpha}'_{eff}$ and $\overline{\beta}_{eff}$ are redefined for 2D case as

$$\overline{\alpha}'_{eff} = \left(1 - \frac{\left(\rho + \frac{\rho_s}{2} \right) \omega^2 h h_s}{\overline{G}_s} \right) \quad 4.46(a)$$

and

$$\overline{\beta_{eff}} = \left(1 + \frac{\rho_s \omega^2 h h_s}{2 \overline{G}_s} \right) \quad 4.46(b)$$

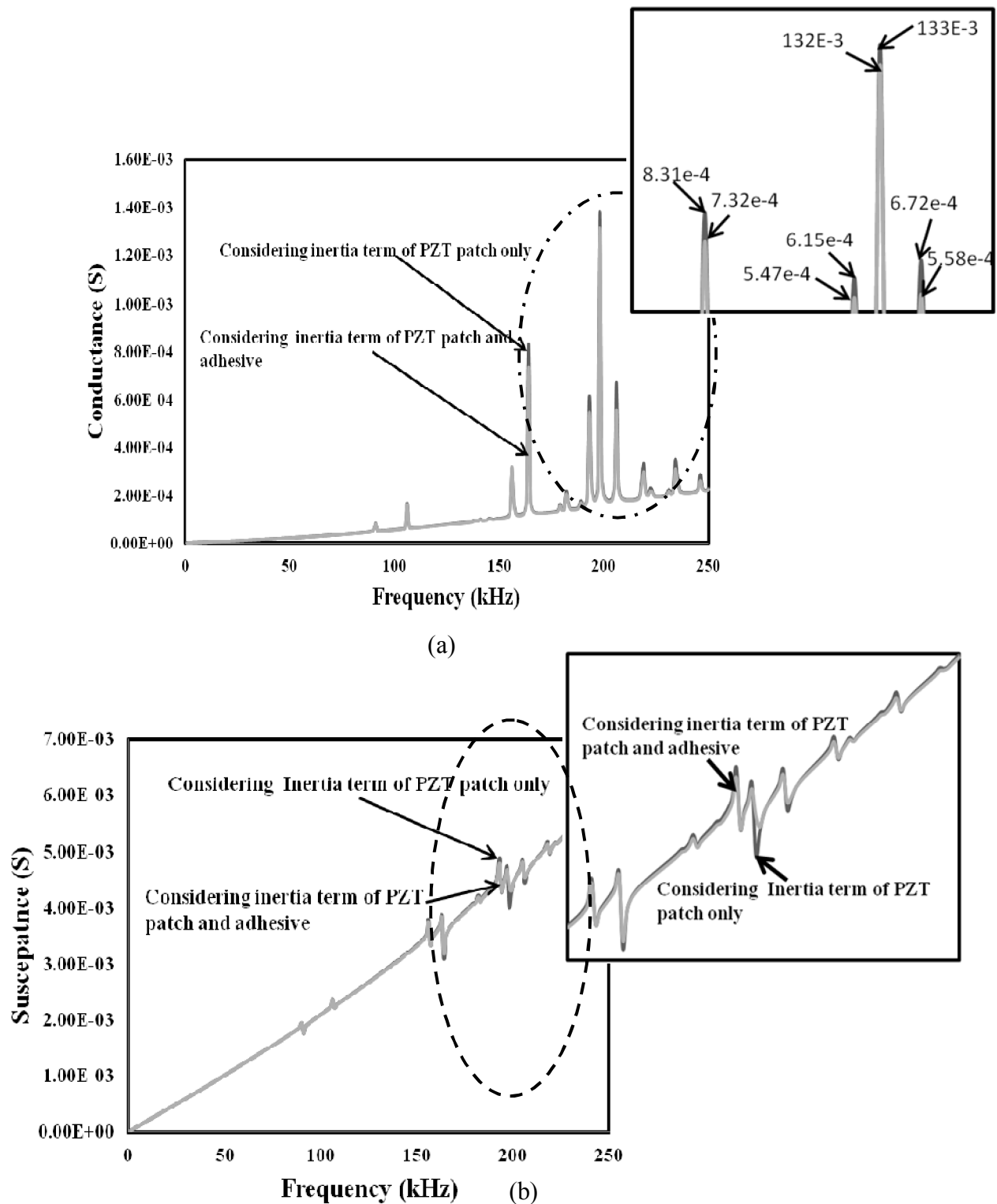
The second governing equation of shear lag, namely Equation (4.32) will remain unchanged. Combining Equations (4.32) and (4.45), eliminating the $u_{p,eff}$, we can obtain the modified governing differential equation as

$$u'''_{eff} + \overline{p}_{eff} u''_{eff} - \overline{\alpha'_{eff}} q_{eff} u'_{eff} + (\overline{\alpha'_{eff}} - \overline{\beta_{eff}}) \overline{p}_{eff} q_{eff} = 0 \quad (4.47)$$

Repeating the same procedure (with similar characteristic equation and boundary conditions) to solve the homogenous differential equation as it was done in the 1D and 2D case of previous sections, Equation (4.47) can be solved. A MATLAB code for derivation of EMI signature for this combined inertia effect is enlisted in Appendix B. Figure 4.9 shows the plots of G and B based on above considerations for $h_s=0.125\text{mm}$ and compare them with those obtained by neglecting the adhesive mass. On close inspection, it can be observed that the inclusion of the adhesive mass leads to further lowering the peaks of G and B and also the overall slopes of B slightly. However, at the same time, it can also be noted that neglecting the mass of the adhesive will not make as significant difference as neglecting the inertia term. Hence, the mass of the adhesive can possibly be ignored.

4.6 INTERFACIAL STRESS AND STRAIN ANALYSIS FOR COUPLED PHENOMENA

In recent years, the PZT patches have been utilized as both sensors and actuators in SHM techniques. For EMI technique, the common configuration of integrated monitoring is to surface-bond piezoelectric patches to the host structure through a bonding layer. In an integrated sensor-structural system, evaluating the interfacial stresses between the layers is important in two aspects.

**Figure 4.9** Effect of mass of adhesive on signature(a) Conductance (G) vs Frequency(b) Susceptance (B) vs Frequency

First, excessive interfacial stresses can delaminate the bond layer and cause failure of the monitoring system. Second, the distribution of these stresses determines the actuation capacity of the piezoelectric actuator. In other words, the effectiveness of the strain transfer of the actuator depends on the stress (or strain) distributions along the bonding layer (Ryu and Wang, 2004).

Till now, FEM is the only technique used to examine the interfacial stresses of bonding layers. Robbins and Reddy (1991) analyzed stress variation from piezoelectrically actuated beams using a layer-wise displacement theory. However, the drawback of the FEM is that the values of interfacial stresses significantly depend on the mesh size as Seemann et al. (1997) concluded from their study. A MATLAB code is enlisted in Appendix D to simulate the shear stress, strain and effective axial stress for refined model.

4.6.1 Shear Stress Profile along Bond Layer

This section investigates the distribution of the shear stress within the bond layer, using the refined model developed in this chapter. The shear stresses cannot be directly measured experimentally for the minutely thick PZT-adhesive-structure system. Hence, analytical approach or FEM are the only possible avenues for stress analysis. In this investigation, Equation 4.3(d) is employed, by replacing u_p and u by $u_{p,eff}$ and u_{eff} respectively, the resulting equation can be expressed as

$$\tau = \frac{\bar{G}_s}{h_s} (u_{p,eff} - u_{eff}) = \frac{\bar{G}_s}{h_s} \left(A_1 e^{\lambda_1 x} \left(\frac{\lambda_1}{\bar{P}_{eff}} \right) + A_2 e^{\lambda_2 x} \left(\frac{\lambda_2}{\bar{P}_{eff}} \right) + A_3 e^{\lambda_3 x} \left(\frac{\lambda_3}{\bar{P}_{eff}} \right) \right) \quad (4.48)$$

For simplicity, the inertia term associated with the adhesive is ignored. Figure 4.10 shows the plot of the interfacial shear stress as a function of distance, from $x=0$ to $x=l$ at a frequency of 91 kHz (first resonance peak). It should be noted that this plot shows the absolute values. From the

plot, it can be observed that, the stress is zero at $x=0$, increases to the maximum value and then remain constant.

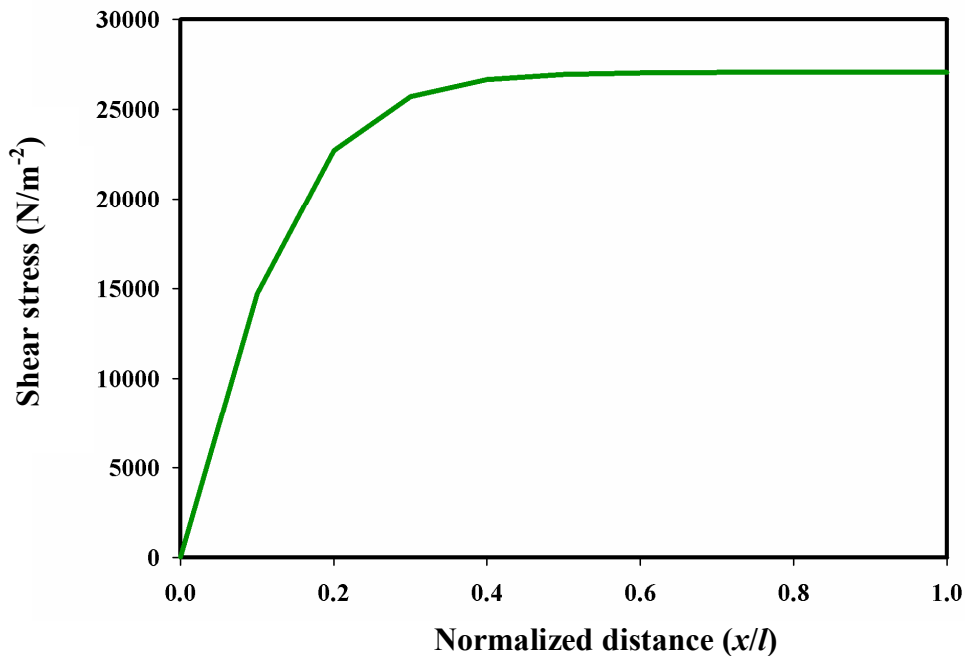


Figure 4.10 Variation of shear stress in bond layer

Figure 4.11 (a) and (b) depict the behaviour of shear profile along the bond length (at 91 kHz) with respect to the parametric change of bond properties mechanical loss factor of bond and bond thickness respectively. From Figure 4.11(a), it can be noted that the shear stress increases marginally with increasing value of bond layer's damping. Similarly, Figure 4.11(b) shows the effect of bond layer thickness on the shear stress. It can be observed that the shear stress distribution tends to be uniform with decreasing bond layer thickness. Hence, it is recommended that the bond layer thickness be maintained minimum possible for better force transfer. However, it should be noted that, it should not be too low to increase shear stress beyond the permissible limit.

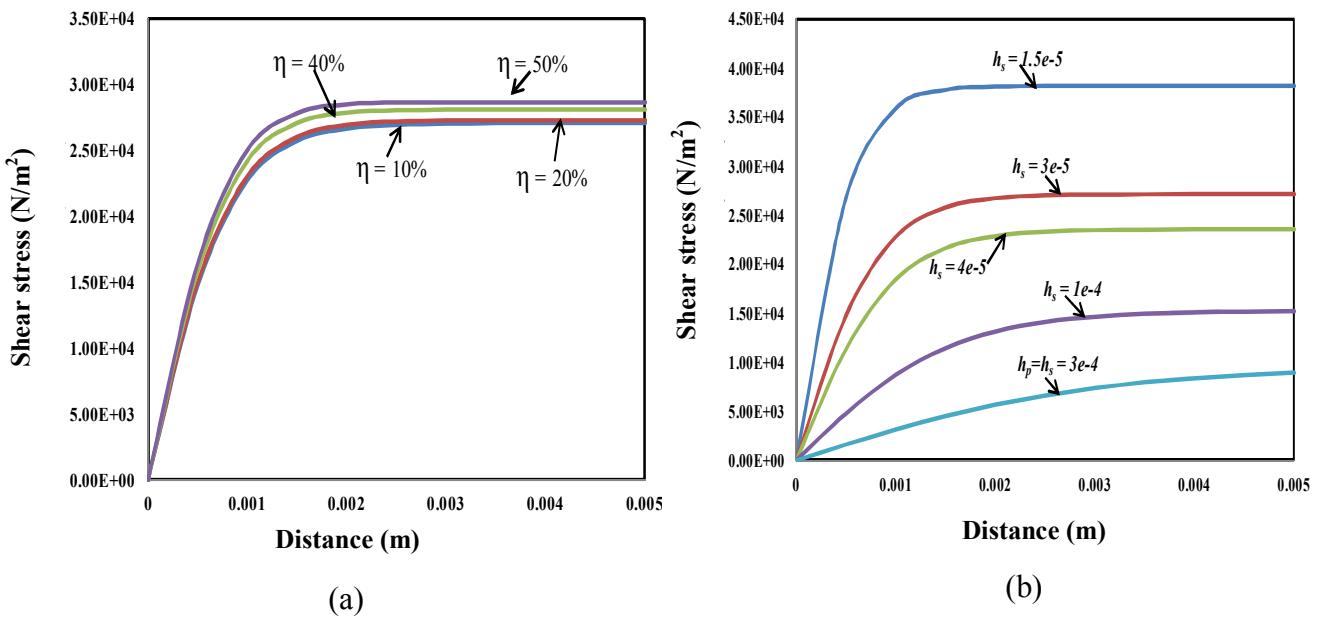


Figure 4.11 Profile of interfacial shear stress distribution

- (a) Effect of mechanical damping of bond layer
- (b) Effect of bond layer thickness

The effect of the shear modulus of adhesive bond on shear stress (at 91kHz) is shown in Figure 4.12. It is observed that the shear distribution tends to be uniform with increasing shear modulus. Therefore, bond with higher shear modulus is more desirable for better shear interaction, however such that shear stress is within permissible limit. This refined model facilitates studying the effect of the inertia parameter $\bar{\alpha}$. In Figure 4.13, the effect of $\bar{\alpha}$ on shear stress has been examined. The variation is highlighted at higher peak region of the shear profile, where it is very clear that, the shear stress increases marginally with $\bar{\alpha}$ in the peak region. At other points, hardly any effect is noticed.

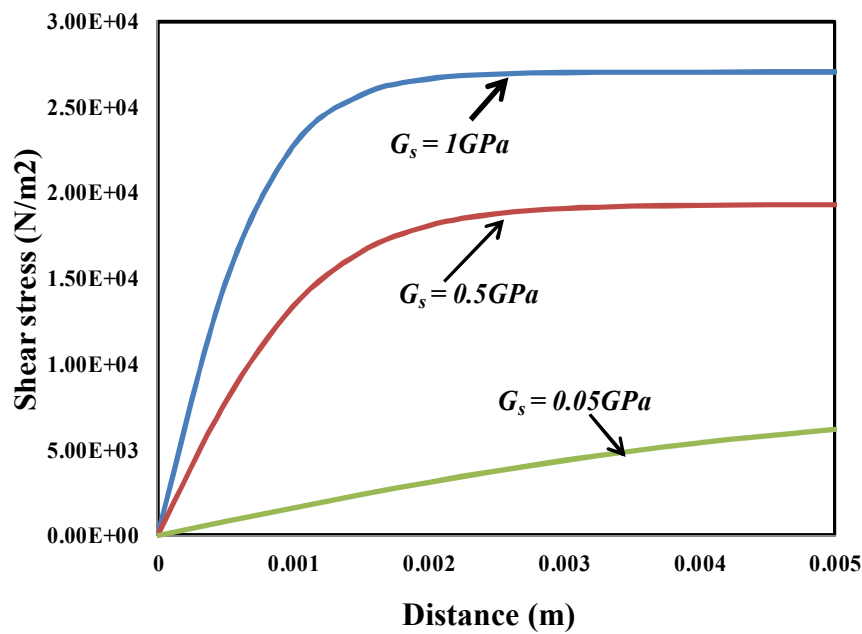


Figure 4.12 Effect of bond layer's shear modulus on shear stress profile

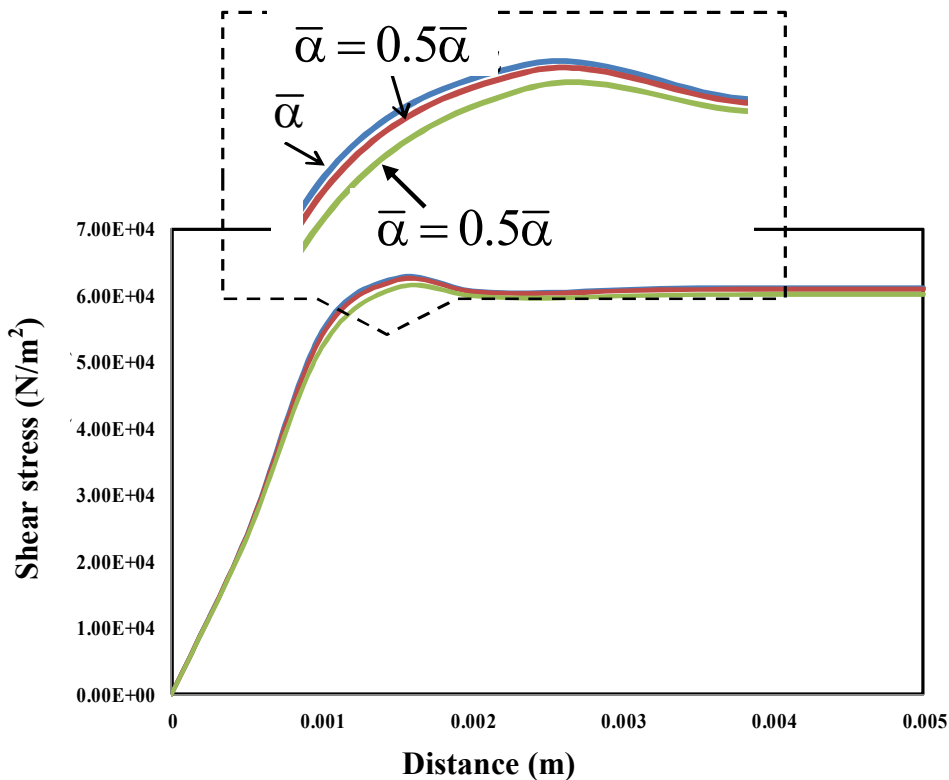


Figure 4.13 Effect of inertia parameter $\bar{\alpha}$ on shear stress

4.6.2 Effective Strain Profile along Bond Layer

Figure 4.14 similarly shows a plot of the effective strain ($u'_{p,eff}$) in the PZT patch along the length at 91kHz. Mathematically it can be expressed as (from Equation 4.16)

$$S_{eff} = u'_{p,eff} = \left(1 + \frac{\lambda_1}{\bar{P}_{eff}}\right) \lambda_1 e^{\lambda_1 x} A_1 + \left(1 + \frac{\lambda_2}{\bar{P}_{eff}}\right) \lambda_2 e^{\lambda_2 x} A_2 + \left(1 + \frac{\lambda_3}{\bar{P}_{eff}}\right) \lambda_3 e^{\lambda_3 x} A_3 \quad (4.49)$$

The variation is similar to that of shear stress (maximum at end and minimum at centre). Figure 4.15 (a) and (b) presents the parametric variation of bond properties (shear modulus and bond thickness) on the effective strain at 91 kHz. The variation of strain for different values of shear modulus and bond thickness follow similar trend as that of shear stress (see Figure 4.12 and 4.11(b)). The overall observations are similar to the previous section. Figure 4.16 presents the variation of strain for different values of the inertia parameter at 91kHz section. The strain value increases with increasing of $\bar{\alpha}$ and the distribution becomes more uniform. Hence, the value inertia parameter should as high as possible.

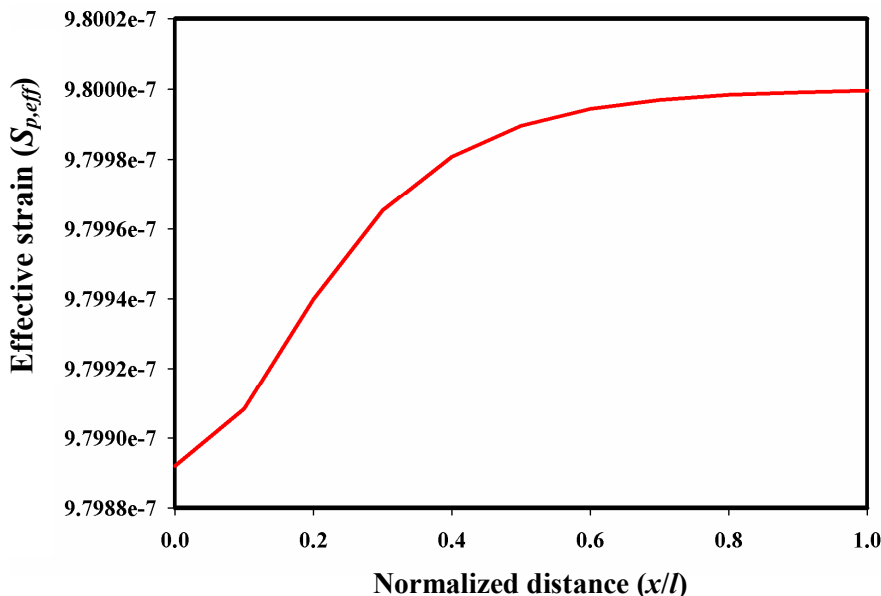


Figure 4.14 Profile of effective strain ($S_{p,eff}$) over the length of PZT

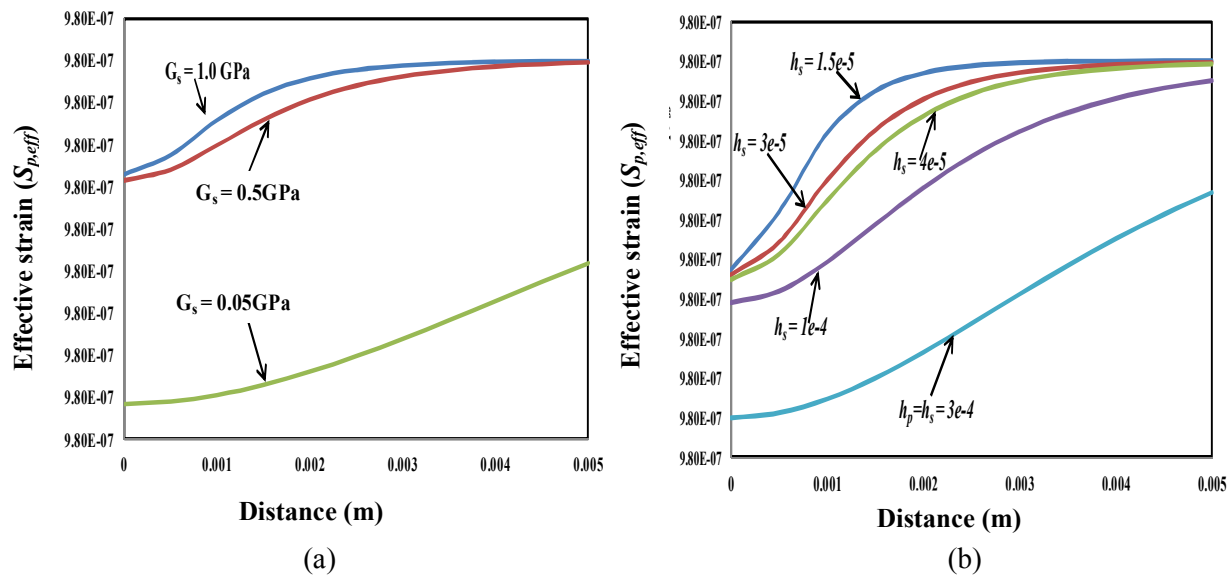


Figure 4.15 Profile of interfacial effective strain distribution

- (a) Effect of shear modulus of bond layer
- (b) Effect of bond layer thickness

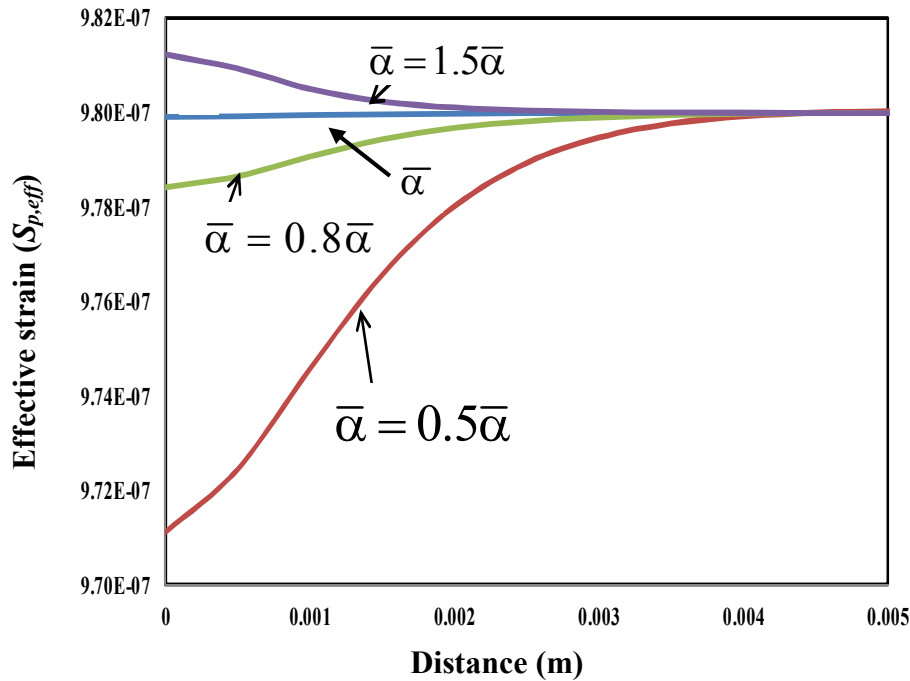


Figure 4.16 Effect of inertia parameter $\bar{\alpha}$ on effective strain

4.6.3 Variation of Effective Axial Stress along Adhesive Bond

The axial stresses along the two principal directions in the PZT patch can be expressed as

$$T_1 = \frac{\overline{Y^E}}{(1-\nu^2)} \left[(u'_{px} + \nu u'_{py}) - \Lambda(1+\nu) \right] \quad (4.50)$$

$$T_2 = \frac{\overline{Y^E}}{(1-\nu^2)} \left[(u'_{py} + \nu u'_{px}) - \Lambda(1+\nu) \right] \quad (4.51)$$

Adding Equation (4.46) and (4.47) and dividing by 2, we get

$$T_{eff} = \frac{(T_1 + T_2)}{2} = \frac{\overline{Y^E}}{(1-\nu)} \left[u'_{p,eff} - \Lambda \right] \quad (4.52)$$

Figure 4.17 shows a plot of T_{eff} as a function of distance for the PZT-adhesive-aluminium block system at a frequency of 91 kHz. From this figure, it can be noted that the effective axial stress is maximum at the centre of the patch and reduces to zero at the ends. The area under the curve normalized with respect to $T_{eff}l$ will result in a parameter similar to the effective length ratio defined by Sirohi and Chopra (2000) for the sensor case. In the present analysis, however, both sensor and actuator effects have been simultaneously considered.

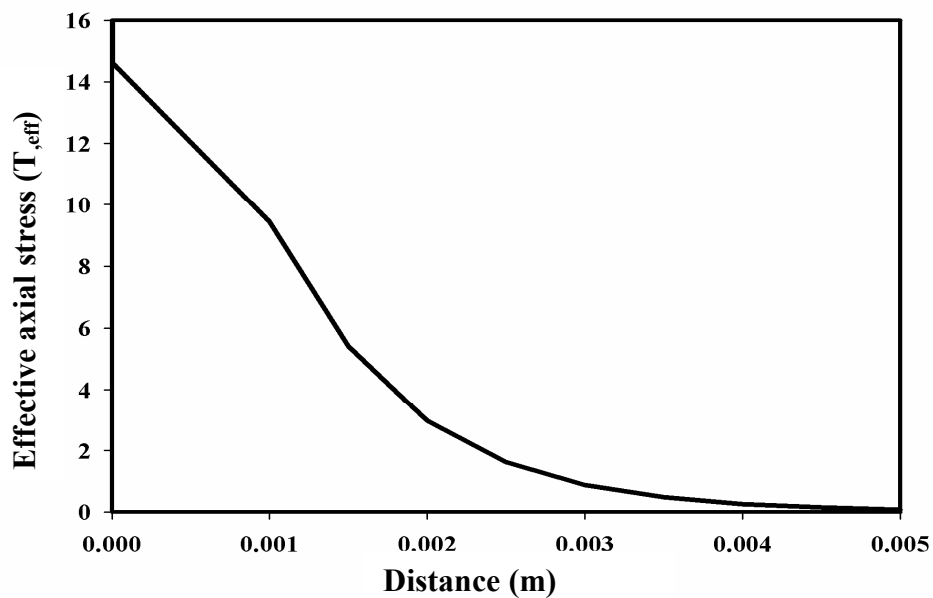


Figure 4.17 Variation of effective stress (T_{eff}) over the length of PZT patch

4.7 PARAMETRIC STUDY ON ADHESIVE BOND LAYER INDUCED ADMITTANCE SIGNATURES

This section studies the influence of various physical parameters on G and B with the aid of the new refined model presented in this chapter. The various factors affecting shear lag are shear modulus of bond layer (\overline{G}_s), thickness of adhesive layer (or the ratio h_s/h_p) and sensor length (l). The influence of all these parameters is studied in depth using the 2D shear lag based effective impedance formulations. The PZT parameters and mechanical properties of both host structure and adhesive are considered as listed in Table 4.1. For the bond layer, the thickness is chosen as 0.125mm for this study. The frequency range is limited to 0-250kHz, since for most of the civil engineering applications a sub range within 0-250kHz is adequate (Soh et al., 2000). Again, for simplicity, the inertia of the adhesive is ignored for following parametric studies.

4.7.1 Effect of bond layer Shear Modulus

Figure 4.18 shows the influence of the bond layer's shear modulus of elasticity ($\overline{G}_s = 1, 0.5$ and 0.05GPa) on the conductance and susceptance plots. It is observed that as \overline{G}_s decreases, the peaks of both G and B subside down, and the overall slope of B decreases. The worst results are observed for $\overline{G}_s = 0.05 \text{ GPa}$, for which the PZT patch behaves as independent from the host structure, as marked by a peak at its own resonance frequency, rather than identifying the host structure. From these observations, it is recommended that for best structural identification, an adhesive with high shear modulus is preferable for bonding the PZT patch with the structure.

4.7.2 Effect of bond layer thickness

Fig. 4.19 shows the plots of conductance and susceptance corresponding to $h_s = 0.05\text{mm}$ (thickness ratio, $h_s/h_p = 0.17$) and 0.1mm (thickness ratio, $h_s/h_p = 0.33$). It is apparent that as

bond layer thickness increases, the peaks subside down and shift rightwards. In addition, the average slope of the susceptance curve falls down. Hence, the overall effect is similar to that of reducing \bar{G}_s . Exceptionally thick bond layer (thickness ratio > 1.0) may lead to highly erroneous structural identification, as illustrated in the preceding section for \bar{G}_s . Hence, it is recommended that the bond layer thickness be maintained minimum possible.

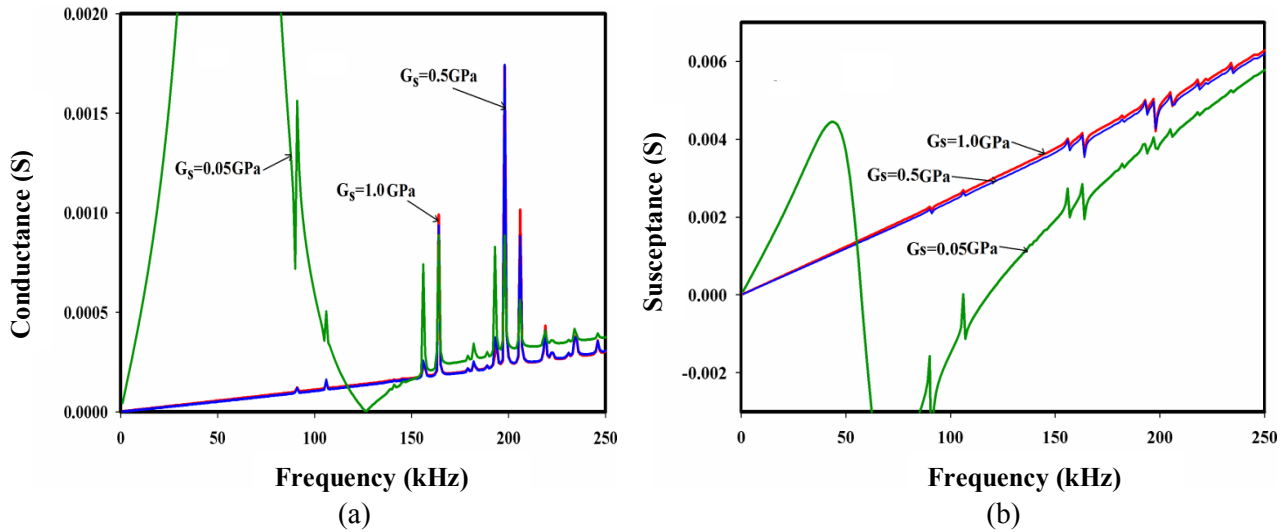


Figure 4.18 Influence of shear modulus of bond layer on EMI signature

- (a) Conductance (G) vs Frequency
- (b) Susceptance (B) vs Frequency

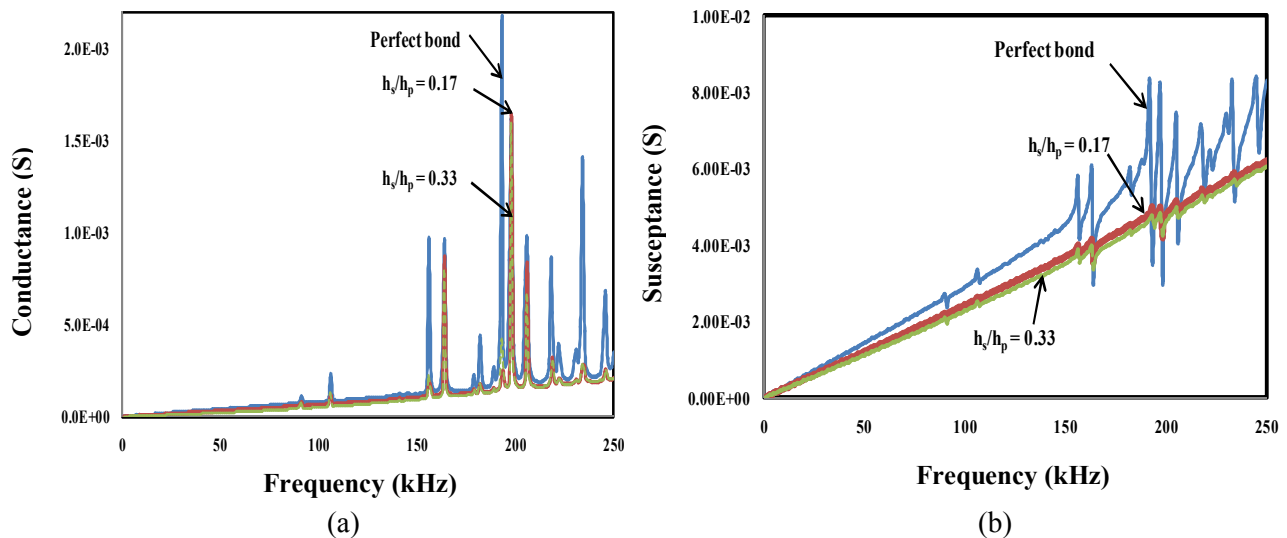


Figure 4.19 Influence of bond thickness on EMI signature

- (a) Conductance (G) vs Frequency
- (b) Susceptance (B) vs Frequency

4.7.3 Influence of Damping of Bond Layer (η')

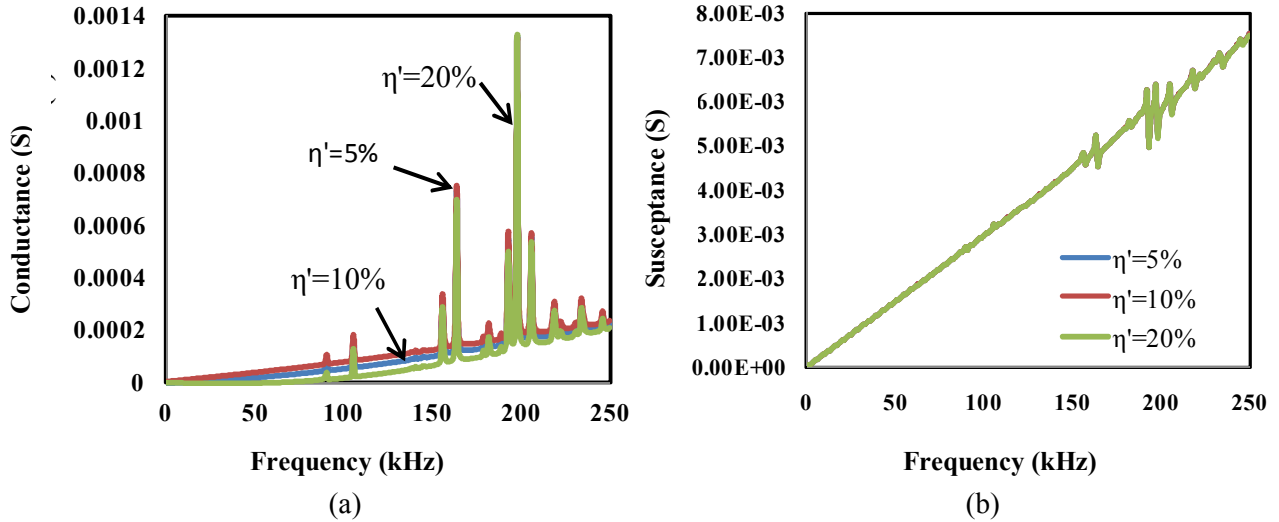


Figure 4.20 Influence of bond layer's damping on EMI signature

- (a) Conductance (G) vs Frequency
- (b) Susceptance (B) vs Frequency

Figure 4.20 shows the influence of the damping of the bonding layer on conductance and susceptance signatures. It is observed from Figure 4.20(a) that as the damping increases, the slope of the baseline conductance tends to fall down. However, susceptance, on the other hand, remains largely insensitive to damping variations, as can be observed from Figure 4.20(b).

4.7.4 Effect of sensor length

Figure 4.21 shows the influence sensor length on G and B . For the purpose of comparison, normalized values (G/l^2) and (B/l^2) have been plotted. It is observed that for small sensor length ($l = 5\text{mm}$), the signatures are closer to those for perfect bonding condition. However, the quality of signatures degrades for longer PZT patches ($l = 10\text{mm}$). Hence, smaller patches should be preferred over longer ones. This observation is also similar to the previous study (Bhalla and Soh, 2004c).

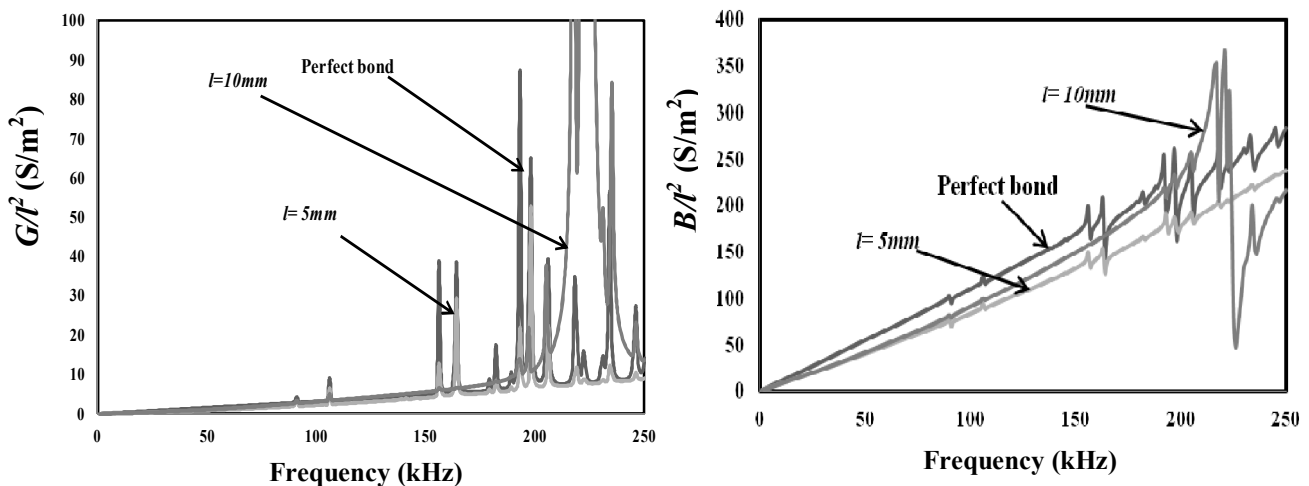


Figure 4.21 Influence of sensor length on EMI signature

- (a) Normalized Conductance
- (b) Normalized Susceptance

4.7.5 Effect of excitation voltage

Figure 4.22 depicts the influence of excitation voltage on G and B as per the present shear lag model. Electric potential has very negligible effect on the signature, as is clearly depicted from the plots. For experimental and analytical studies in the preceding sections, the applied voltage is kept 1Vrms, studies in preceding section, which is recommended for EMI technique (Sun et al., 1995; Park et al., 2000a, b). In fact, Sun et al. (1995) reported that higher excitation voltage has no influence on the conductance signature, but might only be helpful in amplifying weak structural modes. Hence, for the EMI technique, the small excitation voltage is adequate (less than 1V). In refined model, the electric field is directly accounted in the free PZT strain $\Lambda = d_{31}E_3$ (see equation 4.33). From this analysis, it can be concluded that, the effect is not significant.

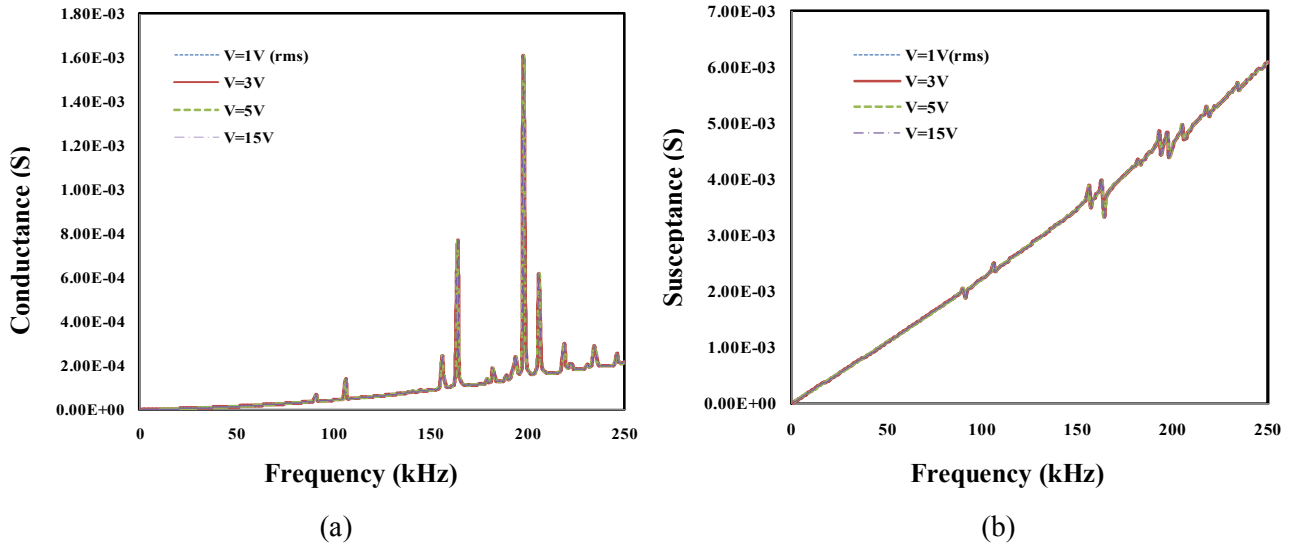


Figure 4.22 Influence of electric voltage on EMI signature

(a) Conductance (G) vs Frequency

(b) Susceptance (B) vs Frequency

4.8 CONCLUDING REMARKS

This chapter has provided a rigorously refined new analytical model for considering shear lag effect in the EMI formulations. The treatment is complete in the sense that the model includes the inertial as well as the shear stress term simultaneously, a feature missing in the previous models. The results show that it is important to consider the inertia effect which has significant influence on the signatures, especially in terms of lowering the peak values and the overall slope of conductance and susceptance. The effect of inclusion of the mass of adhesive has also been investigated. The results show that the mass of the adhesive plays only a negligible role and can be neglected. The distribution of shear stress and effective strain in the bond layer and the variation of axial stresses in the PZT patch have also been investigated for this paper. Finally, a parametric study has also been conducted to study the influence of different bond parameters on conductance and susceptance signatures.

Chapter-5

EXTENSION TO CONTINUUM BASED SHEAR LAG MODEL

5.1 INTRODUCTION

The previous chapter covered the derivation of a refined shear lag model incorporating both shear lag and inertia terms simultaneously. The effectiveness of the strain transfer from structure to PZT patch, highly depends on the stress (and strain) distribution along the bond layer with due consideration of all piezo-mechanical properties. The analytical derivation of continuum based shear lag model covered in this chapter aims to provide an improved and more accurate model for shear interaction between the host structure and the PZT patch through the adhesive bond layer taken care of all the piezo, structural and adhesive (shear lag) actions not only simultaneously but also in a continuous manner throughout the bond layer. Further, it eliminates the hassle of determining the equivalent structural impedance and actuator impedance separately, as required in the previous models, which involved the approximation of functional and mechanical impedance of the host structure.

In practical applications where the strains are a source for control, the term "Actuation Strain" refers to the strain other than that caused by stresses, such as thermal, magnetic or piezoelectric effects. Thus, the actuation strain is the term $\Lambda = d_{31}E_3$. For an unconstrained, unstressed piezoelectric material, the induced strain would be the same as actuation strain. However, if the piezoelectric material is constrained, being embedded or bonded with another material, then the actuation strain is clearly different from the induced strain. The induced strain is influenced by the actuation strain and it is determined by the coupling term at electro-mechanical interaction.

Hence, an accurate calculation of the actuation strain duly considering the adhesive effect along and throughout the total bond area will achieve the more accurate coupled admittance signature.

Although the refined model is an improvement over the previous model, the equivalent structural impedance ($Z_{s,eq}$), is computed at ($x=l$) only (see Equation 4.36). The equivalent impedance values are thus determined by making approximate deduction from true structural impedance for modelling strain transfer phenomena between the patch and the structure. In order to rigorously consider shear transfer phenomena through the adhesive layer, one needs to integrate all terms continuously and simultaneously throughout the bond area. This is the main objective addressed in this chapter, discussed in the forthcoming sections.

5.2 DERIVATION OF ADMITTANCE SIGNATURE USING CONTINUUM APPROACH

The electric displacement D_3 over the surface of a PZT patch can be determined from the basic equation governing piezoelectric direct effect (Equations 2.1(a), (b)). For 2D case, the piezoelectric constitutive equations can be reduced to (Bhalla and Soh, 2004a)

$$D_3 = \overline{\epsilon_{33}^T} E_3 + d_{31} (T_1 + T_2) \quad (5.1)$$

$$S_1 = \left(\frac{T_1 - \nu T_2}{\overline{Y^E}} \right) + d_{31} E_3 \quad (5.2)$$

$$S_2 = \left(\frac{T_2 - \nu T_1}{\overline{Y^E}} \right) + d_{31} E_3 \quad (5.3)$$

where ν is the Poisson's ratio of the patch and T_1 , T_2 and S_1 , S_2 are the principal components of stress and strain tensor respectively.

From Equations (5.2) and (5.3), we get

$$T_1 + T_2 = \frac{\overline{Y^E}}{(1-\nu)} (S_1 + S_2 - 2d_{31}E_3) \quad (5.4)$$

Substituting the Equation (5.4) into (5.1) and with $E_3 = \left(\frac{V_0}{h} \right) e^{j\omega t}$ (where V_0 represents the peak sinusoidal voltage), the equation can be further reduced to

$$D_3 = \overline{\varepsilon_{33}^T} \frac{V_0}{h} e^{j\omega t} + d_{31} \frac{\overline{Y^E}}{(1-\nu)} \left(S_1 + S_2 - 2d_{31} \frac{V_0}{h} e^{j\omega t} \right) \quad (5.5)$$

The current flowing through the circuit can be determined as

$$\bar{I} = \iint_A \dot{D}_3 dx dy = j\omega \iint_A D_3 dx dy \quad (5.6)$$

Substituting the Equation (5.5) in to the Equation (5.6), the equation can be re-written as (integrating from $x=l$ to $x=-l$)

$$\bar{I} = j\omega \iint_A \overline{\varepsilon_{33}^T} \frac{V_0}{h} e^{j\omega t} dx dy + j\omega \iint_A d_{31} \frac{\overline{Y^E}}{(1-\nu)} \left(S_1 + S_2 - 2d_{31} \frac{V_0}{h} e^{j\omega t} \right) dx dy \quad (5.7)$$

Substituting $\bar{V} = V_0 e^{j\omega t}$ (\bar{V} represents the instantaneous voltage across the PZT patch), and solving the equation, it can be reduced to

$$\bar{I} = 4j\omega \bar{V} \frac{l^2}{h} \left[\overline{\varepsilon_{33}^T} - \frac{2d_{31}^2 \overline{Y^E}}{(1-\nu)} \right] + j\omega d_{31} \frac{\overline{Y^E}}{(1-\nu)} \iint_A (S_1 + S_2) dx dy \quad (5.8)$$

where S_1 and S_2 are the strains in the PZT patch along both x and y directions respectively. They can be obtained from the expressions for displacements (Equation 4.15 and 4.16) as

$$S_1 = -u'_{px} = \left(1 + \frac{\lambda_1}{\bar{P}_{eff}} \right) \lambda_1 e^{\lambda_1 x} A_1 + \left(1 + \frac{\lambda_2}{\bar{P}_{eff}} \right) \lambda_2 e^{\lambda_2 x} A_2 + \left(1 + \frac{\lambda_3}{\bar{P}_{eff}} \right) \lambda_3 e^{\lambda_3 x} A_3 \quad (5.9)$$

$$S_2 = -u'_{py} = \left(1 + \frac{\lambda_1}{\bar{P}_{eff}} \right) \lambda_1 e^{\lambda_1 y} A_1 + \left(1 + \frac{\lambda_2}{\bar{P}_{eff}} \right) \lambda_2 e^{\lambda_2 y} A_2 + \left(1 + \frac{\lambda_3}{\bar{P}_{eff}} \right) \lambda_3 e^{\lambda_3 y} A_3 \quad (5.10)$$

The negative sign indicates that compressive strain is induced in the PZT patch on account of positive displacement at the patch tip. λ_1 , λ_2 and λ_3 are the three complex roots of the shear lag governing differential equation (Equation (4.13)) and A_1 , A_2 and A_3 are the three unknown coefficients of the solution, expressed as

$$u = A_1 e^{\lambda_1 x} + A_2 e^{\lambda_2 x} + A_3 e^{\lambda_3 x} \quad (5.11)$$

$\overline{p_{eff}}$ the shear lag parameter for 2D case, evaluated as (Bhalla and Soh, 2004c)

$$\overline{p_{eff}} = -\frac{2l\overline{G_s}(1+\nu)}{Z_{eff}j\omega h_s} \quad (5.12)$$

The co-efficients A_1 , A_2 and A_3 can be determined from the imposed boundary conditions, as explained in chapter 4. Using the expressions of S_1 and S_2 from Equations (5.9) and (5.10), the final complex electro-mechanical admittance spectra for full PZT patch can be formulated as

$$\overline{Y} = \frac{\overline{I}}{\overline{V}} \quad (5.13)$$

which, after simplifying yields the final expression for \overline{Y} as

$$\overline{Y} = 4j\omega \frac{l^2}{h_p} \left[\overline{\varepsilon_{33}^T} - \frac{2d_{31}^2 \overline{Y^E}}{(1-\nu)} \right] - \frac{8lj\omega d_{31} \overline{Y^E}}{(1-\nu)\overline{V}} \left[\left(1 + \frac{\lambda_1}{\overline{p}_{eff}} \right) \lambda_1 (e^{\lambda_1 l} - 1) A_1 + \left(1 + \frac{\lambda_2}{\overline{p}_{eff}} \right) \lambda_2 (e^{\lambda_2 l} - 1) A_2 + \left(1 + \frac{\lambda_3}{\overline{p}_{eff}} \right) \lambda_3 (e^{\lambda_3 l} - 1) A_3 \right] \quad (5.14)$$

In compact form, the new coupled admittance signature can thus be expressed as

$$\overline{Y} = \frac{\overline{I}}{\overline{V}} = 4j\omega \frac{l^2}{h_p} \left[\overline{\varepsilon_{33}^T} - \frac{2d_{31}^2 \overline{Y^E}}{(1-\nu)} \right] - \frac{8lj\omega d_{31} \overline{Y^E}}{(1-\nu)\overline{V}} [U_{con}] \quad (5.15)$$

where U_{con} is the continuum displacement generated at the interfacial bond layer after accounting the shear lag effect in the continuous manner as derived above. The main advantage of the new model is that it eliminates the equivalent structural impedance terms of the previous models, which was simply an approximation (see equation (4.36)). In the present approach, the

admittance \bar{Y} is determined by continuous integration taking account of variation of stresses and strains along the PZT patch, rather than at the periphery of the patch. Since u and u_p were just considered at ends of the patch in previous models, they did not carry complete information behind the force transfer mechanism occurring along the adhesive bond. On the other hand the term U_{con} takes care of the strain generated at interfacial bond due to PZT patch deformation in a continuous manner. This makes the current shear lag model more accurate and realistic. A MATLAB code enlisted in appendix C for the simulation of continuum signature.

5.3 EXPERIMENTAL VERIFICATION

The admittance signature (\bar{Y}) derived in the previous section was verified based on the experimental results of Bhalla and Soh (2004a, b). The experimental set up is described in chapter 4. All piezo-mechanical properties remain the same. A bond thickness ($h_s = 0.125\text{mm}$) was chosen for the analytical and experimental signatures. After performing harmonic analysis, the resultant admittance signature was determined using Equation (5.15).

Figures (5.1) and (5.2) compare the analytical and experimental conductance and susceptance signatures respectively for two different bond thickness ratio ($h_s/h_p = 0.417$) and ($h_s/h_p = 0.834$). Figure (5.3) and (5.4) respectively compare the conductance and susceptance signature resulting from the continuum approach with those from the refined model of chapter 4. It can be observed that, the continuum signatures are match better to the experimental plots as compared to refined model. For the susceptance, the influence of bond is significantly highlighted by lowering the slope (see Figure 5.2 and 5.4), which is not highlighted in refined model (for experimental case) similar observation hold good for conductance (Figure 5.1 and 5.3). The accuracy and efficiency of bonding effect on piezo-elastodynamic model has been increased significantly through

continuum based approach due to more effective quantification shear parameter throughout the bond area, which is lacking in refined shear lag model.

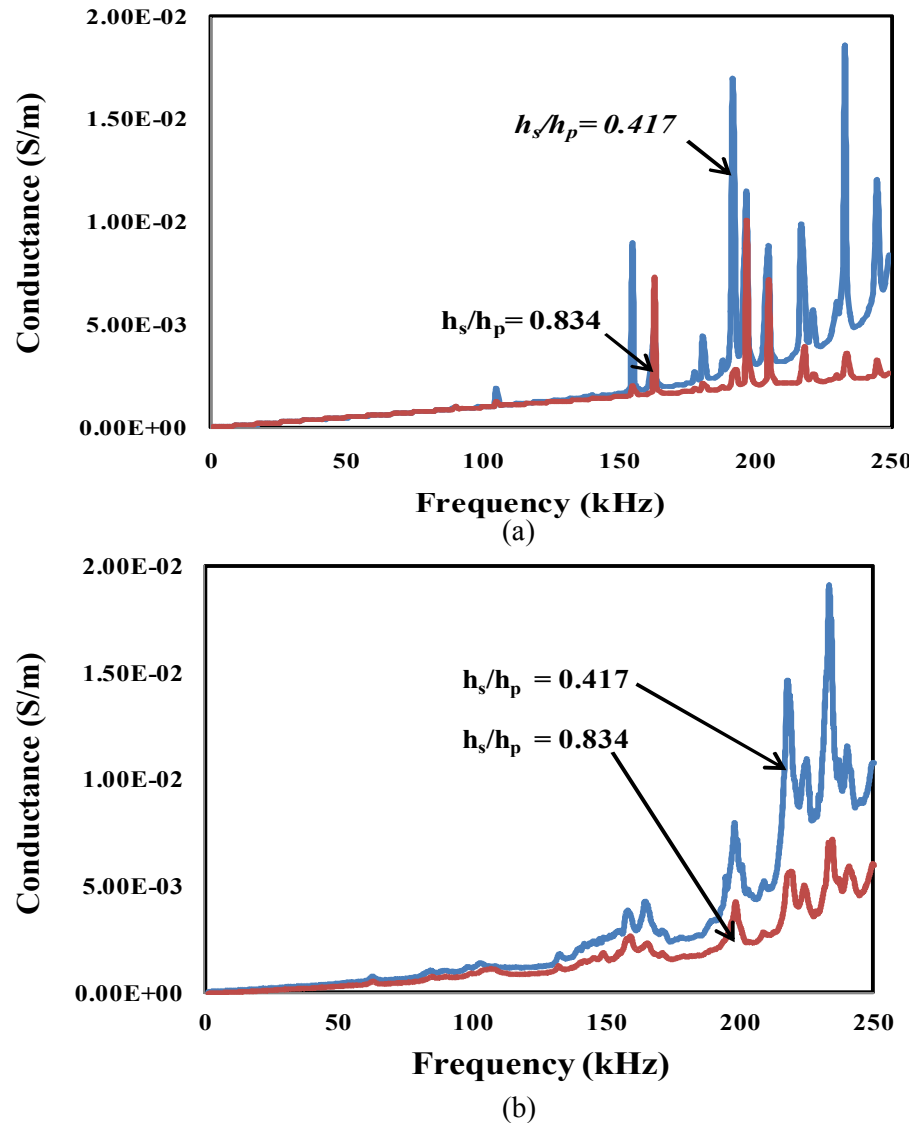


Figure 5.1 Comparison of conductance of experimental result with continuum shear lag model

(a) Normalized analytical conductance (continuum model) for $h_s/h_p=0.417$ and $h_s/h_p=0.834$

(b) Normalized experimental conductance for $h_s/h_p=0.417$ and $h_s/h_p=0.834$

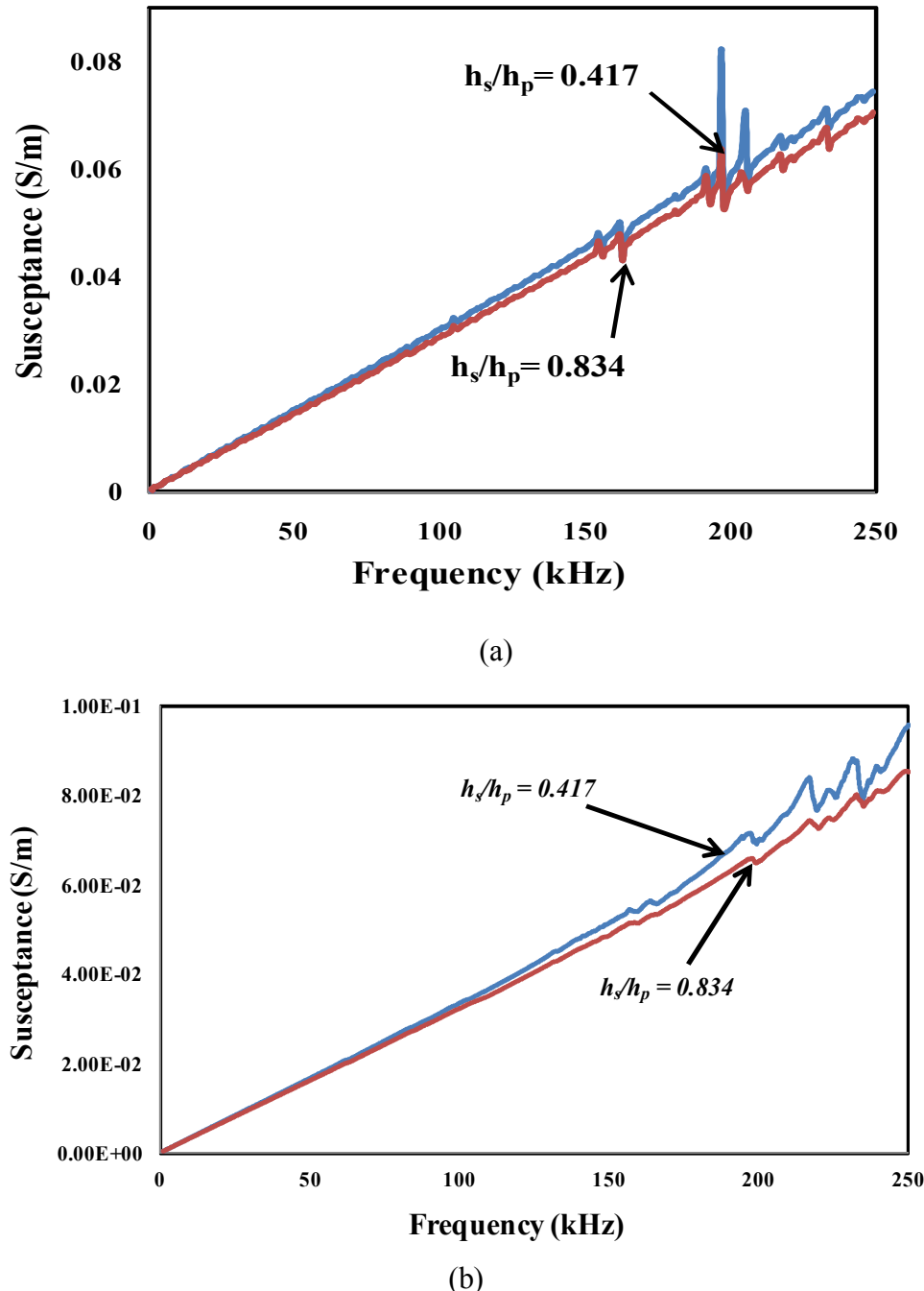
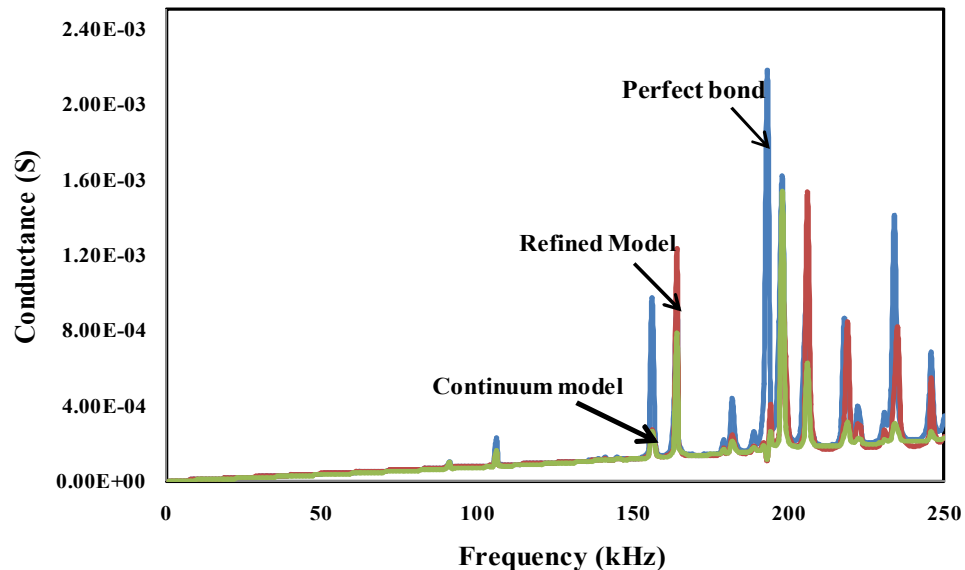
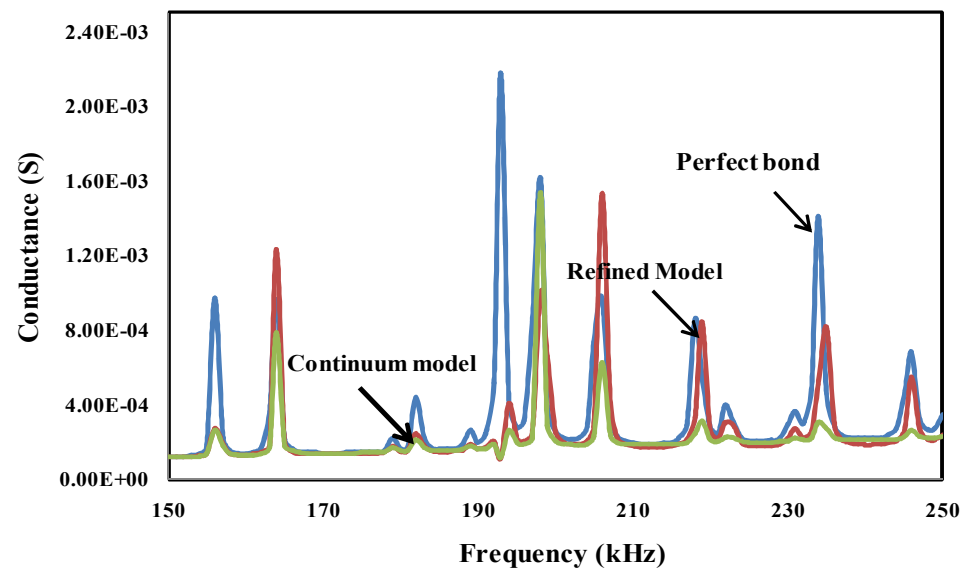


Figure 5.2 Comparison of susceptance of experimental result with continuum shear lag model

- (a) Normalized analytical susceptance (continuum model) for $h_s/h_p=0.417$ and $h_s/h_p=0.834$
- (b) Normalized experimental susceptance for $h_s/h_p=0.417$ and $h_s/h_p=0.834$



(a)

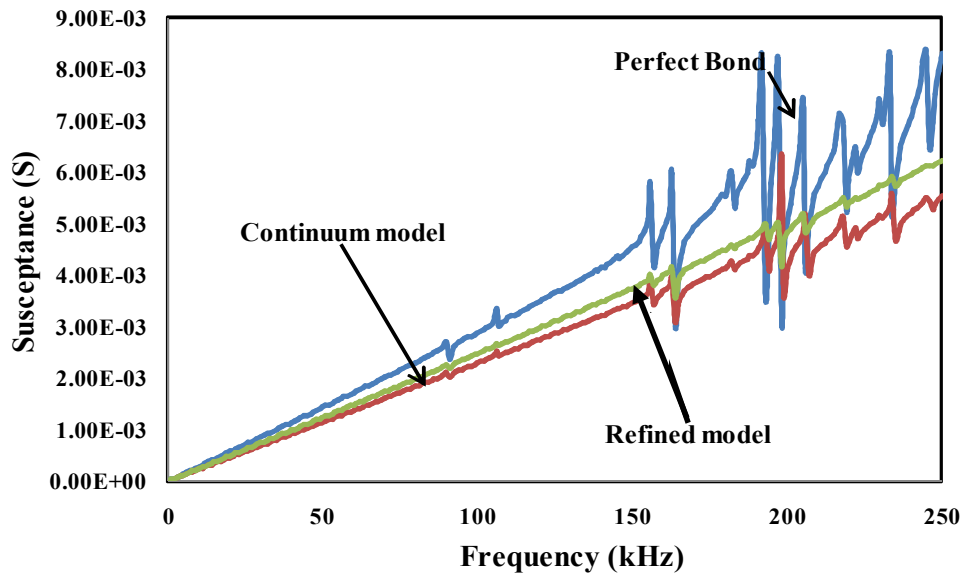


(b)

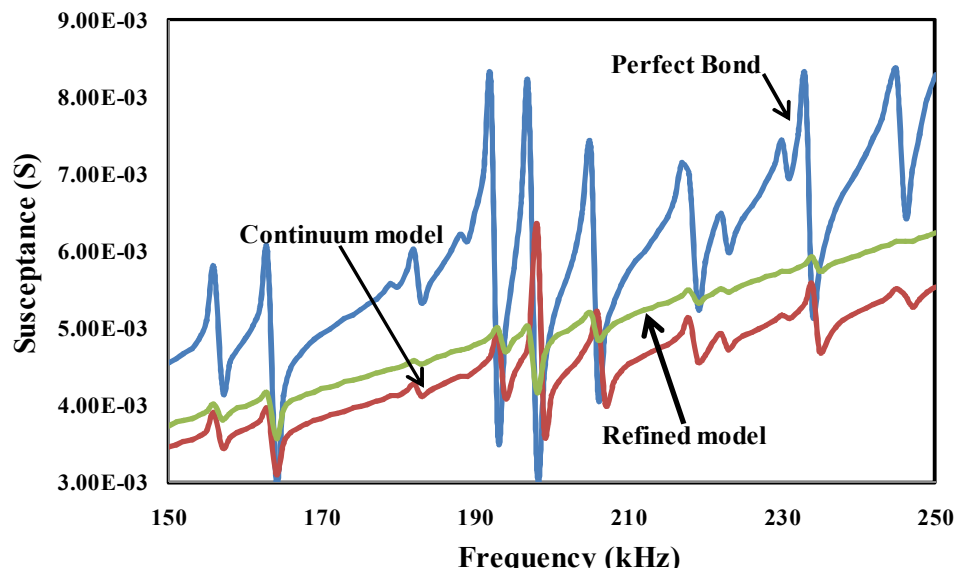
Figure 5.3 Comparison of conductance (G) plot

(a) Plot over (0-250) kHz

(b) Closer view (150-250) kHz



(a)



(b)

Figure 5.4 Comparison of susceptance (B) plot

(a) Plot over (0-250) kHz

(b) Closer view (150-250) kHz

5.4 PARAMETRIC STUDY FOR CONTINUUM SIGNATURE

Figure (5.5) shows the effect of the mechanical loss factor η' with two extreme variations (80% and 150%) on conductance and susceptance signatures obtained using the continuum model. The effect of damping of the bond layer has negligible effect on overall signature, as clearly apparent from the Figure.

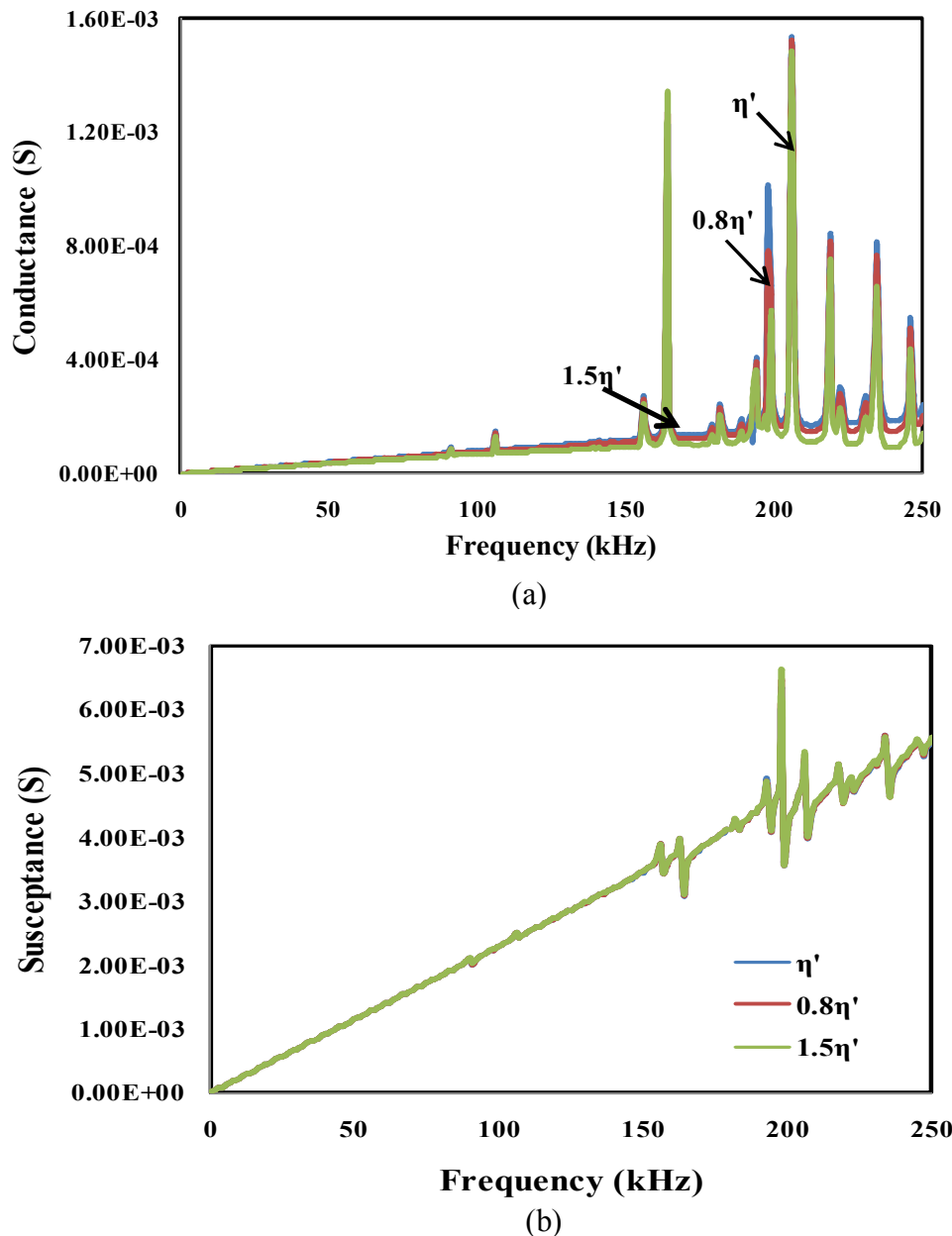


Figure 5.5 Effect of mechanical loss of bond layer on new proposed admittance function

(a) Conductance vs Frequency

(b) Susceptance vs Frequency

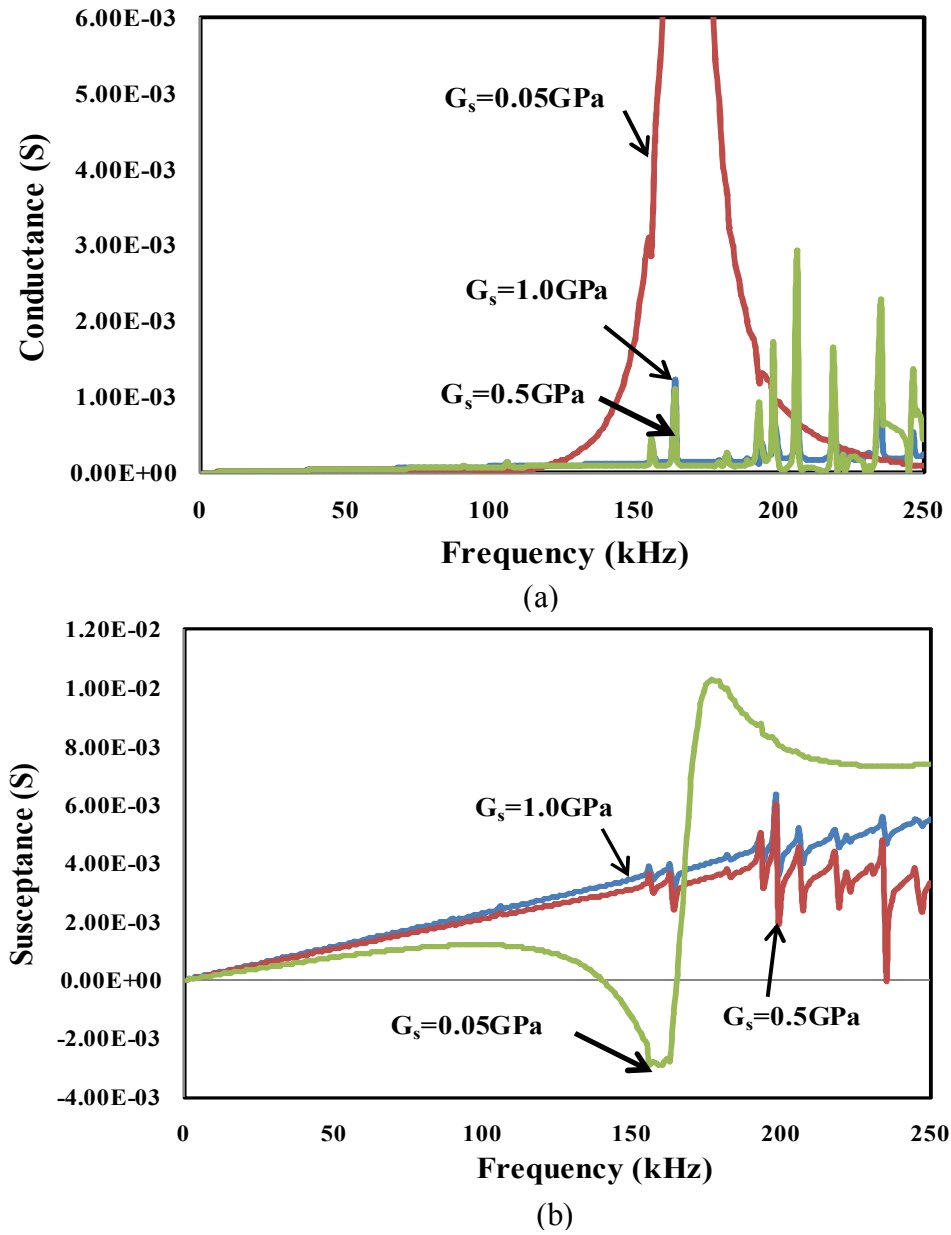


Figure 5.6 Effect of shear modulus of bond layer on new proposed admittance function

(a) Conductance vs Frequency

(b) Susceptance vs Frequency

Figure 5.6 shows the influence of shear modulus of bond layer on continuum signature. It can be observed that, the effect is similar to that observed for the refined model (Chapter-4). Similarly, the effect of dielectric loss factor δ on the admittance signature is shown in Figure (5.7) with same range of variation (80% and 150%). The effect of the dielectric loss for proposed is

significant for conductance but negligible for susceptance. It can be stated that compared to η , δ has significant effect on the conductance signature.

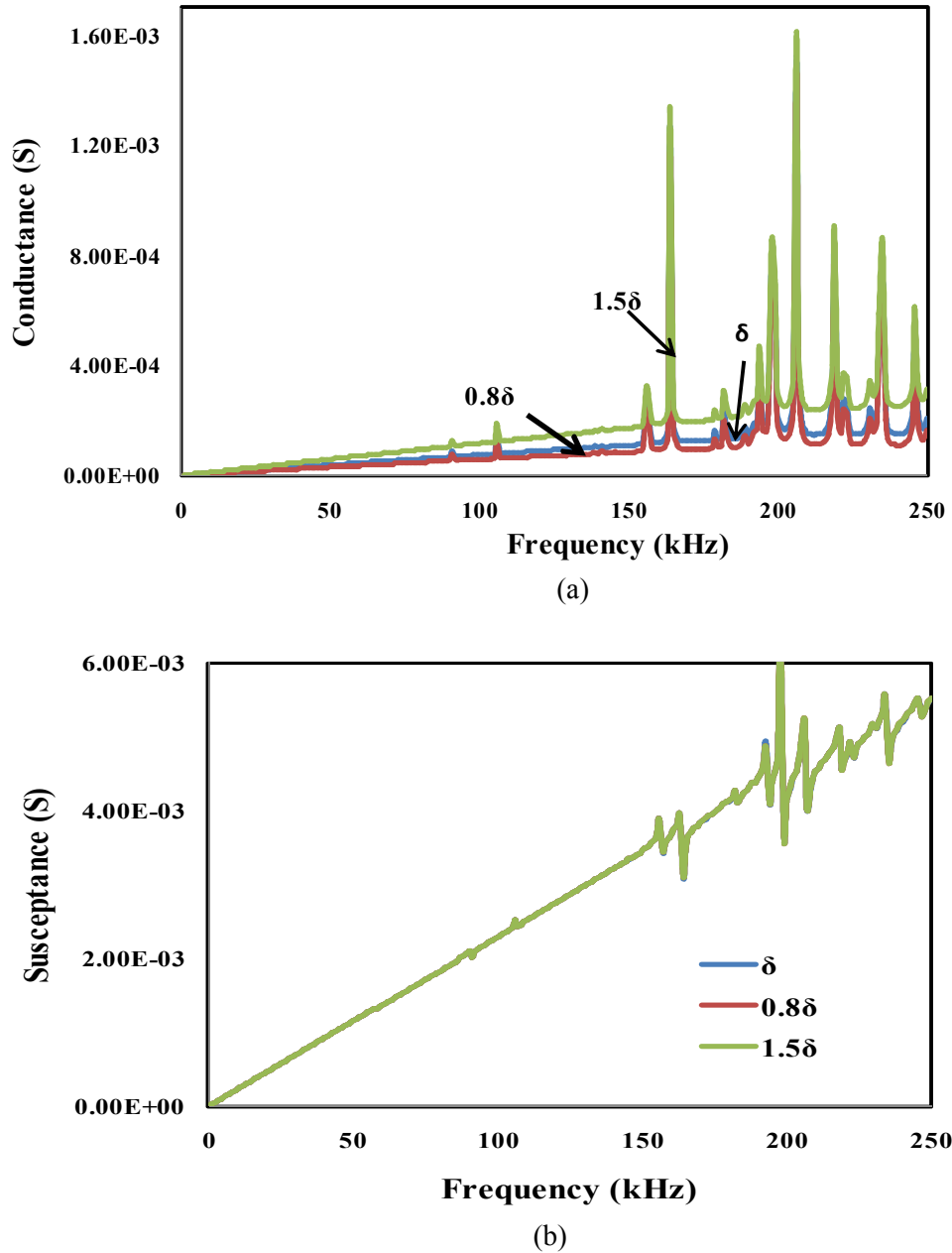


Figure 5.7 Effect of dielectric loss on new proposed admittance function

- (a) Conductance vs Frequency
- (b) Susceptance vs Frequency

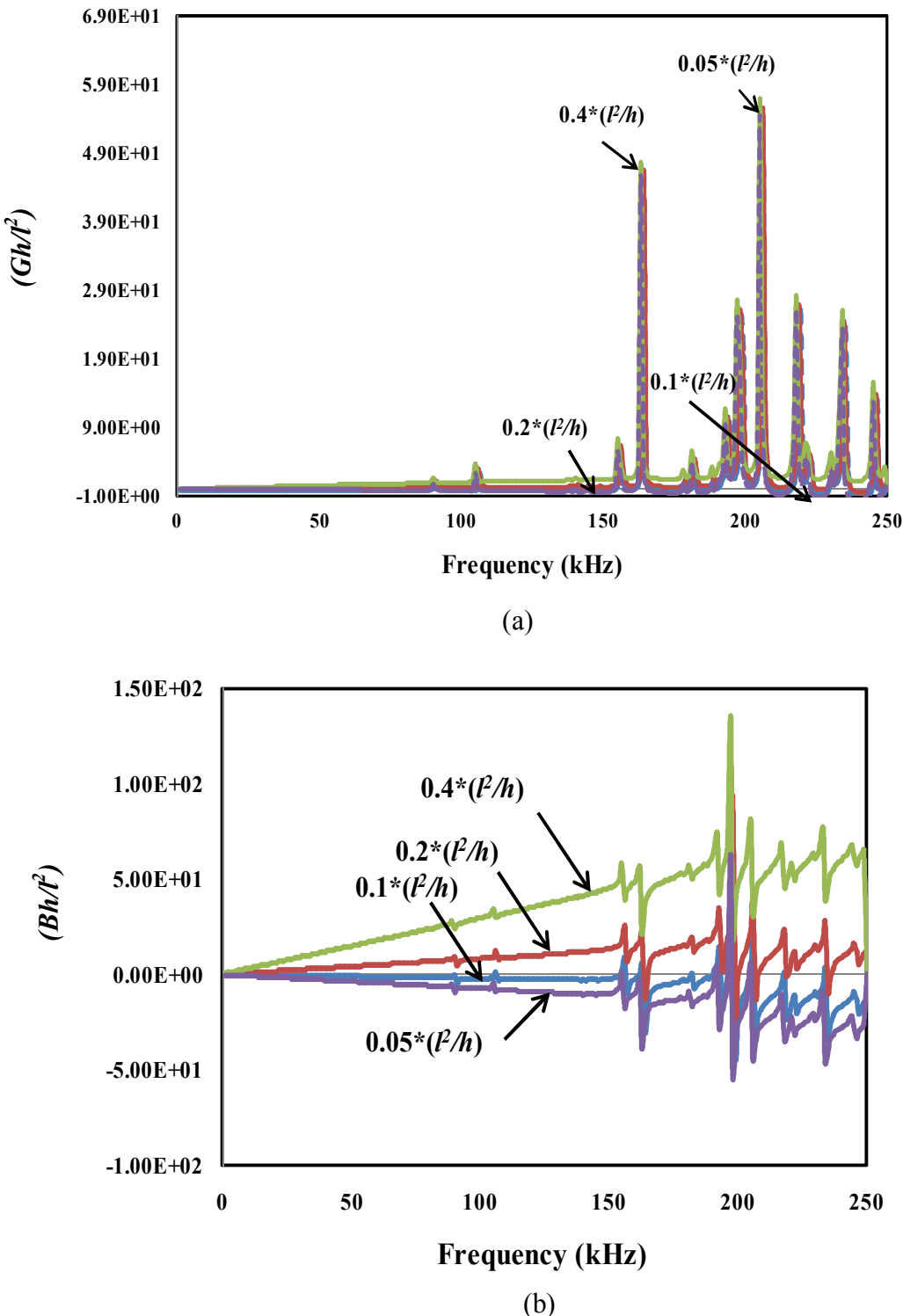


Figure 5.8 Effect of dimension change (l^2/h) on new proposed admittance function

(a) Normalized conductance vs Frequency

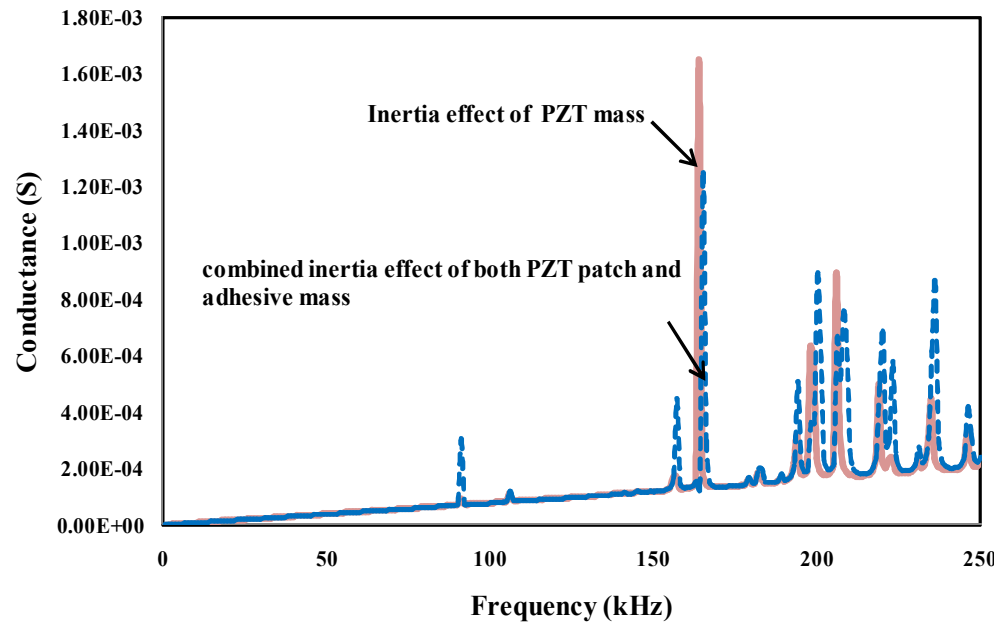
(b) Normalized susceptance vs Frequency

The dimensional ratio (l^2/h) has observable effect on normalized conductance (Gh/l^2) and normalized susceptance (Bh/l^2), evident from Figure (5.8). Hence, The PZT patch's dimension has significantly affect the admittance of piezo elastic model.

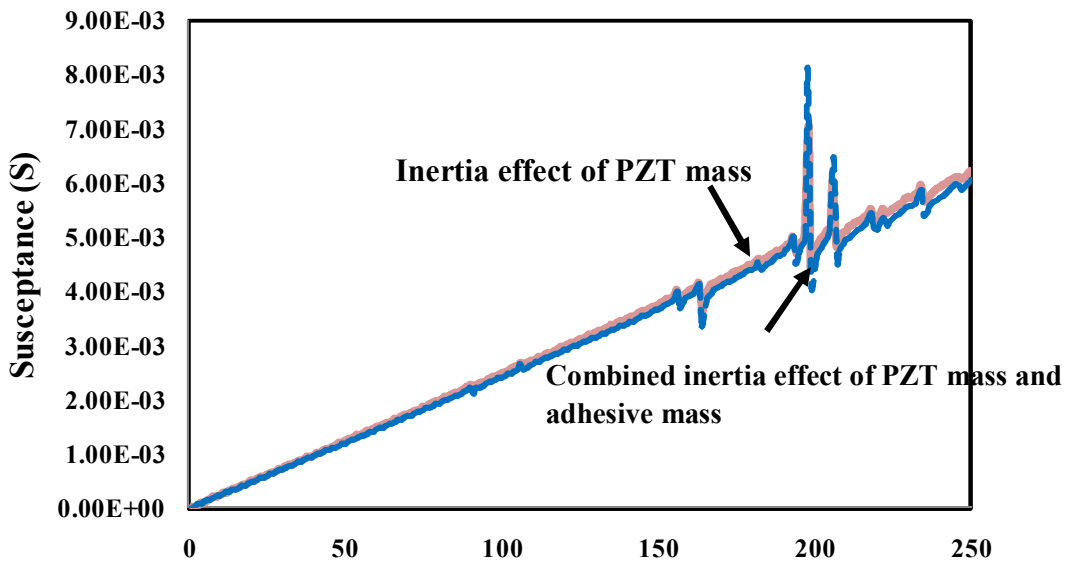
From this study, it can be concluded that for better electro-mechanical coupled interaction, sensor length and bond thickness should kept to minimum possible and $\overline{G_s}$ should have highest possible value.

5.5 EFFECT OF ADHESIVE MASS

The combined effect of the inertia of both the adhesive and the PZT patch on the continuum based EMI admittance spectra is investigated in this section. For this purpose, Equation (4.47) is utilized to obtain $u_{p,eff}$ (hence, strain u'_{px} and u'_{py}), thus integrated Equation (5.15), to obtain U_{con} , which ultimately yield more precise and accurate coupled admittance signature for this cumulative inertia effect of both the adhesive and PZT mass based on continuum approach. Figure 5.9 (a) and (b) show the overall effect on the admittance signature. As compared to the refined model, the effect of mass of adhesive is marginal in susceptance (see Figures 4.9(b) and 5.9(b)). As far as conductance is concerned, the continuum approach predicts are greater effect of the mass of adhesive (see Figures 4.9(a) and 5.9(a)), in terms of shifting of peaks of conductance in addition to magnitude. However, the overall effect can be considered to be negligible



(a)



(b)

Figure 5.9 Effect of combined mass (PZT and adhesive) effect on admittance signature

(a) Conductance Vs. Frequency

(b) Susceptance Vs Frequency

5.6 CONCLUDING REMARKS

This chapter has rederived the coupled admittance signature based on the continuous variation of displacement (hence, the related piezo induced strain) and charges over the PZT patch. This is more accurate and more realistic shear lag model for the impedance based SHM for EMI technique. A new continuum strain term (U_{con}) has been introduced to consider the continuous variation of parameters (bond and piezo through the bond layer). It is more convenient and practicable in real life applications because it eliminates all the approximations associated with previous models, which were based on equivalent impedance term without rigorous integration of all shear lag parameters (shear stress and inertia force) in a continuous manner. The continuum based signatures are closer to the new experimental plots. The effect of adhesive mass and PZT mass simultaneously has also been investigated, which shows negligible impact on overall performance. Parametric study has been carried out to analyse the effect of both mechanical and electrical properties on the proposed admittance spectrum. The continuum model represents a significant improvement over the refined model.

Chapter -6

BOND EFFECT ON POWER AND ENERGY TRANSEDUCTION EFFICIENCY

6.1 INTRODUCTION

This chapter deals with analysis of the power consumption in the PZT patch and its loss due to adhesive bonding with host structure. When a PZT patch is utilized as active impedance transducer in the EMI technique, the patch acts as both sensor and actuator (dual effect) for a range of frequency. For an efficient intelligent system, power consumption occurs in two forms. First part of the energy is used to actuate the PZT patch and produce deformation. The other part of the energy is dissipated within the piezo-mechanical system due to internal mechanical loss and heat generation. Hence, the determination of power consumption characteristic for active piezo system is very important for designing an efficient intelligent structure with optimized mass and energy combination. Adhesive bond itself acts as an added stiffness mass and damping element for mechanical response and plays an important role in mechanical and electrical energy conversion in the piezo-mechanical system. Hence, a detailed investigation is needed to characterize the power consumption and energy issues associated with bond layer driven PZT patch.

6.2 ELECTRICAL IMPEDANCE AND POWER TRIANGLE

The impedance term refer to electrical load, which acts opposite to work done, the combined effect of the resistance (R), inductive reactance (X_L) and capacitive reactance (X_C) in an AC circuit (shown in Figure 6.1(a)), under an alternating voltage source operating at a frequency f .

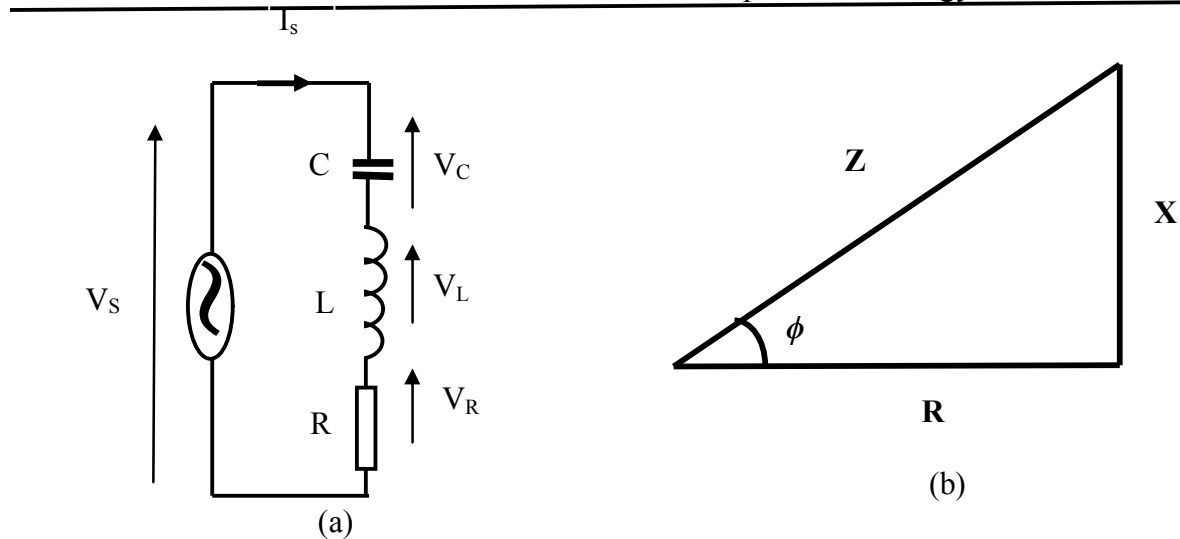


Figure 6.1

- (a) Series combination of LCR Circuit the inductance (L), the resistance (R), and the capacitance (C).
- (b) Impedance triangle for LCR circuit

The impedance triangle for an LCR circuit in series has shown in Figure 6.1(b) (Watkins and Kitcher, 2006). From Figure 6.2, the impedance (\bar{Z}_e) term for a complex plane (Figure 6.2(a)) can be defined as

$$\bar{Z}_e = R + Xj \quad (6.1)$$

Equation (6.1) can be rewritten in the form admittance as

$$\bar{Y} = G + Bj = \frac{1}{\bar{Z}_e} = \frac{1}{R + Xj} \quad (6.2)$$

On simplification of Equation (6.2), the conductance and susceptance can be expressed in terms of R and X as

$$G = \frac{R}{(R^2 + X^2)} \quad 6.3(a)$$

$$B = \frac{-X}{(R^2 + X^2)} \quad 6.3(b)$$

The phase angle between the voltage and current can be determined as

$$\tan \phi = \frac{X}{R} = \left(-\frac{B}{G} \right) \quad (6.4)$$

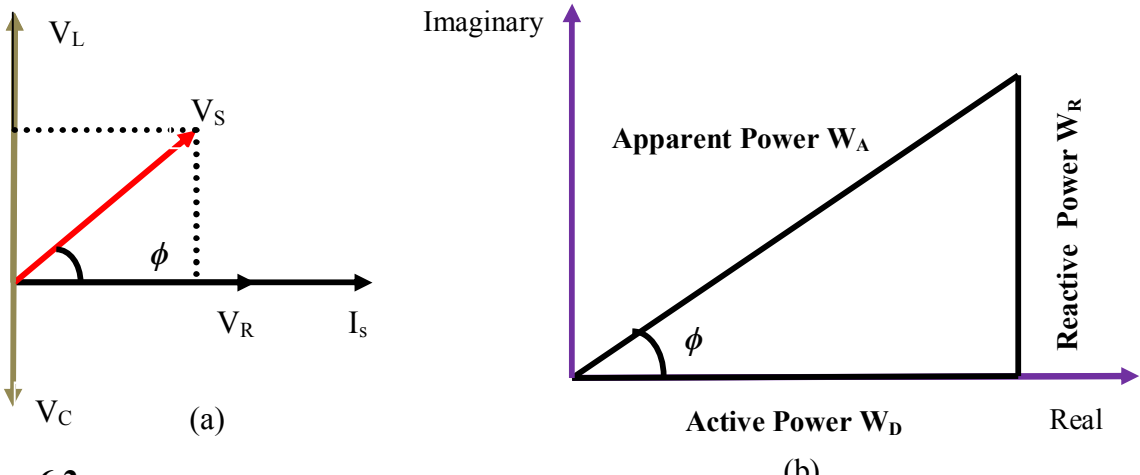


Figure 6.2

- (a) Vector representation of voltage and current on complex plane
- (b) Power triangle

The power factor of impedance circuit can be defined as

$$\cos \phi = \frac{R}{|Z|} = \frac{G}{|Y|} \quad (6.5)$$

The impedance and power triangles of impedance have are similar. We can thus conclude that:

$$\frac{W_D}{R} = \frac{W_R}{X} = \frac{W_A}{Z} \quad (6.6)$$

where W_D , W_A and W_R are the dissipative , reactive and apparent power component of a given impedance triangle.

The sign of angle ϕ must be accounted, for two of these cases

- 1) $\phi > 0 \Rightarrow W_R > 0 \text{ & } X > 0$ (inductive impedance)
- 2) $\phi < 0 \Rightarrow W_R < 0 \text{ & } X < 0$ (capacitive impedance)

6.3 POWER AND ENERGY FLOW IN PIEZO-MECHANICAL INTERACTION

In the EMI technique, the PZT patch couples the electrical and mechanical parameters simultaneously.

In the EMI technique, the PZT patch couples the electrical and mechanical parameters simultaneously. Integrated induced strain actuators provide the necessary energy for an intelligent system to respond adaptively to internal or external stimuli. The actuator power consumption as well as the energy transfer (from the actuator to the mechanical systems and vice versa), therefore, is an important issue in the application and design of intelligent material systems and structures. In the EMI technique, though actuation is part of the mechanical interaction, the forces involved are low. In either case, for a system with integrated PZT patches, the power consumed by the patches consists of two parts: the energy used to drive the system, which is dissipated in terms of heat (as a result of the structural damping), and energy dissipated by the PZT patches themselves because of their dielectric loss and internal damping.

The power consumption is related to the designated function of the piezo system, i.e., whether it is used for shape control, health monitoring, vibration, or acoustic control, as well as the associated electronic systems, including the power supply itself. In this section, we will not include the power supply system in the coupled electro-mechanical analysis by assuming that the power supply system can always satisfy the current needs of the actuator (Liang et al., 1994). In vibration control, the energy supplied to the PZT is absorbed by the structural damping in the mechanical system and the internal damping and dielectric loss of the PZT actuator. For acoustic control, most of the electrical and mechanical energy is used to radiate sound. In shape control, all the system energy is transferred from reactive electric energy into reactive mechanical energy (strain energy) but still stored in the electromechanical system. In SHM (EMI Technique), all the

electrical reactive energy is converted into the mechanical reactive energy and vice versa because of the dual piezoelectric effect. As a matter of fact, this issue was noticed during the early development and implementation of PZT actuators.

In the beginning, several static-based modelling techniques were developed to determine the equivalent static forces or moments (Bailey and Hubbard, 1985; Crawley and de Luis, 1987; Dirmittiadis et al., 1989; Wang and Rogers, 1991) as described in Chapter-2. An approximate dynamic analysis using the static models is not accurate because active forces provided by PZT actuators are usually harmonic in nature. The dynamic interaction between the host structure and the active elements exist and affects the performance of both the structure and the patch. Later on, the impedance-based analytical model developed by the Liang and others provided a better understanding of the dynamic characterization of PZT element-driven systems (Liang et al., 1994; Zhou et al., 1996; Bhalla and Soh, 2004a, b; Bhalla et al., 2009). The frequency-dependent force output behaviour is accurately predicted in the impedance model. The bonding effect on the electro-mechanical admittance output has been modelled by various researchers with numerous analytical models (Xu and Liu, 2002; Ong et al., 2002; Bhalla and Soh, 2004c; Ammandas and Soh, 2007a, b; Han et al., 2008; Dugnani, 2009; Bhalla et al., 2009; Huang et al., 2010; Tinoco et al., 2010; Yu et al., 2010; Giurgiutiu and Santoni, 2009) supplemented with experimental verification. They concluded that the bonding effect has significant impact on coupled admittance signature. Several numerical investigations on shear lag effect (Liu and Giurgiutiu, 2006, 2007; Yang et al., 2008, 2011; Jin and Wang, 2011; Zhang et al., 2011) have been reported to analyse the bonding effect.

The designers of the engineering and space structures are also concerned with how efficiently a PZT patch acts as a transducer to transforms the electrical energy into the mechanical energy.

Liang et al. (1996) studied triangular component of power to interpret the usage of the electro-mechanical properties of piezo transducer in various applications. They suggested actuator power factor, defined as the ratio of the dissipative mechanical power in the system to the total electrical power supplied to the actuator. This concept was used to optimize the location of the actuator (Liang et al., 1995). Stein et al. (1994) investigated the power consumption of a PZT actuator integrated with an underwater structure that radiated sound, and evaluated the power requirements in active acoustic control.

The influence of different dissipaters on the system power factor and the system power requirement was studied by Zhou et al. (1996) who extended the impedance model to 2D. Lin and Giurgiutiu (2012) developed a 1D guided axial and flexural wave based predictive model for power and energy transduction between structurally guided waves and piezo wafer active sensor (PWAS) in closed-form analytical expressions. The power and energy analysis for single PWAS transmitter, single PWAS receiver and a complete PWAS pitch-catch setup were carried out. Frequency response functions were derived for voltage, current, complex power, active power, etc. They concluded that a judicious combination of PWAS size, structural thickness, and excitation frequency can ensure optimal energy transduction and coupling with the ultrasonic-guided waves travelling in the structure. However, they considered only the 1D guided axial and flexural wave for the analysis.

The above literature review shows that although a number of studies have been conducted for power and energy efficiency, but none have considered the influence of the bond layer. The analysis of preceding chapters shows that bond layer has strong influence on piezo-structure system. Therefore, the next section has aims to examine the power consumption and energy

efficiency related to EMI technique through the continuum based piezo-elastodynamic model, considering all piezo-mechanical properties of the adhesive bond along the bonding area. Hence, taking the advantage of accuracy and simplifying the continuum model, the power factor and energy conversion efficiency ratio has been rederived, where the shear stress and inertia effect are considered simultaneously. A modified coupling co-efficient has been proposed for continuum based signature to encounter the shear lag mechanism for piezo-transducer application.

6.4 ELECTRICAL POWER CONSUMPTION IN PIEZO-IMPEDANCE TRANSESDUCER

(i) Apparent Power

The apparent power (Volts-Amps), W_A in terms admittance function, can be defined as

$$P_{apparent} = W_A = V I = \frac{V_0^2}{2} |Y| \quad (6.7)$$

where $|Y|$ is absolute value of admittance signature and V and I are the root mean square values of the corresponding quantity. V_0 is the peak value of excited voltage. The apparent power is the quantity of power initially applied to the PZT patch to induce the strain-deformation. As we know, a piezo patch behaves as a capacitor, the induced displacement is proportional to the stored charge, and hence, the apparent power is greater than the true power.

(ii) Active (True) power

The active or the dissipative power (Watt), W_D can be defined as

$$P_{active} = W_D = W_A \cos \phi = \frac{V_0^2}{2} \operatorname{Re}(\bar{Y}) = \frac{V_0^2}{2} G \quad (6.8)$$

The active power is the measurement of the rate at which electricity performs work such as producing heat, light, or mechanical energy. The amount of power actually consumed in the piezo system and dissipated during the dielectric losses and structural losses results in the active or real power. The piezo capacitance causes the phase lag between the current and the voltage. The true power is eventually dissipated in the piezo system in the form of heat, sound and mechanical losses and reflects itself in system through acoustic impedance and structural damping.

(ii) Reactive Power

The vector difference between the apparent and true power is called reactive power. The reactive power, W_R can be expressed as

$$P_{reactive} = W_R = W_A \sin \phi = \frac{V_0^2}{2} \operatorname{Im}(\bar{Y}) = \frac{V_0^2}{2} B \quad (6.9)$$

The energy stored in the capacitive PZT patch undergoes periodical reversal in the direction of the energy flow. Some part of the energy is temporarily stored by itself due its conductive nature of PZT patch. Due to this, the reactive power of the piezo patch always remains and flows within it (similar to the strain energy stored in a spring-mass system).

In order to maintain the constant voltage supply to piezo-electric system, one needs to ensure meeting a minimum power requirement which is called the power rating below which the PZT patch will cease to operate. This is expressed in terms of the maximum absolute admittance as

$$P_{rating} = W_{rating} = \frac{V_0^2}{2} \max(|\bar{Y}|) \quad (6.10)$$

The relation between the apparent power, active power and reactive power can be formulated as

$$P_{\text{apparent}}^2 = P_{\text{active}}^2 + P_{\text{reactive}}^2 \quad (6.11)$$

The influence of the adhesive bonding on the electrical power components of piezo-structural interaction system has been shown in Figures 6.3, 6.4 and 6.5. In Figure 6.3, the influence of bond on apparent power is visible as decrease in the slope of curve and the decrease in the peak value as well. From the figure, it is clear that, due to the adhesive bonding, the power required by PZT patch to initiate the structural deformation has been obstructed by the presence of the bond. Similarly, Figure 6.4 shows the effect of the bond layer on the reactive power. It can be observed that the reactive part of the piezoelectric power (Eq. (6.9)), which is the stored charge, is virtually same as apparent power, because the imaginary admittance is almost same as the absolute value of complex electro-mechanical admittance due to the small magnitude of the real part. This indicates the strong reactive nature of electro-mechanical system. The piezo-coupled reactive power consist of the mechanical reactive power related to the mass (kinetic energy), spring (potential strain energy), and electric reactive power (electric and magnetic field energy of capacitors and inductors).

Power consumed by the PZT patch in terms of heat due to the resistive admittance of the PZT material as well as the losses in the structure is represented by the dissipative power component as shown in Figure 6.5. For bonding effect, the mechanical resistive power is more dominant than perfect bonding case, hence energy dissipation for coupled interaction phenomena gets lowered for adhesive bond compared to perfect bond. The phenomenon ultimately indicates that the entire process is mechanically more reactive because more energy is required to stores within piezo system to continue the coupled interaction process.

The power factor in electrical theory is defined as the ratio of dissipative power to supplied (or apparent) power. The power factor of an electrical system represents the capability of the electrical network to convert supplied electrical energy into heat, light, or mechanical energy. In the cases of PZT patch in the EMI technique, we can physically interpret the power factor as the efficiency or effectiveness of the piezo-patch to provide mechanical response of structure. The power factor of piezo-driven system can be defined as (Liang et al., 1994)

$$\cos \phi = \frac{W_D}{W_A} = \frac{\operatorname{Re}(\bar{Y}|_{\delta=0, \eta=0})}{|\bar{Y}|} = \frac{G_{(\eta=\delta=0)}}{|Y|} \quad (6.12)$$

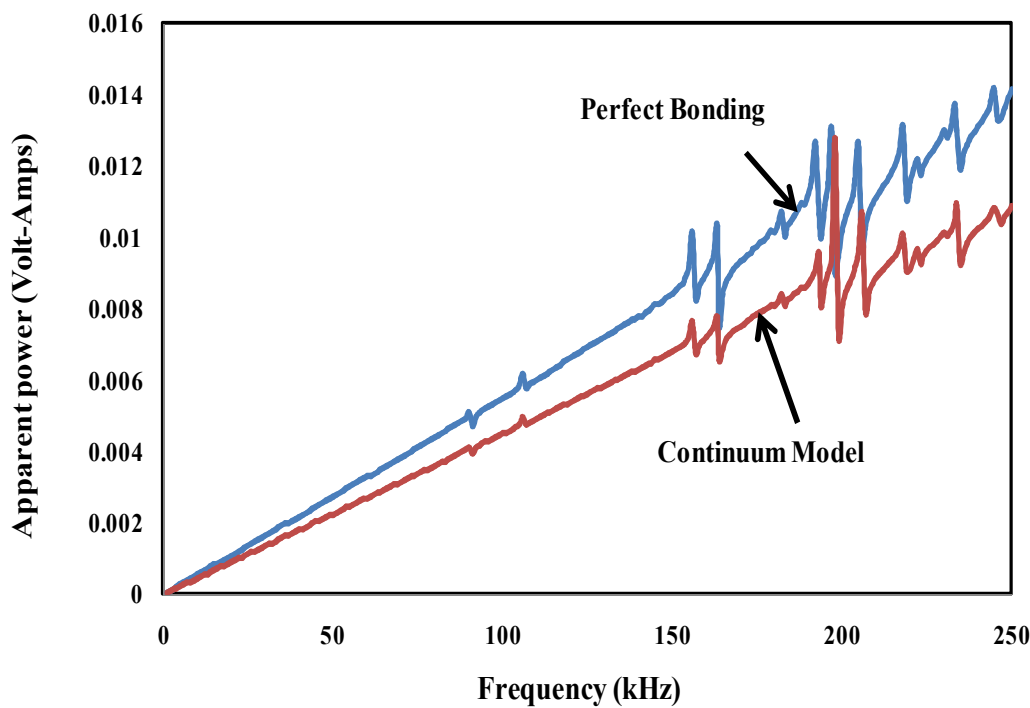


Figure 6.3 Apparent power consumption in piezo-impedance transducer

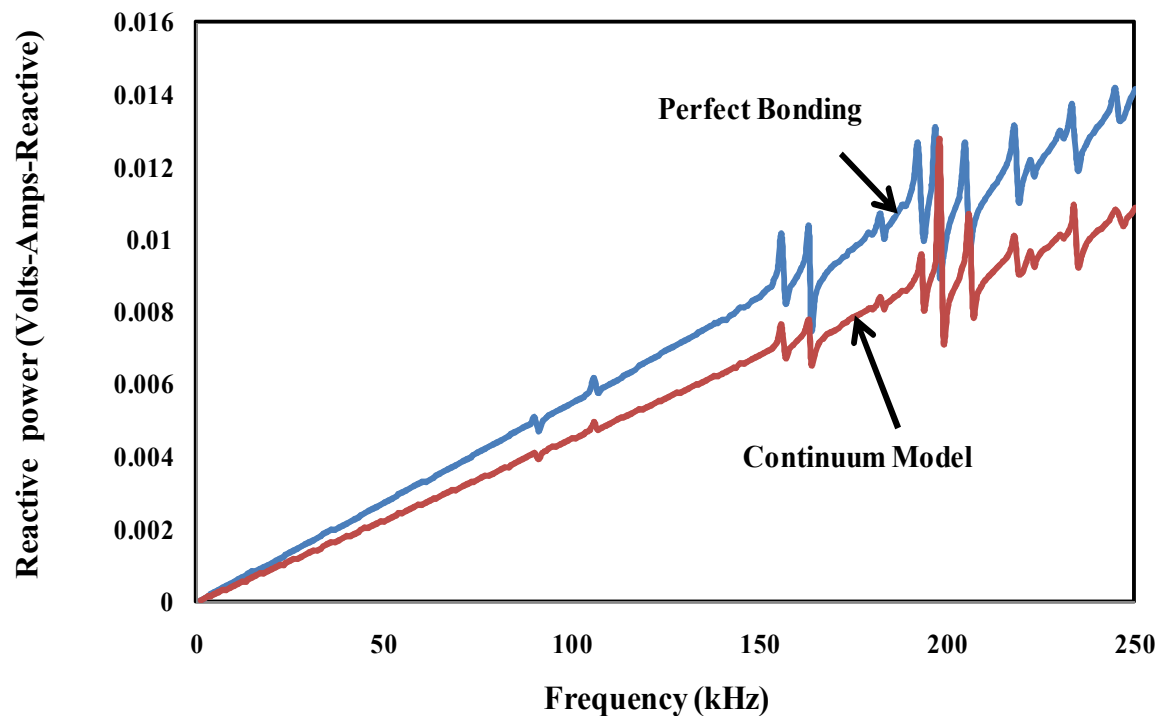


Figure 6.4 Reactive power consumption in piezo-impedance transducer

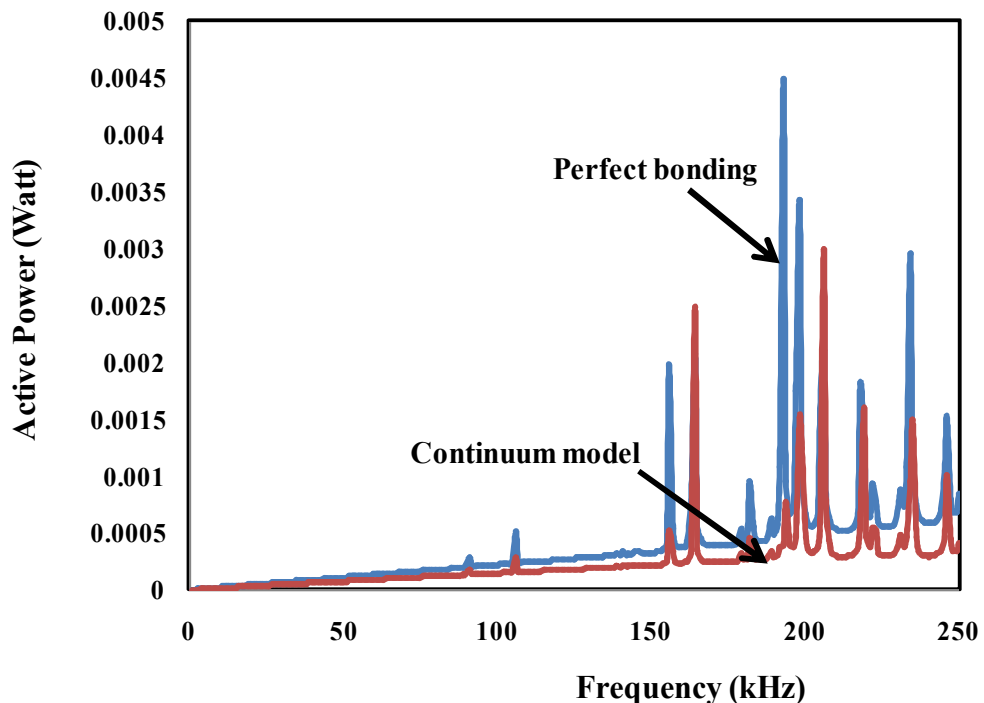


Figure 6.5 Active power consumption in piezo-impedance transducer

From Figure 6.5, it is clearly observed that, more power is dissipated (lowered resonance peak) for adhesive bonded case because additional losses (due to adhesive bonding) occur along with other conventional loss (heat, sound and electrical energy). In Figure 6.6, the power rating (the maximum power over the frequency range that piezo patch expected to operate) for three different models (perfect, refined and continuum) has been compared. The adhesively bonded PZT patch has lesser power rating than idealized perfect bond situation. The continuum model predicts marginally higher power than the refined model. The piezoelectric materials have an electro-mechanical efficiency (Power factor) which indicates the energy transfer rate between the stored strain energy to the electrical energy; however, it is only a material index and cannot be used to evaluate the effectiveness of piezoelectric actuators integrated in a mechanical material system. The system efficiency defined by Eq. (6.12) is used here to evaluate the the effectiveness of the PZT patch to excite the mechanical system, as graphically presented in Figure 6.7. The adhesively bonded PZT patch lower power factor than idealized perfectly bonded patch. A MATLAB code enlisted in Appendix E for calculation of electrical power component.

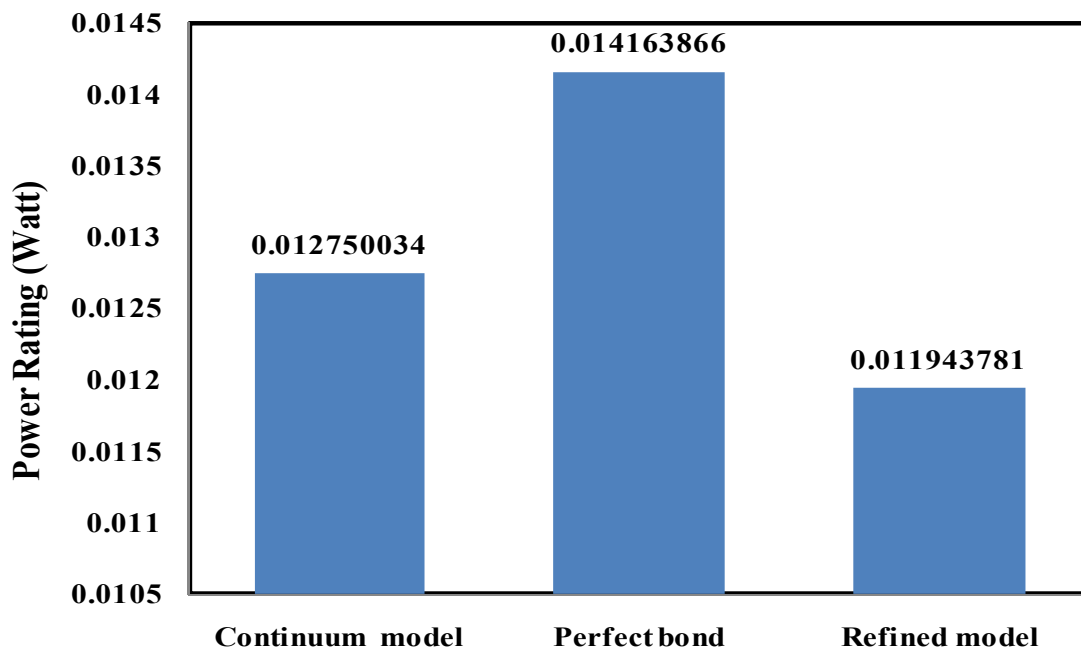


Figure 6.6 Comparison of maximum power requirement for piezo-structure interaction models

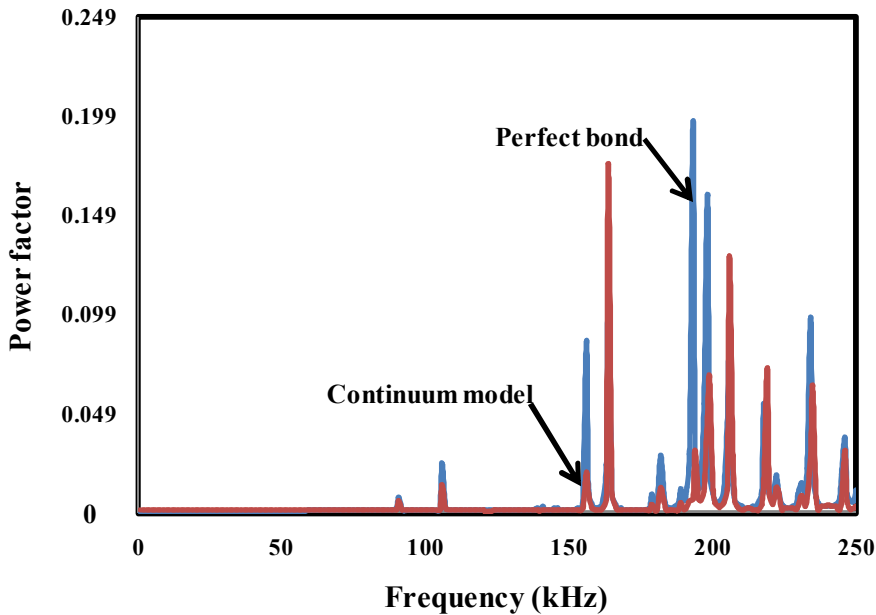


Figure 6.7 The efficiency of PZT patch to excite the piezo-active system

The height of a resonance peak indicates the effectiveness of the patch to excite that particular mode. For the bonding effect, the peak and the slope of the curve have been lowered as compared to perfect bond, which indicates that the overall efficiency of PZT patch has degraded in the presence bond. The actuator efficiency is important parameter in the optimal design of actuator configuration (actuator impedance) and location. Figure 6.8 illustrates how the power supplied to the system is consumed. The real admittance is divided into four distinct ways. The first plot results from the perfect bonding with piezo-mechanical loss being ignored. This is calculated by assuming zero internal damping and dielectric loss for the PZT patch for perfect bonding case excluding shear lag effect and also assuming $\eta=\delta=0$. The second plot results from the mechanical loss, which is calculated by assuming zero dielectric loss for the PZT patch ($\eta \neq 0, \delta = 0$) for perfect bonding case. The third curve is obtained for the dielectric loss, estimated by assuming zero internal damping ($\eta = 0, \delta \neq 0$) for perfect bonding case. The

fourth plot results when accounting for the shear lag effect calculated by assuming zero mechanical ($\eta=0$) and dielectric loss ($\delta=0$) for PZT patch, but considering the patch to be adhesively bonded.

6.5 ENERGY CONVERSION EFFICIENCY OF PIEZO-ACTIVE MECHANICAL SYSTEM

The energy consumption and requirements of an active control system are fundamental concern for the viability of piezo-active systems for various applications which are weight and volume sensitive, such as noise control of aircraft cabins, submarine quietening and the EMI technique for SHM based applications. The energy conversion factor represents the efficiency of the PZT patch for energy conversion from electrical to structural domain. When a PZT patch is integrated with an active mechanical system, energy conversion efficiency factor is required to estimate the usefulness of the piezo-active system, which in turn depends upon the mechanical damping, intermolecular bonding between the PZT patch and structure (characteristic of adhesive bond), structural stiffness, piezoelectric properties of the patch and the imposed boundary conditions.

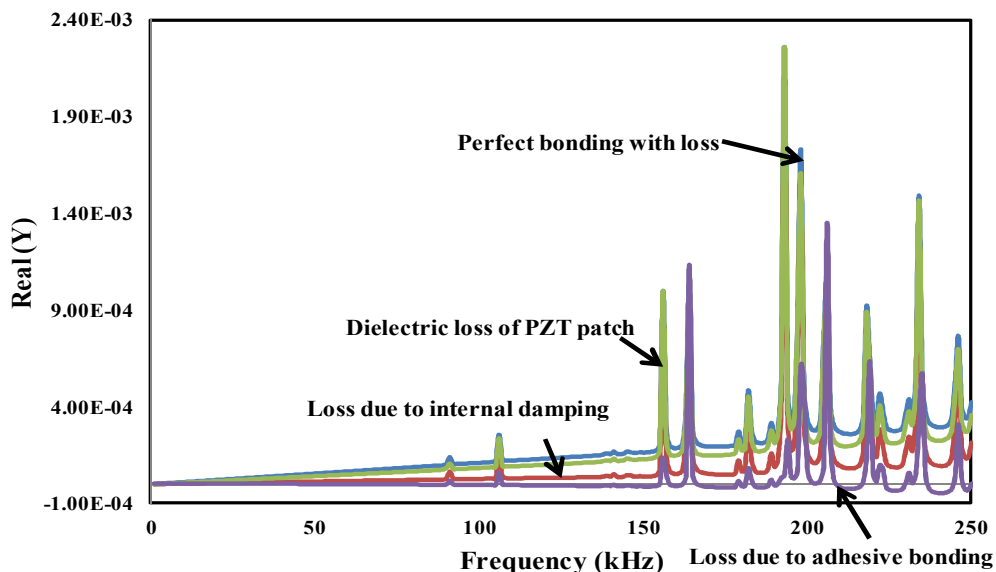


Figure 6.8 The Real part of coupled signature illustrating how active component of electrical power consumed in electro-mechanical interaction process

Liang et al. (1994) determined the power and energy variation for 1D electro-mechanical impedance model (see Fig. 2.2) to design an efficient intelligent structure and illustrated its optimized performance in real life applications by studying the different components of power (reactive, dissipative) and power efficiency relationship. They demonstrated numerically and experimentally that the total energy flow in the system produced conversional phenomena of electrical and thermal energy within the model to reflect the structural properties to reactive electrical parameters.

They predicted that, in the electro-mechanical coupling system, it is the strain energy (which is reactive in nature) which interacts with the system (converse effect, acts as actuator) and consumed in various mechanical phenomena (damage, failure and thermal loss) in the region of resonance peak. The over used or balanced strain energy is converted to electrical energy (direct effect, as sensor) and manifests as the coupled admittance signature. The drawback of this model is that it does not account for the energy losses due to shear lag effect, besides being restricted to 1D. Hence, power output is over estimated.

The energy dissipation within a PZT patch results from mechanical loss and electrical loss. The modelling of these dissipations in the frequency domain analysis is usually conducted by using complex elastic modulus $\overline{Y^E} = Y^E(1+nj)$ and complex electrical permittivity $\overline{\epsilon_{33}^T} = \epsilon_{33}^T(1-\delta j)$. Some studies (Bondarenko et al., 1982; Martin, 1974) suggest a third source of energy dissipation resulting from the ‘imperfection of energy conversion’, which is depicted by the hysteresis between the applied electrical field and induced strain. The energy conversion within a PZT patch involves the conversion of electrical energy to mechanical potential and kinetic energy and electrical energy to heat (dissipation).

Later on, Liang et al. (1996) made an investigation for specifically coupled mechanical and electrical performance and derived working index for the piezo-impedance model. They mainly focused on the methodology and its utilization in various applicable fields such as optimal actuator location, modal analysis and acoustic power prediction etc.

In a different publication (Liang et al., 1995) a simplified actuator power factor was derived to obtain the structural response for changing actuator location and configuration, expressed as

$$\psi = \frac{2\pi\eta K_M y^2}{K_E V E^2} \quad (6.13)$$

where η is the structural loss, y is the structural response and E refers to applied electric field. K_M and K_E are the proportionality factors for total mechanical and electrical energy and V is the actuator volume. They concluded that the optimized actuator power factor is more useful to obtain the structural response for a different actuator location. It is also applicable for experimentation and system optimization of an active control model.

Siorhi and Chopra (2000a) determined the power consumption of piezo-active system for surface bonded and free PZT patch experimentally, duly considering including the non-liner variation of dielectric permittivity ($\overline{\epsilon_{33}^T}$) and dissipation factor ($\tan \delta$) for a particular electric field. Once the complex electro-mechanical admittance is calculated, the voltage drawn and current flow for an active piezo system can be easily estimated. Siorhi and Chopra (2000b) introduced the shear lag correction for strain voltage relationship by introducing effective sensing length (K_b), expressed as

$$\epsilon_1 = \frac{V_0}{K_b K_p S_q^*} \quad (6.14)$$

where K_p and K_b are the correction factors to take care for shear lag and Poisson's ratio. S_q^* is the circuit sensitivity.

6.6 ENERGY CONVERSION EFFICIENCY RATIO FOR BONDING INFLUENCE ON PIEZO-IMPEDANCE SYSTEM

The energy conversion efficiency (λ) can be defined as the ratio of the total energy used for mechanical response produced (from the piezo-electric induced strain) to the total energy supplied to the system during the piezo-mechanical interaction phenomena. Mathematically, it can be expressed as (Liang et al., 1995)

$$\lambda = \frac{E_{\text{mech}}}{E_{\text{sup}}} \quad (6.15)$$

The above ratio represents the inside direction of flow of physical energy. Therefore, in dynamic application, the electrical energy and the power will be averaged under each cycle of alternating current. The energy lost per cycle per second will be in the form of dissipative and reactive energy, according to which, the loss ratio can be divided into two categories. The first term is the *piezo-dissipative loss ratio*, which is concerned with dissipative power (loss due to heat, sound, structural damping and dielectric loss) and can be defined as (Liang et al., 1996)

$$\lambda_{PZT-\text{Str}} = \frac{E_{\text{mechanically-dissipative}}}{E_{\text{total-dissipation}}} = \frac{\text{Re}(P_m)}{W_D} \quad (6.16)$$

Where P_m is the mechanical power, which can be computed as $\bar{Y}_{\delta \rightarrow 0}$ ($\delta=0$ is avoided to rule out a negative value). The second term is *piezo-reactive loss ratio* resulting due to electrically reactive nature of piezo capacitance, which always has tendency to store energy in the system

temporarily. So, it represents the instantaneous energy conversion factor of dynamic piezo-structure system, and can be formulated as

$$\lambda_{PZT-elec} = \frac{E_{mechanically-reactive}}{E_{Total-reactive}} = \frac{\text{Im}(P_m)}{W_R + \text{Im}(P_m)} \quad (6.17)$$

Investigating power conversion will also provide information on the direction of the energy flow in piezo-active system. The energy conversion efficiency ratio defined by Eqs. (6.16) and (6.17) is obtained for both perfect bonding and adhesive bonding case. Figure 6.9 compares the piezo dissipative loss ratio of piezo-active model for perfect bonding and adhesive bonding case ($\delta=0.002$, $1/10^{\text{th}}$ of the actual value)). The plot has been restricted to initial frequency range (At resonance peaks 91 kHz and 106 kHz). From the Figure 6.9, it can be observed that for the bonding case, the efficiency ratio has been low, that is, lesser energy is dissipated in the form of heat, sound and damping in the presence of the adhesive bond indicating less efficient piezo-structural interaction. Figure 6.10 similarly shows the plot for the reactive loss efficiency ratio. There is increase in efficiency for the bonding case because here the mechanical reactive part becomes more dominant than the mechanical resistive energy. In other words, at higher frequency range, the energy conversion phenomenon becomes very complex.

The reactive energy conversion efficiency ratio given by Eq. (6.17) describes the instantaneous energy conversion and represents the real coupled interaction phenomena within the PZT patch for any dynamic application. For this process conversion, the mechanical reactive energy is thus significant for adhesive bonding as compared to perfect bonding case, because the presence of bonding obstructs the deformed strain to produce electrical response (voltage) for sensor application as well as during actuation.

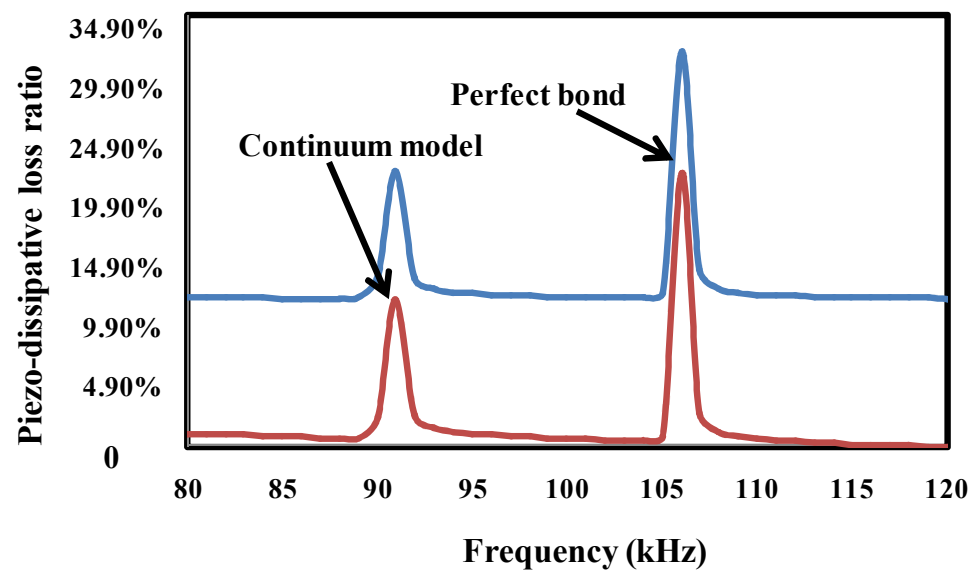


Figure 6.9 Dissipative energy conversion efficiency ratio for integrated piezo-structural model

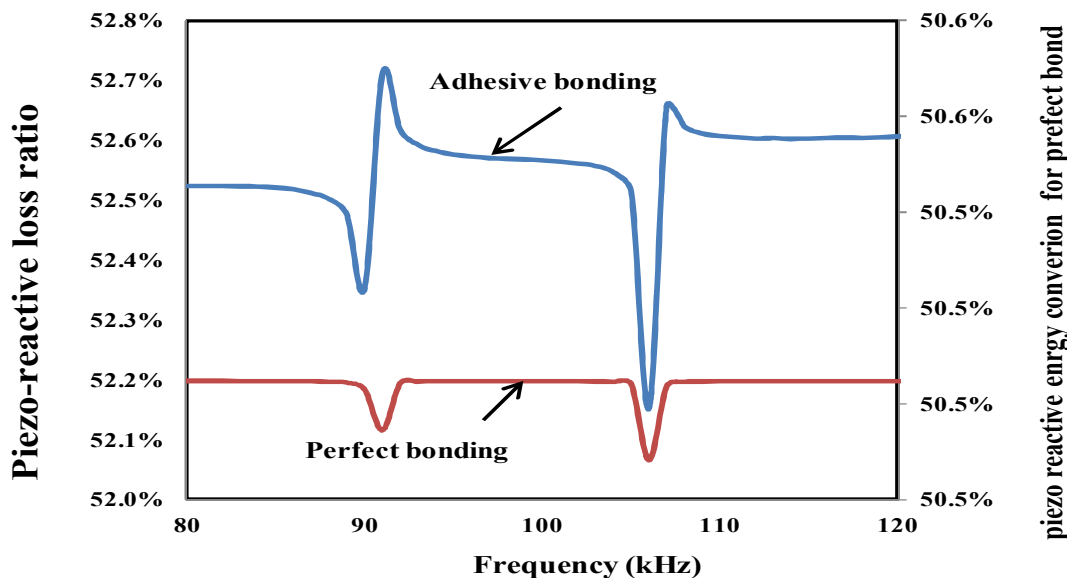


Figure 6.10 Reactive energy conversion efficiency ratio for integrated piezo-structural model

6.7 FORMULATION OF MODIFIED ELECTRO-MECHANICAL COUPLING CO-EFFICIENT

The electro-mechanical coupling is the process of phase transformation of crystals from ferroelectric to paraelectric phase, famously known as the morphic effect. It is an indicator of the effectiveness of the piezo-patch to convert the electrical energy to mechanical energy and vice versa. The value of electro-mechanical co-efficient (k_{eff}^2) depends on resonance frequency, modes of vibration, shapes and material losses of the PZT patch. Usually, the k_{eff}^2 (theoretical maximum value) valued is supplied by manufacturers. Theoretically it can be expressed as (Ikeda, 1990)

$$K_{\text{eff}}^2 = \frac{\text{Mechanical energy converted due to piezo deformation}}{\text{Total electrical energy input}} \quad (6.18)$$

It can be seen that at lower frequency range, the force transfer phenomena is accelerated to 50 to 70% as reported by Liang et al. (1996), so that the energy delivered from one form to other form is greatly enhanced. For this reason, the higher value of k_{eff}^2 at lower frequency range is generally adapted by manufacturer for the well designed piezo-ceramic element, whose efficiency of conversion can be maximized up to 95%. So, by definition the electro-mechanical coupling co-efficient can be defined as the ratio of the converted, usable energy delivered by the piezo-electric element to the total energy supplied to the element.

k_{eff}^2 , is frequently used to express the effective coupling coefficient of an arbitrary resonator. Experimentally, it can be measured from fundamental resonance or at any overtone and can be expressed as (Seacor Piezoceramic)

$$k_{eff}^2 = \frac{f_a^2 - f_r^2}{f_r^2} \quad (6.19)$$

where f_a and f_r are the frequencies at anti resonance and resonance point. The coupling coefficient can be calculated for the various modes of vibration. For SHM, the piezo mechanical coupling coefficient for one dimensional excitation (lateral or longitudinal) can be defined as (Mason, 1966).

$$k_{31} = \frac{d_{31}}{\sqrt{\varepsilon_{33}^T S_{11}^E}} \quad (6.20)$$

Where $\overline{\varepsilon_{33}^T}$ and $\overline{S_{11}^E} = \frac{1}{Y_{11}^E}$ are the two complex terms, which can be split into real and imaginary

parts. The real part of the conversion factor indicates the capability of a PZT material to convert electrical energy to mechanical energy and vice versa. The imaginary part reflects the energy dissipation and should remain positive according to the sign convention used in a thermodynamic system (Liang et al., 1996). Liang et al. (1995) proposed the modified electro-mechanical coupling co-efficient to take care of all the losses (piezoelectric and mechanical), expressed as

$$k_{eff}^2 = \frac{[d_{31}(1-i\eta_{em})][d_{31}(1-i\eta_{em}^*)][Y^E(1+i\eta)]}{\varepsilon_{33}^T(1-i\delta)} \quad (6.21)$$

where d_{31} is the piezoelectric strain coefficient, Y^E is the elastic modulus, ε_{33}^T the electric permittivity. δ and η are the dielectric and mechanical loss factor of PZT patch. η_{em} is the piezo-mechanical loss factor for active system. The approach was somehow improved but not realistic as its still ignored the force/strain transfer between the PZT and structure through bond layer. They rederived the coupling co-efficient introducing a complex piezoelectric constant

$d(1+i\eta_{em})$ to describe the hysteretic behaviour, where η_{em} is the piezo-mechanical loss factor which was measured by experimentally as

$$\eta_{em} = 0.034 + 2.92 \times 10^{-5} f \quad (6.22)$$

where f is the frequency in Hz. η_{em}^* is the complex conjugate of η_{em} . The electrical energy input from the piezo-capacitor, can expressed in mathematically as

$$E_{elect} = \frac{1}{2} CV^2 \quad (6.23)$$

where $C = \frac{k_r \varepsilon_0 l b}{t}$, where k_r is the dielectric constant and ε_0 the electrical permittivity for vacuum.

For PZT materials of grade PIC 151(PI Ceramic, 2010) following values are considered for present derivation. $k_r = 2400$ and $\varepsilon_0 = 8.85 \times 10^{-12} F/m$

Total mechanical energy stored in PZT patch due to piezo-mechanical displacement is given by

$$E_{mech} = \frac{1}{2} \int_V T_1 S_1 dV \quad (6.24)$$

where T_1 and S_1 are axial stress and strain along x -direction respectively , and the stress (T_1) can expressed as

$$T_1 = \overline{Y^E} (S_1 - \Lambda) \quad (6.25)$$

Hence, from Equations (6.24) and (6.25),

$$E_{mech} = A \int_l \left[\overline{Y^E} (S_1 - \Lambda) S_1 \right] dl \quad (6.26)$$

Now, we can define coupling co-efficient as (k_{eff}^2) as for mechanical energy to electrical energy

$$k_{eff}^2 = \frac{A \int_l \left[\overline{Y_{11}^E} (S_1 - \Lambda) S_1 \right] dl}{\frac{1}{2} C V^2} \quad (6.27)$$

This modified coupling co-efficient (k_{eff}^2) is derived with consideration of the energy loss due to shear lag along with all the complex conjugates (dielectric and mechanical loss) of piezo properties, and is thus more accurate and realistic. The value for k_{eff}^2 has been estimated for the conversion of mechanical energy to the electrical energy and vice versa at first natural frequency (91 kHz). For mechanical to electrical energy conversion the coupling coefficient is found to be 0.1545 and for electrical to mechanical energy conversion it is estimated as 6.4734. The value of k_{eff}^2 for mechanical energy conversion to electrical response is low because the shear lag phenomena play a significant role due to presence of adhesive bond.

6.8 CONCLUDING REMARKS

This chapter has presented the electrical requirements of the proposed piezo bond model and investigated its real life utility and applications in the area of modelling of active piezo-structure interaction. Different components of input power have been determined for adhesive effect using continuum based modelling approach. For better understanding of piezo-structure coupled interaction mechanics, various energy conversion efficiency ratios and a new modified electro-mechanical coupling co-efficient have been derived, which further aid in effective understanding of the piezo-elastodynamic model and can facilitate optimum localization of PZT patch in host structure.

Chapter-7

CONCLUSIONS AND RECOMMENDATIONS

7.1 INTRODUCTION

This thesis embodies the findings from the research involving the development of a refined analytical shear lag model for piezo impedance transducer considering all the dynamic terms neglected in previous models, its extension to continuum based model for rigorous consideration of force transfer mechanism in piezo-elastodynamic system. Along the bond area, the proposed approach takes care of all piezo-mechanical variables. The thesis culminates in the study of power consumption and energy efficiency for bonding effects related to the EMI technique. The only choice of analytical approach was motivated by the discrepancies and other problems associated with coupled finite element based approach. Specifically, a major objective of the research was to upgrade the previous shear lag model by considering shear stress and inertia factor simultaneously and in a continuous manner. The research is further extended to combined inertia effect of PZT patch and adhesive mass, which is not reported till date.

Major novelty in the present research is the new continuum based electro-mechanical formulation, which very simple and accurate and eliminates all hassle of calculation of complex mechanical impedance terms (Z_s, Z_{eq}, Z_a) required in the previous models. These terms are discrete approximations to true structural impedance for a real piezo-mechanical strain deformation along the bond layer.

The following sections outline in detail the major contributions, conclusions and recommendations stemming out from this research.

7.2 RESEARCH ORIGINALITY AND CONTRIBUTIONS

Monitoring a structure for damage detection through the EMI technique should be accurate enough to take care of all the forces, stresses and strains developed due to piezo deformation along with different bonding conditions and sensor location to enable optimized SHM. This research aimed at developing a new and more accurate shear lag model relevant to the EMI technique. The existing models are deficient in not considering the inertia and shear lag terms simultaneously. Further, they do not account for a continuous transfer of stresses throughout the contact area. The EMI signatures are significantly affected by presence of the bond layer between PZT patch and host structure.

The original contribution of this research work can be summarized as follows

- 1) A new analytical refined shear lag model has been developed which considers the shear stresses developed during PZT patch's deformation in the interfacial layer and the inertia term contributed by PZT patch as well as the bond layer simultaneously. All previous models ignored simultaneous contribution.
- 2) The refined model has further been extended to a new continuum based coupled admittance model, which enables a more accurate modelling of the force transmission. This modelling approach circumvents the determination of lumped impedance terms.
- 3) A detailed study on power consumption and energy efficiency has been carried out for the piezo-structure system based on the developed model taking due consideration of the bond layer. To quantify the energy conversion efficiency of bonded piezo patch, various loss ratios have been derived in accordance with the physical energy flow in PZT patch during interaction. The effect of various losses

(electrical and mechanical) on overall power performance of the piezo-impedance model has been studied in detail.

7.3 RESEARCH CONCLUSIONS

Major research conclusions and contributions from the research can be summarized as follows

- (i). As a first preliminary step, a detailed numerical investigation of shear mechanism has been carried out using FE coupled field analysis. The FE based shear lag model has developed for both 1D and 2D PZT-structure coupling. The correct input format (conversion from IEEE format to ANSYS format) of piezoelectric and structural elastic compliance matrices has been accounted in the analysis. Keeping in view that shear and inertia effects are automatically taken into consideration in coupled-field analysis, it could be a preferred option although it requires considerable modelling effort. This conversion of input material properties has not been considered in similar studies reported previously in the literature. The admittance signature resulting from harmonic analysis found to be inaccurate. The values of conductance (G) and susceptance (B) are found to be lower as compared to experimental and analytical values. A major discrepancy found is the values of susceptance are negative. Parametric studies go well with the models. The problem is further compounded by the necessary transformation of material and piezoelectric matrices, due to different norms prevailing in IEEE standards and conventional continuum mechanics. This could be a source of utter confusion for the users. This has motivated the researcher towards development of the closed form analytical solution for shear lag model.
- (ii). Step-by-step derivation of piezo-bond-impedance model with proper inclusion of shear lag effect and the inertia force concurrently has been done starting from the governing dynamic

shear lag equilibrium equation. Form this model, results have been compared with existing models and also the experimental signatures. The inertia effect is found to significantly affect the coupled EMI signature (lowering the resonance peaks in conductance and overall slope of the curve in susceptance). The overall results are better qualitative match with the experimental results. The model has been further extended by considering the adhesive mass and inertia in addition to that of PZT patch. However the mass of adhesive has very negligible effect on coupled admittance signature. The variance of the shear stress, the mechanical strain and the effective axial stress profiles have been investigated based on the refined model. A detailed parametric study has also been carried out for better understanding of the phenomena.

- (iii). The above formulation are extended to a continuum based admittance piezo-elastodynamic model, in which the bond layer effect is considered continuously along the sensor length rather than restricting it to the edge/boundary of the PZT patch as considered earlier. The continuum approach eliminates the hassle of computing the equivalent impedance terms (Z_a and Z_s), in addition to ensuring higher accuracy. The continuum signature has been compared with both refined model and perfect bonding. For real part (G), the continuum signature is much lower than other models. For the imaginary part, the slope has been lowered further as compared to refined model but the peak values are almost same as that of refined model. The continuum approach has also been extended to investigate the additional effect of adhesive layer mass, which is found to have only marginal effect on the signature by slight lowering peaks and as well as slope of curve, which makes them close to experimental results .

A new continuum displacement term (U_{con}) has been proposed, which accounts for continuum stress and strain developed during the piezo deformation. Parametric studies have also been carried out for the continuum signature with varying piezoelectric and bond properties.

- (iv). Form the parametric studies of the refined and the continuum model, one can arrive at conclusion that the smallest possible bond thickness be should maintained for best results in SHM. The higher shear modulus and lower mechanical damping of bond layer can further enhance the effectiveness of piezo-structure interaction. The sensor length should be maintained to smaller value (5mm to 10mm) for better interaction.
- (v). As a further application of the continuum shear lag model, the electrical power consumption and energy conversion has been investigated. Triangular component of piezoelectric power has been rederived duly considering the adhesive bonding effect. The presence of the bond layer makes the piezo-elastodynamic model mechanically more reactive, implies frequent energy conversion from mechanical to electrical energy, but still stored in the system. The apparent and the reactive power components are significantly decreased because the finite thickness of bond layer obstructs the piezo-deformation. For sensing case, again the adhesive bond obstructs the mechanical stain to produce electrical voltage by additionally dissipating the electrical energy in terms of heat and sound, hence the dissipative power for bonding case has also decreased.

The issues related to energy conversion within an active control system involve conversion between electrical to mechanical energy and vice versa. Being able to quantify various energy conversion processes and to understand the basic interaction mechanics of piezo-active control systems duly considering the bond effect, two types of energy conversion

efficiency ratio have been derived i.e. dissipative and reactive energy conversion efficiency ratios. From these ratios, it can be concluded that for the adhesive bonding, the mechanical reactive power is more dominant than the electrical dissipative power, which is opposite for the perfect bonding case.

The main energy losses in the PZT patch during the energy conversion process are the mechanical and dielectric losses. The real part of the coupled EMI signature is more sensitive to these losses, which indicates the capability of a PZT patch to convert electrical energy to mechanical energy and vice versa.

7.4 RECOMMENDATIONS

The following tasks are recommended to be undertaken to continue further research in this field.

- (i) The coupled FE shear model could be further extended to carry out damage localization studies considering bond layer simulation. An input system consistent with IEEE norms may be developed.
- (ii) Present shear lag solution can be further extended to different cases of bonding with anisotropic material properties, edge imperfections, debonding and bonding quality degradation etc. More exploration can be done for contribution of imaginary susceptance towards the shear-lag phenomena.
- (iii) In this research, the bond effect has only been studied analytically and numerically. It is recommended that future studies may be the investigation of piezo-bond-structure interaction through advanced microscopic technologies through atomic force microscope (AFM) and piezoresponce force microscope (PFM)
- (iv) Further studies can be extended to explore the utilization of the continuum based admittance signature for damage detection and crack propagation in real life systems

- (v) The study on power consumption and system energy transfers of proposed shear lag model can be extended for following cases
- a. The amount of heat and sound generation from the actuators and lost during the coupled interaction, which is essential in the thermal stress analysis of induced strain actuators, can be evaluated.
 - b. Continuum based piezo-elastodynamic model may be considered as an aid in designing energy-efficient intelligent material systems and structures.

REFERENCES

1. Aktan, A. E., Helmicki, A. J. and Hunt, V. J. (1998), "Issues in Health Monitoring for Intelligent Infrastructure," Smart Materials and Structures, 7(5), 674-692.
2. Allik, H. and Hughes, T. J. R. (1970), "Finite element method for piezoelectric vibration," International Journal for Numerical Methods in Engineering, 2(2):151–157.
3. Annamdas, V. G. M. (2007), "Characterization of Smart PZT Transducer and Admittance Signatures Using PZT-structure Interaction Models for Structural Health Monitoring," PhD Thesis, Nanyang Technological University, Singapore.
4. Annamdas, V. G. M. and Soh, C. K. (2007a), "Three Dimensional Electromechanical Impedance Model I: Formulation of Directional Sum Impedance," Journal of Aerospace Engineering, ASCE 20, 53-62.
5. Annamdas, V. G. M. and Soh, C. K. (2007b), "Three Dimensional Electromechanical Impedance Model II: Damage Analysis and PZT Characterization," Journal of Aerospace Engineering, ASCE, 20, 63-71.
6. ANSYS (2010), "ANSYS VERSION 12.0," <http://www.ansys.com>.
7. Ayres, J. W., Lalande, F., Chaudhry, Z. and Rogers, C. A. (1998), "Qualitative Impedance-Based Health Monitoring of Civil Infrastructures", Smart Materials and Structures, 7(5), 599-605.
8. Bailey, T. and Hubbard, J. E. (1985), "Distributed Piezoelectric –Polymer Active Vibrational Control of a Cantilever Beam," AIAA Journal of Guidance of Control, 6(5), 605-611.
9. Balamurugan, V. and Narayan, S. (2008), "A piezolaminated composite degenerated shear finite element for active control of structures with distributed piezosensors and actuators," Smart materials and Structures, 17, 035031.
10. Bhalla, S. (2001), "Smart System Based Automated Health Monitoring of Structures," M.Eng. Thesis, Nanyang Technological University, Singapore.
11. Bhalla, S. and Soh, C. K. (2003), "Structural Impedance Based Damage Diagnosis by Piezo-Transducer," Earthquake Engineering and Structural Dynamics, 32(12), 23-33.

-
12. Bhalla, S. (2004), "A Mechanical Impedance Approach For Structural Identification, Health Monitoring and Non-Destructive Evaluation Using Piezo-Impedance Transducer," Ph. D Thesis, Nanyang Technological University, Singapore.
 13. Bhalla, S. and Soh, C. K. (2004a), "Structural Health Monitoring by Piezo-Impedance Transducers I: Modelling," Journal of Aerospace Engineering, ASCE, 17(4), 154-165.
 14. Bhalla, S. and Soh, C. K. (2004b), "Structural Health Monitoring By Piezo-Impedance Transducers II: Applications," Journal of Aerospace Engineering, ASCE, 17(4), 166-175.
 15. Bhalla, S. and Soh, C. K. (2004c), "Impedance Based Modelling for Adhesively Bonded Piezo- Transducers," Journal of Intelligent Material Systems and Structures, 15(12), 955-972.
 16. Bhalla, S., Yang, Y. W., Zhao, J. and Soh, C. K. (2005), "Structural Health Monitoring of Underground Facilities-Technological Issues and Challenges," Tunnelling and Underground Space Technology, 20(5), 487-500.
 17. Bhalla, S., Gupta, A., Bansal, S. and Garg, T. (2009), "Ultra Low Cost Adaptations of Electro-Mechanical Impedance Technique for Structural Health Monitoring," Journal of Intelligent Material Systems and Structures, 20(8), 991-999.
 18. Boller C. (2002), "Structural Health Management of Ageing Aircraft and Other Infrastructure", Monograph on Structural Health Monitoring, Institute of Smart Structures and Systems (ISSS), pp. 1-59.
 19. Bondarenko A A., Karas, N. I. and Ulitko, A. F. (1982), "Methods for Determining the Vibrational Dissipation Characteristics of Piezoelectric Structural Elements" translated from Prikladnaya Mekh. (Plenum), 18, 104–108.
 20. Carrera, E. and Boscolo M. (2007), "Classical and Mixed Finite Elements for Static And Dynamic Analysis of Piezoelectric Plates," International Journal for Numerical Methods in Engineering, 70(10), 1135–1181.
 21. Chaudhry, Z., Joseph, T., Sun, F. and Rogers, C. A. (1995), "Local-Area Health Monitoring of Aircraft Via Piezoelectric Actuator/Sensor Patches," Proceedings of SPIE, March, San Diego, USA, 24-43.

22. Cheng, C.C. and Lim, C.C. (2005), "An Impedance Approach for Vibration Response Synthesis Using Multiple PZT Actuator," Sensors and Actuators A, 118, 116-126.
23. Crawley, E. F. and de Luis, J. (1987), "Use of Piezoelectric Actuators as Elements of Intelligent Structures," AIAA Journal, 25(10), 1373-1385.
24. Crawley, E. F. and Anderson, E. H. (1990), "Detailed Models of Piezoceramic Actuation of Beams," Journal of Intelligent Material Systems and Structures, 1, 5-25.
25. De Faria, A. R. (2003), "The Effect of Finite Thickness Bonding on the Sensing Effectiveness of Piezoelectric Patches," Technical Note, Smart Material and Structures, 12, N5-N8.
26. Dirmitriadiis, E. K., Fuller, C. K. and Rogers, C. A. (1989), "Piezoelectric Actuators for Distributed Noise and Vibration Excitation in Thin Plates," ASME Failure Prevention and Reliability, DE, 6:223-233.
27. Doherty, J. E. (1987), "Nondestructive Evaluation," Chapter 12 in Handbook on Experimental Mechanics, A. S. Kobayashi Edt., Society for Experimental Mechanics, Inc.
28. Dugnani, R. (2009), "Dynamic Behaviour of Structure-mounted Disk-shape Piezoelectric Sensors Including the Adhesive layer," Journal of Intelligent Material Systems and Structures, 20, 1553-1564.
29. Encarta Concise Encyclopedia, 2012, <http://scholar.lib.vt.edu/theses/available/etd-042299-150134/unrestricted/Chapter2.pdf>.
30. Eric Quili Sun, " Shear locking and hourgassing in MSC Nastran, Abaqus and Ansys" (<http://docstoc.com/> FEA Course notes).
31. Fairweather, J. A. (1998), "Designing with Active Materials: An Impedance Based Approach," Ph.D. Thesis, Rensselaer Polytechnique Institute, New York.
32. Farrar, C. R. and Jauregui, D. A. (1998), "Comparative Study of Damage Identification Algorithms Applied to a Bridge: I. Experiment", Smart Materials and Structures, 7(5), 704-719.

33. Ghoshal, A., Harrison, J., Sundaresan, M. J., Hughes, D. and Schulz, M. J. (2001), "Damage Detection Testing on a Helicopter Flexbeam," Journal of Intelligent Material Systems and Structures, 12(5), 315–330.
34. Giurgiutiu, V. and Rogers, C. A., (1997), "Electromechanical (E/M) Impedance Method for Structural Health Monitoring and Non-Destructive Evaluation", Proceedings of International Workshop on Structural Health Monitoring, edited by F. K. Chang, Stanford University, Stanford, California, September 18-20, Technomic Publishing Co., pp. 433-444.
35. Giurgiutiu, V. and Rogers, C. A. (1999), "Modelling of Electromechanical Impedance Response of Damaged Composite Beam," ASME Winter Annual Meeting, ASME Aerospace and Materials Divisions, Adaptive Structures And Material Systems Symposium, November 14-19, 1999, Nashville, TN, AD-Vol. 59, MD-Vol. 87, 39-46.
36. Giurgiutiu, V., Redmond, J., Roach, D. and Rackow, K. (2000), "Active Sensors for Health Monitoring of Ageing Aerospace Structures", Proceedings of the SPIE Conference on Smart Structures and Integrated Systems, edited by N. M. Wereley, SPIE Vol. 3985, pp. 294-305.
37. Giurgiutiu, V. (2000), "Active-Materials Induced-Strain Actuation for Aeroelastic Vibration Control," Shock and Vibration Digest, 32(5), 355-368.
38. Giurgiutiu, V. and Zagari, A. N. (2000), "Characterization of Piezoelectric Wafer Active Sensors", Journal of Intelligent Material System and Structure, 11, 957-967.
39. Giurgiutiu, V. and Zagari, A. N. (2002), "Embedded Self-Sensing Piezoelectric Active Sensors for Online Structural Identification," ASME Journal of Vibration and Acoustics, 124(1), 116-125.
40. Giurgiutiu, V. and Santoni-Bottai, G. (2009), "Extension of the Shear-Lag Solution for Structurally Attached Ultrasonic Active Sensors", AIAA Journal, 47(8), 1980-1983.
41. Gopalakrishnan, S., Ruzzene, M. and Hanagud, S. (2008), "Spectral Finite Element Method" Springer-Germany.
42. Gopalakrishnan, S., Ruzzene, M. and Hanagud, S. (2011), "Computational Techniques for Structural Health Monitoring" Springer –UK.

-
43. Grisso, B. L. (2004), "Considerations of the Impedance Method, Wave propagation and Wireless System for Structural Health Monitoring," M.S. Thesis, Virginia Polytechnic Institute and State University, Blacksburg, Virginia
44. Hagood, N. W. and Flotow, A. V. (1991), "Damping of Structural Vibrations with Piezoelectric Materials and Passive Electrical Networks," Journal of Sound and Vibration, 146(2), 243–268.
45. Han, J. H., Rew, K. H. and Lee, I. (1997), "An Experimental Study of Active Vibration Control of Composite Structures with Piezoceramic Actuator and a Piezo-film sensor," Smart Materials and Structures, 6, 549-558.
46. Han, L., Wang, X. D. and Sun, Y., (2008), "The Effect of Bonding Layer Properties on The Dynamic Behaviour of Surface Bonded Piezoelectric Sensors," International Journal of Solid and Structure, 45, 5599-5612.
47. Huang, G., Song, F. and Wang, X. (2010), "Quantitative Modelling of Coupled Piezo-Elasto dynamic Behaviour of Piezoelectric Actuators Bonded to an Elastic Medium for Structural Health Monitoring: A Review," Sensors, 10, 3681-3702.
48. Hwang, W. S. and Park, H. C. (1993), "Finite Element Modelling of Piezoelectric Sensors and Actuators," AIAA Journal, 31(5), 930–937.
49. IEEE Standard on Piezoelectricity. 1987. ANSI/IEEE., Std. 176
50. Ikeda, T. (1990), "Fundamental of Piezoelectricity," Oxford University Press, Oxford.
51. Inman, D. J. (2005), "Damage Prognosis: For Aerospace Civil and Mechanical System," Willy Publication.
52. Jin, C. and Wang, X. (2011), "Analytical Modelling of the Electromechanical Behaviour of Surface-Bonded Piezoelectric Actuators Including the Adhesive Layer," Engineering Fracture Mechanics, 78, 2547–2562.
53. Kawiecki, G. (2001), "Modal Damping Measurement for Damage Detection," Smart Materials and Structures, 10, 466-471.

-
54. Kersey, A. D., David, M. A., Patrick, H. J., LeBlanc, M., Koo, K. P., Askins, C. G., Putnam, M. A. and Friebele, E. J. (1997), "Fiber Grating Sensors," *Journal of Lightwave Technology*, 15, 1442 – 1463.
55. Kessler, S. (2002), "Piezoelectric-Based In-Situ Damage Detection of Composite Materials for Structural Health Monitoring Systems," Massachusetts Institute of Technology, *PhD dissertation*, Cambridge, MA.
56. Kim, J., Varadan, V. V. and Varadan V. K. (1997), "Finite Element Modelling Of Structures Including Piezoelectric Active Devices," *International Journal for Numerical Methods in Engineering*, 40(5), 817–832.
57. Lalande, F., Chaudhry, Z. and Rogers, C. A. (1995), "Impedance-Based Modelling of Actuators and Bonded to Shell Structures," *Journal of Intelligent Material System and Structure*, 6, 765-774.
58. Lammering, R. and Mesecke, R. S. (2003), "Multi-Field Variational Formulations and Related Finite Elements for Piezoelectric Shells," *Smart Materials and Structures*, 12(6), 904–913.
59. Lesietre, G. A. (1998), "Vibration Damping and Control Using Shunted Piezoelectric Materials," *The Shock and Vibration Digest*, 30(3), 187–195.
60. Liang, C., Sun, F. P. and Rogers, C. A. (1994), "Coupled Electro-Mechanical Analysis of Adaptive Material Systems- Determination of the Actuator Power Consumption and System Energy Transfer," *Journal of Intelligent Material Systems and Structures*, 5, 12-20.
61. Liang, C., Sun, F. P. and Rogers, C. A. (1995), "Determination of Design of Optimal Actuator Location and Configuration Based on Actuator Power factor," *Journal of Intelligent Material Systems and Structures*, 6(4), 456-464.
62. Liang, C., Sun, F. P. and Rogers, C. A. (1996), "Electro-Mechanical Impedance Modelling of Active Material System," *Smart Material and Structures*, 5, 171-186.
63. Lim Y. Y., Bhalla, S. and Soh, C. K. (2006), "Structural Identification and Damage Diagnosis Using Self-Sensing Piezo-Impedance Transducers," *Smart Materials and Structures*, 15(4), 987-995.

64. Lim, Y. Y. (2010), Discussion on Coupled Field Analysis, Personal Email Communication.
65. Lin, M.W. and C. A. Rogers. (1993), "Modeling of the Actuation Mechanism in a Beam Structure with Induced Strain Actuators," AIAA-93-1715-CP.
66. Lin, B.; Giurgiutiu, V. (2012) "Power and Energy Transduction Analysis of Piezoelectric Wafer Active Sensors for Structural Health Monitoring", *Structural Health Monitoring – an International Journal*, Vol. 11, No. 1, pp. 109-121, Jan 2012
67. Liu, W. and Giurgiutiu, V. (2006), "Finite Element Modelling And Simulation Of Piezoelectric Wafer Active Sensors Interaction With The Host Structure For Structural Health Monitoring," SPIE's 13th International Symposium on Smart Structures and Materials and 11th International Symposium on NDE for Health Monitoring and Diagnostics, San Diego, CA, 26 February–2 March, 2006, paper #6174-107
68. Liu, W. and Giurgiutiu, V. (2007), "Finite Element Simulation of Piezoelectric Wafer Active Sensors for Structural Health Monitoring with Coupled Field Elements," Proc. of 6th International Workshop on Structural Health Monitoring, 6259, 1-13.
69. Makkonen, T., Holappa, A., Elia, J. and Salomaa, M. M. (2001), "Finite Element Simulation of Thin-Film Composite BAW Resonators," IEEE Transaction on Ultrasonic, Ferroelectrics and Frequency Control, 48(5), 1241-1258.
70. Martin, G. E. (1974), "Dielectric, elastic, and piezoelectric losses in piezoelectric materials," Proc. of Ultrasonics Symp. (Milwaukee, WI, 1974).
71. Mason, W. P. (1966), Crystal Physics of Interaction Process (New York: Academic)
72. Naidu, A. S. K. (2004), "Structural Damage Identification with Admittance Signatures of Smart PZT Transducers" Ph. D Thesis, Nanyang Technological University.
73. Meltz, G., Morey, W. W. and Glenn, W. H. (1989), "Formation of Bragg Grating In Optical Fibers By a Transverse Holographic Method," Optical Letter, 14, 823–825.
74. Nguyen, C. H. and Pietrzko, S. J. (2006), "FE Analysis of A PZT-Actuated Adaptive Beam with Vibration Damping using A Parallel R-L Shunt Circuit," Finite Elements in Analysis and Design, 42(14), 1231–1239.
75. Ong, C. W., Yang, Y., Wong, Y. T., Bhalla, S., Lu, Y., and Soh, C. K. (2002), "The Effects of Adhesive on The Electro-Mechanical Response of A Piezoceramic Transducer

- Coupled Smart System.” SPIE International Conference on Smart Materials, Structures and Systems, ISSS, Bangalore, 191–197.
76. Pandey, A. K. and Biswas, M. (1994), “Damage Detection in Structures Using Changes in Flexibility,” Journal of Sound and Vibration, 169(1), 3-17.
77. Park, G. (2000), “Assessing Structural Integrity Using Mechatronic Impedance Transducers with Applications in Extreme Environments”, Ph.D. Dissertation, Virginia Polytechnic Institute and State University, Blacksburg, VA.
78. Park, G., Cudney, H. H. and Inman, D. J. (2000a), “Impedance Based Health Monitoring of Civil Structural Component,” Journal of Infrastructure System, ASCE, 6(4), 153-160.
79. Park, G., Cudney, H. H. and Inman, D. J. (2000b), “An Integrated Health Monitoring Technique Using Structural Impedance Sensors,” Journal Intelligent Material Systems and Structures, 11, 448-455.
80. Park, G., Inman, D.J. and Farrar, C.R. (2003), “Recent Studies in Piezoelectric Impedance-Based Structural Health Monitoring,” Proceedings of 4th International Workshop on Structural Health Monitoring: from Diagnostics and Prognostics to Structural Health Management, 15-17 September, Stanford University, Palo Alto, CA, DES Tech Publications, Inc., Lancaster, PA, pp. 1423-1430.
81. Park, G., Sohn, H., Farrar, C. R. and Inman, D. J. (2003), “Overview of Piezoelectric Impedance-based Health Monitoring and Path Forward,” The Shock and Vibration Digest, 35, 451-463.
82. Park, S., Lee, J. J. Yun, C. B. and Inman, D.J. (2008), “Electro-Mechanical Impedance-based Wireless Structural Health Monitoring Using PCA-Data Compression and k-means Clustering Algorithms,” Journal Intelligent Material Systems and Structures, 19, 509-520.
83. Pearis, D. M., Grisso, B. L., Margasahayam, R. N., Page, K. R. and Inman, D. J. (2004), “Proof-of Concept Application of Impedance-Based Health Monitoring on Space Shuttle Ground Structures,” Proceedings of SPIE, San Diego, CA, USA, 5394(15), 99-107.
84. PI Ceramic (2003), Product Information Catalogue, Lindenstrabe, Germany,
<http://www.piceramic.de>
85. PI Ceramic (2010), Product Information Catalogue, Lindenstrabe, Germany,
<http://www.piceramic.de>

86. Prabakar, K. and Mallikarjun, R. S. P. (2005), "Acoustic Emission during Phase Transition in Soft PZT Ceramics under an Applied Electric Field," Ferroelectrics Letters Section, 32, 99-110.
87. Qing, X. P., Chan, H. L., Beard, S. J., Ooi, T. K. and Marotta, S. A. (2006), "Effect of Adhesive on Performance of Piezoelectric Elements Used to Monitor Structural Health," International Journal of Adhesion and Adhesives, 26(8), 622-628.
88. Rama Shankar, (2010), "An Integrated Approach for Health Monitoring of Structures" Ph. D Thesis, Indian Institute of Technology, Delhi
89. Robbins, D. H. and Reddy, J. N. (1991), "Finite Element Analysis of Piezoelectrically Actuated Beams," Computers and Structures, 41, 265–279.
90. Rogers, C. A. (1988a), "Workshop Summary", Proceedings of U.S. Army Research Office Workshop on Smart Materials, Structures and Mathematical Issues, edited by C. A. Rogers, September 15-16, Virginia Polytechnic Institute & State University, Technomic Publishing Co., Inc., 1-12.
91. Rogers, C. A., Barker, D. K. and Jaeger, C. A. (1988b), "Introduction to Smart Materials and Structures," Proceedings of U.S. Army Research Office Workshop on Smart Materials, Structures and Mathematical Issues, edited by C.A. Rogers, September 15-16, Virginia Polytechnic Institute & State University, Technomic Publishing Co., Inc., 17-28.
92. Rogers, C. A. (1990), "Intelligent Material Systems and Structures," Proceedings of U.S.-Japan Workshop on Smart/ Intelligent Materials and Systems, edited by I. Ahmad, A. Crowson, C. A. Rogers and M. Aizawa, March 19-23, Honolulu, Hawaii, Technomic Publishing Co., Inc., 11-33.
93. RS Components (2003), Northants, UK, <http://www.rs-components.com>.
94. Ryu, D. H. and Wang, K. H. (2004), "Analysis of interfacial stresses and actuation authorities induced by surface-bonded piezoelectric actuators on curved flexible beams," Smart Materials and Structures, 13(4), 753-761.
95. Saravacos, D. A, Heyliger, P. R. and Hopkins, D. A. (1997), "Layer wise Mechanics and Finite Element for The Dynamic Analysis of Piezoelectric Composite Plates," International Journal of Solids and Structures, 34(3), 359–378.

-
96. Seemann, W., Wolf, K., Straub, A., Hagedorn, P. and Chang, F. (1997), "Bonding Stresses Between Piezoelectric Actuators and Elastic Beams," Proceeding Conference on Smart Structures and Materials, SPIE 3041, 665–675.
97. Seecor piezoceramics. <http://www.seacorpiezo.com/>
98. Shanker, R., Bhalla, S. and Gupta, A. (2011), "Dual Use of PZT Patches as Sensors in Global Dynamic and Local EMI Techniques for Structural Health Monitoring," Journal of Intelligent Material Systems and Structures, 22(16), 1841-1856.
99. Sirohi, J. and Chopra, I. (2000a), "Fundamental Behavior of Piezoceramic Sheet Actuators," Journal of Intelligent Material Systems and Structures, 11(1), 47-61.
100. Sirohi, J. and Chopra, I. (2000a), "Fundamental Behavior of Piezoceramic Sheet Actuators," Journal of Intelligent Material Systems and Structures, 11(1), 47-61.
101. Sirohi, J. and Chopra, I. (2000b), "Fundamental Understanding of Piezoelectric Strain Sensors," Journal of Intelligent Material Systems and Structures, 11(4), 246-257.
102. Soh, C. K., Tseng, K. K. H., Bhalla, S. and Gupta, A. (2000), "Performance of Smart Piezoceramic Patches in Health Monitoring of a RC Bridge." Smart Materials and Structures, 9(4), 533-542.
103. Soh, C. K. and Bhalla, S. (2005), "Calibration of Piezo-Impedance Transducers for Strength Prediction and Damage Assessment of Concrete," Smart Materials and Structures, 14(4), 671-684.
104. Stein, S. C., Liang, C. and Rogers, C. A. (1994), "Power Consumption of Piezoelectric Actuators Driving A Simply Supported Beam Considering Fluid Coupling," Journal of Acoustic Society of America, 96(3), 1598-1604.
105. Sun, F. P., Chaudry, Z., Rogers, C. A., Majmundar, M. and Liang, C. (1995), "Automated Real-time Structure Health Monitoring Via Signature Pattern Recognition," Proceedings of SPIE, February 27 to March 1, San Diego, California, USA, 2443, 236-247.
106. Tinoco, H. A., Serpa, A. L. and Ramos, A. M. (2010), "Numerical Study of The Effects of Bonding Layer Properties on Electrical Signatures of Piezoelectric Sensors," Mecánica Computacional, XXIX, 8391-8409.
107. Tjin, S.; Suresh, R.; Ngo, N. (2004), "Fiber Bragg grating based shear-force sensor: Modeling and testing," Journal of Light wave Technology. 22, 1728–1733.

108. Tjin, S. C., Hao, J., Lam, Y. Z., Ho, Y. C. and Ng, B. K. (2001), "A Pressure Sensor Using Fiber Bragg Grating," *Fiber and Integrated Optics*, 20(1), 59-69.
109. Trindade, M. A., Benjeddou, A. and Ohayon, R. (2001), "Finite Element Modelling of Hybrid Active-Passive Vibration Damping of Multilayer Piezoelectric Sandwich Beams—Part I: Formulation," *International Journal for Numerical Methods in Engineering*, 51(7), 835–854.
110. Tzou, H. S. and Tseng, C. I. (1990), "Distributed Piezoelectric Sensor/Actuator Design for Dynamic Measurement/Control of Distributed Parameter Systems: A Piezoelectric Finite Element Approach," *Journal of Sound and Vibration*, 138(1), 17–34.
111. Vardan, V. K. and Vardan, V. V. (2002), "Micro sensors, Micro electro-mechanical systems (MEMS) and Electronics for Smart Structures and Systems," *Smart Material and Structures*, 9(6), 953-972.
112. Vasques, C. M. A. and Rodrigues, J. D. (2005), "Coupled Three-Layered Analysis of Smart Piezoelectric Beams with Different Electric Boundary Conditions," *International Journal for Numerical Methods in Engineering*, 62(11), 1488–1518.
113. Wan, X. and Taylor, H. F. (2003) " Fiber Bragg Grating Pair Interferometer Sensor With Improved Multiplexing Capacity and High Resolution," *IEEE Photonic Technology Letter*, 15, 742–744
114. Wang, B. T. and Rogers, C. A, (1991), "Laminated Plate Theory for Spatially Distributed Induced Strain Actuators," *Journal of Composite Materials*, 25(4), 433-452.
115. Wang, J. and Zeng, S. (2008), "Enhanced Interface Stress Analysis of Piezoelectric Smart Beams," *Smart Structure and Materials*, 17, 1-12.
116. Watkins, A. J. and Kitcher, C. (2006), "Electrical installation and calculations," Elseviers publication, London, sixth Edition
117. Wu, S. Y., Tran, B. N., Davis, F.Y., Trent, C. L., Edberg, D. L. and Geideman, W. A. (1994), "Active Beam Vibration Control Using PZT Actuators," *Integrated Ferroelectrics: An International Journal*, 4, 281-291.
118. Xu, Y. G. and Liu, G. R. (2002), "A Modified Electro-Mechanical Impedance Model of Piezoelectric Actuator-Sensors for Debonding Detection of Composite Patches," *Journal of Intelligent Material Systems and Structures*, 13(6), 389-396.

-
119. Yamashita, K., Katata, H., Okuyama, M., Miyoshi, H., Kato, G., Aoyagi, S. and Suzuki, Y. (2002), "Arrayed Ultrasonic Micro sensors with High Directivity for In-Air Use Using PZT Thin Film on Silicon Diaphragms," Sensors and Actuators A: Physical, 97(98), 302-307.
120. Yan, W., Lim, C. W., Chen, W. Q., Cai, J. B. (2007), "A Coupled Approach for Damage Delection of Framed Structures Using Piezoelectric Signature," Journal of Sound and Vibration, 307, 802-817.
121. Yang, Y., Lim, Y. Y. and Soh, C. K. (2008), "Practical Issue Related to the Application of the Electro-Mechanical Impedance Technique in Structural Civil Health Monitoring of the Structures: II. Numerical Verification," Smart Material and Structures, 17(3), 1-12.
122. Yang, J., Wang, Y. and Xu, R. G. (2011), "Electro-Mechanical Analysis of Piezoelectric Patch Bonding to Beams," Symposium on Piezoelectricity Acoustic Waves and Device Applications SPAWDA, China, 461-464.
123. Yang, Y., Xu, J. and Soh, C. K. (2005), "Generic Impedance Based Model for Structure- Piezoceramic Interaction System," Journal of Aerospace Engineering, 18(2), 93-101.
124. Yu S, He S and Li W (2010) Theoretical and experimental studies of beam bimorph piezoelectric power harvesters Journal of Mechanics and Materials of Structures 5(3):427–445.
125. Zhang, Y., Xu, F., Chen, J., Wu, C. and Wen, D. (2011), "Electromechanical Impedance Response of a Cracked Timoshenko Beam" Sensors, 11, 7285-7301.
126. Zhou, S. W., Liang, C. and Rogers, C. A. (1993), "Impedance Modelling of Two-Dimensional Piezoelectric Actuators Bonded on A Cylinder", Proceeding of Adaptive Structures and Material Systems, ASME, AD, New Orleans, 35, 245-253.
127. Zhou, S. W., Liang, C. and Rogers, C. A. (1994), "A Dynamic Model of A Piezoelectric Actuator-Driven Thin Plate," Proceeding Of Smart Structures and Materials, SPIE Orlando, FL, 550-562.
128. Zhou, S. W., Liang, C. and Rogers, C. A. (1996), "An Impedance-Based System Modelling Approach For Induced Strain Actuator-Driven Structures," Journal of Vibrations and Acoustics, ASME, 118(3), 323-331.

APPENDIX (A)

MATLAB CODE TO DERIVE ELECTROMECHANICAL ADMITTANCE SIGNATURE FOR REFINED SHEAR LAG MODELED PRESENTED IN EQUATIONS. (4.35) AND (4.36)

```
%refined shear lag for 2D%
LA=.005; %Length of PZT patch
HA=3e-4; %Height of PZT patch
RHO=7800; %Density of PZT patch
D331=-0.00000000021; %Piezoelectric strain co-efficient
mu=0.3; %Poisson ratio
Y11E= 66700000000; %Elastic modulus of PZT Patch
E33T=1.7785e-8; %Electric permittivity of PZT Patch
ETA=0.0325; %Mechanical loss factor
DELTA= 0.0224; %dielectric loss
KK =5.35e-9; %experimentally determined constant
GSA = 1.0e9; %Elastic modulus of bond layer
HE =1.25e-4; %Bond layer Thickness
BETA =0.1; %Damping of Bond layer
V=1.4; %excitation Voltage
cf=0.898; %correction factor
W=.005; %Width of PZT patch
data=dlmread('output.txt','t');
f=data(:,1);
Fr=data(:,2); %real part of structural force
Fi=data(:,3); %imaginary part of structural force
Ur=data(:,4); %real part of structural displacement
Ui=data(:,5); %Imaginary part of structural displacement
F=complex(Fr,Fi);
U=complex(Ur,Ui);
Y=Y11E*(1+ETA*i); %complex young's modulus
FS=D331*(V/HA); %Free piezoelectric strain
GSA1=GSA*(1+BETA*i); %Complex shear modulus
E33T1=E33T*(1-DELTA*i); % complex electrical permittivity
for I=1:250
    omega(I)= 2*pi*f(I);
    U1(I)=omega(I)*U(I)*1i; %effective displacement
    Zs(I)=(2*F(I)/U1(I)); %structural impedance from ansys output
    pe=-(GSA1*2*(1+mu)*LA)/(Zs(I)*HE*i*omega(I));
    qe=(GSA*(1-mu)*mu)/(Y11E*HA*HE);
    alpha=1-(RHO*HA*HE*omega(I)^2)/(GSA1); %shear lag parameter
    p=[1,pe,-1*(alpha*qe),(1-alpha)*pe*qe]; %Shear lag parameter
    r=roots(p); %Inertia parameter
    m1=r(1);
    m2=r(2);
    m3=r(3);
    E1=exp(m1*LA);
    E2=exp(m2*LA);
    E3=exp(m3*LA);
    Mat=[1,1,1;(1+m1/pe),(1+m2/pe),(1+m3/pe);(1+m1/pe)*m1*E1,(1+m2/pe)*m2*E2,(1+m3/pe)*m3*E3];
```

```

Constants=inv(Mat)*[0,0,FS]';
A1=Constants(1);
A2=Constants(2);
A3=Constants(3);
u=A1*E1+A2*E2+A3*E3;
up=A1*(1+m1/pe)*E1+A2*(1+m2/pe)*E2+A3*(1+m3/pe)*E3;
Zeq(I)=Zs(I)*(u/up);
% 2D admittance signature%
k(I)=omega(I)*sqrt(RHO*(1-mu*mu)/Y);
K(I)=k(I)*LA;
C(I)=tan(cf*K(I))/(cf*K(I));
Za(I)=((2*HA*Y)/(1i*omega(I)*C(I)*(1-mu)));
M(I)=4*omega(I)*1i*((LA*LA)/HA);
Z11(I)=Za(I)/(Zeq(I)+Za(I));
y1(I)= M(I)*(E33T1-KK+KK*Z11(I)*C(I));
end
data(:,1)=f;
G1=real(y1);
figure
plot(f,G1)
B1=imag(y1);
figure
plot(f,B1)

```

APPENDIX (B)

MATLAB CODER TO DERIVE ELECTROMECHANICAL ADMITTANCE SIGNATURE FOR REFINED SHEAR LAG MODELED INCLUDING COMBINED INERTIA EFFECT PRESENTED IN EQUATION (4.47)

```

LA=.005; %Length of PZT patch
HA=3e-4; %Height of PZT patch
RHO=7800; %Density of PZT patch
RHO1=1000; % Density of Adhesive
D331=-0.00000000021; %Piezoelectric strain co-efficient
mu=0.3; %Poisson ratio
Y11E= 66700000000; %Elastic modulus of PZT Patch
E33T=1.7785e-8; %Electric permittivity of PZT Patch
ETA=0.0325; %Mechanical loss factor
DELTA= 0.0224; %dielectric loss
KK =5.35e-9; %experimentally determined constant
GSA = 1.0e9; %Elastic modulus of bond layer
HE =1.25e-4; %Bond layer Thickness
BETA =0.1; %Damping of Bond layer
V=1.4; %excitation Voltage
cf=0.898; %correction factor
W=.005; %Width of PZT patch

data=dlmread('output.txt','\t');
f=data(:,1);
Fr=data(:,2); %real part of structural force
Fi=data(:,3); %imaginary part of structural force
Ur=data(:,4); %real part of structural displacement
Ui=data(:,5); %Imaginary part of structural displacement

F=complex(Fr,Fi);
U=complex(Ur,Ui);
Y=Y11E*(1+ETA*1i); %complex young's modulus
FS=D331*(V/HA); %Free piezoelectric strain
GSA1=GSA*(1+BETA*1i); %Complex shear modulus
E33T1=E33T*(1-DELTA*1i); % complex electrical permittivity

for I=1:250
    omega(I)= 2*pi*f(I);
    U1(I)=omega(I)*U(I)*1i; %effective displacement
    Zs(I)=(2*F(I)/U1(I)); %structural impedance from ansys output
    pe=-(GSA1*2*(1+mu)*LA)/(Zs(I)*HE*1i*omega(I)); %shear lag parameter
    qe=(GSA*(1-mu*mu))/(Y11E*HA*HE); %Shear lag parameter
    alpha=1-((RHO+0.5*RHO1)*HA*HE*omega(I)^2)/(GSA1)); %Inertia parameter
    beta1=1+ ((HE*HA*RHO1*omega(I)^2)/(2*GSA1)); %Inertia parameter
    p=[1,pe,-1*(alpha*qe),(alpha-beta1)*pe*qe];
    r=roots(p);
    m1=r(1);
    m2=r(2);
    m3=r(3);
    E1=exp(m1*LA);
    E2=exp(m2*LA);
    E3=exp(m3*LA);
    Mat=[1,1,1;(1+m1/pe),(1+m2/pe),(1+m3/pe);(1+m1/pe)*m1*E1,(1+m2/pe)*m2*E2,(1+m3/pe)*m3*E3];
    Constants=inv(Mat)*[0,0,FS]';

```

```

A1=Constants(1);
A2=Constants(2);
A3=Constants(3);
u=A1*E1+A2*E2+A3*E3;
up=A1*(1+m1/pe)*E1+A2*(1+m2/pe)*E2+A3*(1+m3/pe)*E3;
Zeq(I)=Zs(I)*(u/up);
% 2D admittance signature%
k(I)=omega(I)*sqrt(RHO*(1-mu*mu)/Y);
K(I)=k(I)*LA;
C(I)=tan(cf*K(I))/(cf*K(I));
Za(I)=((2*HA*Y)/(1i*omega(I)*C(I)*(1-mu)));
M(I)=4*omega(I)*1i*((LA*LA)/HA);
Z1(I)=Za(I)/(Zs(I)+Za(I));
Z11(I)=Za(I)/(Zeq(I)+Za(I));
y(I)= M(I)*(E33T1-KK+KK*Z1(I)*C(I));
y1(I)= M(I)*(E33T1-KK+KK*Z11(I)*C(I));
end
data(:,1)=f;
G1=real(y1);
figure
plot(f,G1)
B1=imag(y1);
figure
plot(f,B1)

```

APPENDIX (C)**MATLAB CODER TO DERIVE CONTINUUM ELECTROMECHANICAL ADMITTANCE SIGNATURE PRESENTED IN CHAPTER-5 IN EQUATION (5.15)**

```

LA=0.005; %Length of PZT patch
HA=3e-4; %Height of PZT patch
RHO=7800; %Density of PZT patch
RHO1=1000; % Density of Adhesive
D331=-0.00000000021; %Piezoelectric strain co-efficient
mu=0.3; %Poisson ratio
Y11E= 66700000000; %Elastic modulus of PZT Patch
E33T=1.7785e-8; %Electric permittivity of PZT Patch
ETA=0.0325; %Mechanical loss factor
DELTA= 0.0224; %dielectric loss
KK =5.35e-9; %experimentally determined constant
GSA = 1.0e9; %Elastic modulus of bond layer
HE =1.25e-4; %Bond layer Thickness
BETA =0.1; %Damping of Bond layer
V=1.4; %excitation Voltage
cf=0.898; %correction factor
W=.005; %Width of PZT patch
data=dlmread('output.txt','t');
f=data(:,1);
Fr=data(:,2); %real part of structural force
Fi=data(:,3); %imaginary part of structural force
Ur=data(:,4); %real part of structural displacement
Ui=data(:,5); %Imaginary part of structural displacement
F=complex(Fr,Fi);
U=complex(Ur,Ui);
Y=Y11E*(1+ETA*1i); %complex young's modulus
FS=D331*(V/HA); %Free piezoelectric strain
GSA1=GSA*(1+BETA*1i); %Complex shear modulus
E33T1=E33T*(1-DELTA*1i); % complex electrical permittivity
for I=1:250
    omega(I)= 2*pi*f(I);
    U1(I)=omega(I)*U(I)*1i; %effective displacement
    Zs(I)=(2*F(I)/U1(I)); %structural impedance from ansys output
    pe=-(GSA1*2*(1+mu)*LA)/(Zs(I)*HE*1i*omega(I)); %shear lag parameter
    qe=(GSA*(1-mu*mu))/(Y11E*HA*HE); %Shear lag parameter
    alpha=1-((RHO+0.5*RHO1)*HA*HE*omega(I)^2)/(GSA1)); %Inertia parameter
    beta1=1+ ((HE*HA*RHO1*omega(I)^2)/(2*GSA1)); %Inertia parameter
    p=[1,pe,-1*(alpha*qe),(alpha-beta1)*pe*qe];
    r=roots(p);
    m1=r(1);
    m2=r(2);
    m3=r(3);
    E1=exp(m1*LA);
    E2=exp(m2*LA);
    E3=exp(m3*LA);
    Mat=[1,1,1;(1+m1/pe),(1+m2/pe),(1+m3/pe);(1+m1/pe)*m1*E1,(1+m2/pe)*m2*E2,(1+m3/pe)*m3*E3];
    Constants=inv(Mat)*[0,0,FS]';
    A1=Constants(1);
    A2=Constants(2);
    A3=Constants(3);

```

```
ucon(I)=A1*(1+m1/pe)*(E1-1)+A2*(1+m2/pe)*(E2-1)+A3*(1+m3/pe)*(E3-1); %Continuum Displacement
M(I)=4*omega(I)*1i*((LA*LA)/HA);
y1(I)= M(I)*(E33T1-KK)-4*KK*LA*1i*omega(I)*ucon(I)/(D331*V);
end
data(:,1)=f;
G1=real(y1);
figure
plot(f,G1)
B1=imag(y1);
figure
plot(f,B1)
```

APPENDIX (D)**MATLAB CODER TO DERIVE SHEAR STRESS, EFFECTIVE STRAIN AND AXIAL STRESS FOR REFINED SHEAR LAG MODEL FOR EQUATIONS (4.48), (4.49) AND (4.52)**

```

LA=.005; %Length of PZT patch
HA=3e-4; %Height of PZT patch
RHO=7800; %Density of PZT patch
RHO1=1000; % Density of Adhesive
D331=-0.00000000021; %Piezoelectric strain co-efficient
mu=0.3; %Poisson ratio
Y11E= 66700000000; %Elastic modulus of PZT Patch
E33T=1.7785e-8; %Electric permittivity of PZT Patch
ETA=0.0325; %Mechanical loss factor
DELTA= 0.0224; %dielectric loss
KK =5.35e-9; %experimentally determined constant
GSA = 1.0e9; %Elastic modulus of bond layer
HE =1.25e-4; %Bond layer Thickness
BETA =0.1; %Damping of Bond layer
V=1.4; %excitation Voltage
cf=0.898; %correction factor
W=.005; %Width of PZT patch

data=dlmread('output.txt','t');
f=data(:,1);
Fr=data(:,2); %real part of structural force
Fi=data(:,3); %imaginary part of structural force
Ur=data(:,4); %real part of structural displacement
Ui=data(:,5); %Imaginary part of structural displacement

F=complex(Fr,Fi);
U=complex(Ur,Ui);
Y=Y11E*(1+ETA*1i); %complex young's modulus
FS=D331*(V/HA); %Free piezoelectric strain
GSA1=GSA*(1+BETA*1i); %Complex shear modulus
E33T1=E33T*(1-DELTA*1i); % complex electrical permittivity
for I=1:250
    omega(I)= 2*pi*f(I);
    U1(I)=omega(I)*U(I)*1i;
    Zs(I)= (2*F(I)/U1(I));
    pe(I)=-(GSA1*2*(1+mu)*LA)/(Zs(I)*HE*1i*omega(I));
    qe(I)=(GSA*(1-mu*mu))/(Y11E*HA*HE);
    alpha(I)=((RHO*HA*HE*omega(I)^2)/GSA1-1);
    p=[1,pe(I),1*(alpha(I)*qe(I)),(alpha(I)+1)*pe(I)*qe(I)];
    r=roots(p);
    m1(I)=r(1);
    m2(I)=r(2);
    m3(I)=r(3);
    i=1;
    for x=0:5.0000e-004:(.005)
        E1(i,I)=exp(m1(I)*x);
        E2(i,I)=exp(m2(I)*x);
        E3(i,I)=exp(m3(I)*x);
        E11(i,I)=exp(2*m1(I)*LA);
    end
end

```

```

E22(i,I)=exp(2*m2(I)*LA);
E33(i,I)=exp(2*m3(I)*LA);
Mat=[1,1,1;(1+m1(I)/pe(I)),(1+m2(I)/pe(I)),(1+m3(I)/pe(I));(1+m1(I)/pe(I))*m1(I)*E1(i,I),(1+m2(I)/pe(I))*m2(I)*E
2(i,I),(1+m3(I)/pe(I))*m3(I)*E3(i,I)];
Constants=inv(Mat)*[0,0,FS]';
A1(I)=Constants(1);
A2(I)=Constants(2);
A3(I)=Constants(3);
u(i,I)=A1(I)*E1(i,I)+A2(I)*E2(i,I)+A3(I)*E3(i,I);
up(i,I)=A1(I)*(1+m1(I)/pe(I))*E1(i,I)+A2(I)*(1+m2(I)/pe(I))*E2(i,I)+A3(I)*(1+m3(I)/pe(I))*E3(i,I);
Ucon(i,I)=(A1(I)*(1+m1/pe)*(E1(i,I)-1)+A2(I)*(1+m2/pe)*(E2(i,I)-1)+A3(I)*(1+m3/pe)*(E3(i,I)-1));
tou(i,I)= GSA1*(up(i,I)-u(i,I))/HE;                                     %Shear stress
sp(i,I)=A1(I)*E1(i,I)*(m1(I))+A2(I)*E2(i,I)*(m2(I))+A3(I)*E3(i,I)*(m3(I))+(A1(I)*E1(i,I)*(m1(I)^2)+A2(I)*E2(i,I)
)*(m2(I)^2)+A3(I)*E3(i,I)*(m3(I)^2))/pe(I);                           %Effective Strain
Teff(i,I)=(Y/(1-mu))*(sp(i,I)-FS);                                         %Shear stress
    end
end
up=abs(up);
u=abs(u);
tou=abs(tou);
Ucon1=abs(Ucon);
Den1=abs(Den);
Teff=abs(Teff);

```

APPENDIX (E)

**MATLAB CODER TO DERIVE ELECTRICAL TRIANGULAR POWER COMPONENT
FOR CONTINUUM MODEL DERIVED IN EQS. (6.7), (6.8), (6.9) AND (6.10) AND FOR
MODIFIED ELECTRO-MECHANICAL COEFFICIENT EXPRESSED IN EQ. (6.27)**

```

LA=.005; %Length of PZT patch
HA=3e-4; %Height of PZT patch
RHO=7800; %Density of PZT patch
RHO1=1000; % Density of Adhesive
D331=-0.00000000021; %Piezoelectric strain co-efficient
mu=0.3; %Poisson ratio
Y11E= 66700000000; %Elastic modulus of PZT Patch
E33T=1.7785e-8; %Electric permittivity of PZT Patch
ETA=0.0325; %Mechanical loss factor
DELTA= 0.0224; %dielectric loss
KK =5.35e-9; %experimentally determined constant
GSA = 1.0e9; %Elastic modulus of bond layer
HE =1.25e-4; %Bond layer Thickness
BETA =0.1; %Damping of Bond layer
V=1.4; %Excitation Voltage
cf=0.898; %correction factor
W=.005; %Width of PZT patch
EE=8.85*10e-12; % Electrical permittivity of PZT patch at vacuum
ER=2400; %Relative dielectric permittivity for PZT patch

data=dlmread('output.txt','t');
f=data(:,1);
Fr=data(:,2); %real part of structural force
Fi=data(:,3); %imaginary part of structural force
Ur=data(:,4); %real part of structural displacement
Ui=data(:,5); %Imaginary part of structural displacement

F=complex(Fr,Fi);
U=complex(Ur,Ui);
Y=Y11E*(1+ETA*1i); %complex young's modulus
FS=D331*(V/HA); %Free piezoelectric strain
GSA1=GSA*(1+BETA*1i); %Complex shear modulus
E33T1=E33T*(1-DELTA*1i); % complex electrical permittivity

for I=1:250
    omega(I)= 2*pi*f(I);
    U1(I)=omega(I)*U(I)*1i; %effective displacement
    Zs(I)=(2*F(I)/U1(I)); %structural impedance from ansys output
    pe=-(GSA1*2*(1+mu)*LA)/(Zs(I)*HE*1i*omega(I)); %shear lag parameter
    qe=(GSA*(1-mu*mu))/(Y11E*HA*HE); %Shear lag parameter
    alpha=1-(((RHO+0.5*RHO1)*HA*HE*omega(I)^2)/(GSA1)); %Inertia parameter
    beta1=1+ ((HE*HA*RHO1*omega(I)^2)/(2*GSA1)); %Inertia parameter
    p=[1,pe,-1*(alpha*qe),(alpha-beta1)*pe*qe];
    r=roots(p);
    m1=r(1);
    m2=r(2);
    m3=r(3);
    E1=exp(m1*LA);
    E2=exp(m2*LA);

```

```

E3=exp(m3*LA);
Mat=[1,1,1;(1+m1/pe),(1+m2/pe),(1+m3/pe);(1+m1/pe)*m1*E1,(1+m2/pe)*m2*E2,(1+m3/pe)*m3*E3];
Constants=inv(Mat)*[0,0,FS]';
A1=Constants(1);
A2=Constants(2);
A3=Constants(3);
ucon(I)=A1*(1+m1/pe)*(E1-1)+A2*(1+m2/pe)*(E2-1)+A3*(1+m3/pe)*(E3-1); %Continuum Displacement
M(I)=4*omega(I)*1i*((LA*LA)/HA);
y1(I)= M(I)*(E33T1-KK)-4*KK*LA*1i*omega(I)*ucon(I)/(D331*V);
Emech(I)=LA*W*Y*((A1*(1+m1/pe)*(E1-1)+A2*(1+m2/pe)*(E2-1)+A3*(1+m3/pe)*(E3-1))^2-
(FS*(A1*(1+m1/pe)*(E1-1)+A2*(1+m2/pe)*(E2-1)+A3*(1+m3/pe)*(E3-1)))); %Mechanical energy
end
data(:,1)=f;
G1=real(y1);
B1=imag(y1);
kk=(G.*G+B.*B);
kk1=sqrt(kk);
kk2=max(kk1,[],1);
Papp= 0.5*V^2*kk1;
Pactive=0.5*V^2*G;
Preactive=0.5*V^2*B;
Ppeak=0.5*V^2*kk2;
FEmech=abs(Emech);
Elec=0.5*ER*EE*((LA*W)/HA)*V^2;
keff=FEmech/Elec;

```

AUTHOR'S PUBLICATIONS

JOURNALS

1. Moharana, S. and Bhalla, S. (2012), “**Numerical Investigation of Shear Lag Effect on PZT-Structure Interaction: Review and Application,**” *Current Science*, Vol. 103, No. 25, pp. 685-696.
2. Bhalla, S. and Moharana, S. (2012), “**A Refined Shear Lag Model for Adhesively Bonded Piezo Transducer,**” *Journal of Intelligent Material Systems and Structures*, (Published online on 5th September, 2012, DOI: 10.1177/1045389X12457837) Printing version in Press.
3. Moharana, S. and Bhalla, S. (2012), “**A Continuum Based Shear Lag Model for Electro- Mechanical Impedance (EMI) Technique,**” *International Journal of Solids and Structures*, (communicated).
4. Moharana, S. and Bhalla, S. (2012), “**Review of Power Consumption and Energy Efficiency for Piezo- Impedance Model using Electro-Mechanical Impedance (EMI) Technique,**” *Electroceramics*, (under preparation).

CONFERENCE/SYMPORIUM

1. Moharana, S. and Bhalla, S. (2009), “**Finite Element Modelling of PZT-Structure Interaction for Electro-mechanical Impedance technique**” (Extended Abstract), *Proceedings of 3rd International Congress on Computational Mechanics and Simulation*, 1-3 December, Indian Institute of Technology, Bombay, pp. 127-128.
2. Moharana, S. and Bhalla, S. (2010), “**Numerical Study of PZT-Structure Interaction For Electro Mechanical Impedance (EMI) Technique,**” Presented on *VETOMAC-VI*, 13th - 15th DEC, 2010, IIT Delhi, pp 571-578.

-
3. Moharana, S. and Bhalla, S. (2012), “**New Refined 1D Analytical and Numerical Shear Lag Model Using Electro-Mechanical Impedance (EMI) Technique**,” *Proceedings of International Conference on Smart Materials Structures and Systems*, January 04-07, 2012, Indian Institute of Science, Bangalore, India.
4. Moharana, S. and Bhalla, S. (2012), “**Review of Power Consumption and Energy Efficiency for Piezo- Impedance Model using Electro-Mechanical Impedance (EMI) Technique**,” *Indo-French symposium on Sensors Technologies and Systems*, 1-4 March, IIT, Delhi.
5. Poster presentation for the topic “**Investigation of Shear Force Mechanism for Coupled Piezo-Elastodynamic Model Using Electro-Mechanical Impedance (EMI) Technique**” on *National Science Day* at IIT, Delhi on 28/02/2012.
6. Maharan, S. and Bhalla, S. (2013), “**Non-Destructive Evaluation of Concrete Structures using Piezo-Impedance Transducer**,” UKIERI Congress, 5th -8th March, 2013, National Institute of Technology, Jalandhar, Punjab. (Final paper accepted)

BIO DATA

Sumedha Moharana was born on 25th April 1985 in Ganjam district in Odisha, India. She received her Bachelor of Engineering with Honors in May, 2006 from College of Engineering and Technology, Jeypore under Berhampur University. She did her Master of Technology from College of Engineering and Technology, Bhubaneswar under Biju Pattanaik University of Technology in 2008. In 2009, she joined as a research scholar in the Department of Civil Engineering IIT Delhi. Her research interests are the bonding effect on piezo sensor based structural health monitoring, analytical formulation of integrated sensor-structure system and smart material and structures